Pontifícia Universidade Católica
do Rio de Janeiro

Johnes Ricardo Gonçalves

Semi-Analytical Methods for the Electromagnetic Propagation Analysis of Inhomogeneous Anisotropic Waveguides of Arbitrary Cross-Section by Using Cylindrical Harmonics

Tese de Doutorado

Thesis presented to the Programa de Pós–graduação em Engenharia Elétrica, do Departamento de Engenharia Elétrica da PUC-Rio in partial fulfillment of the requirements for the degree of Doutor em Engenharia Elétrica.

Advisor : Prof. Guilherme Simon da Rosa
Co-advisor: Prof. Fernando Lisboa Teixeira

Rio de Janeiro
September 2022

Pontifícia Universidade Católica
do Rio de Janeiro

Johnes Ricardo Gonçalves

Semi-Analytical Methods for the Electromagnetic Propagation Analysis of Inhomogeneous Anisotropic Waveguides of Arbitrary Cross-Section by Using Cylindrical Harmonics

Thesis presented to the Programa de Pós–graduação em Engenharia Elétrica da PUC-Rio in partial fulfillment of the requirements for the degree of Doutor em Engenharia Elétrica. Approved by the Examination Committee:

Prof. Guilherme Simon da Rosa
Advisor
Departamento de Engenharia Elétrica – PUC-Rio

Prof. Fernando Lisboa Teixeira
ElectroScience Laboratory – Ohio State University

Prof. Rafael Ferreira da Silva Caldeirinha
Instituto Politécnico de Leiria – IPL

Prof. Rafael Abrantes Penchel
Departamento de Engenharia Elétrica – Unesp

Prof. Fernando Jose da Silva Moreira
Departamento de Engenharia Elétrica – UFMG

Prof. José Ricardo Bergmann
Centro de Estudos em Telecomunicações – PUC-Rio

Rio de Janeiro, September the 30th, 2022

Johnes Ricardo Gonçalves

Received the B.S. degree in telecommunications engineering from the Federal University of São João Del-Rei, Minas Gerais, Brazil, in 2015, and the M.S. degree in electrical engineering from the Pontifical Catholic University of Rio de Janeiro, Rio de Janeiro, Brazil, in 2018. His research interests include semi-analytical methods for complex waveguides and wave propagation in tunnels.

Bibliographic data

Johnes Ricardo Gonçalves

Semi-Analytical Methods for the Electromagnetic Propagation Analysis of Inhomogeneous Anisotropic Waveguides of Arbitrary Cross-Section by Using Cylindrical Harmonics / Johnes Ricardo Gonçalves; advisor: Guilherme Simon da Rosa; co-advisor: Fernando Lisboa Teixeira. – 2022.

116 f: il. color. ; 30 cm

Tese (doutorado) - Pontifícia Universidade Católica do Rio de Janeiro, Departamento de Engenharia Elétrica, 2022.

Inclui bibliografia

1. Engenharia Elétrica – Teses. 2. Engenharia Elétrica – Teses. 3. Meios anisotrópicos. 4. Mapeamento conformal. 5. Harmônicos cilíndricos. 6. Técnicas de perturbação. 7. Método de casamento pontual. I. Simon da Rosa, Guilherme. II. Teixeira, Fernando Lisboa. III. Pontifícia Universidade Católica do Rio de Janeiro. Departamento de Engenharia Elétrica. IV. Título.

CDD: 621.3

To my parents, for their support
and encouragement.

Acknowledgments

First, I would like to thank my advisor, Professor Guilherme Simon da Rosa for all the support and guidance during this research. Without your assistance and readiness with meticulously accurate ideas and hints, this work would not have been possible and successful. I would also like to thank my co-advisor, Professor Fernando Lisboa Teixeira for his support throughout the research.

I would like to acknowledge and thank my family, my parents Maria Aparecida Ladeira and Geraldo Fonseca Gonçalves, my brothers Lidiane, Emanuel, Ana Luiza and Francisco, and my grandmother Vicentina. They always encouraged and believed in me.

I would like to thank my colleagues at PUC-Rio and CETUC, Teddy, Yoiz, Lisseth, Leonardo, Edson and also the staff at SBMETA, especially Professor Glaucio Lima Siqueira and Professor Marbey Manhães Mosso.

And last but not least, to God, the primordial source of everything.

This work was supported in part by the Brazilian Agency CNPq under Grant 141617/2019-5 and in part by the Brazilian Agency FAPERJ under Grant E-26/201.166/2020.

This study was financed in part by the Coordenação de Aperfeiçoamento de Pessoal de Nível Superior – Brasil (CAPES) – Finance Code 001.

Abstract

Johnes Ricardo Gonçalves; Simon da Rosa, Guilherme (Advisor); Teixeira, Fernando Lisboa (Co-Advisor). **Semi-Analytical Methods for the Electromagnetic Propagation Analysis of Inhomogeneous Anisotropic Waveguides of Arbitrary Cross-Section by Using Cylindrical Harmonics**. Rio de Janeiro, 2022. 116p. Tese de Doutorado – Departamento de Engenharia Elétrica, Pontifícia Universidade Católica do Rio de Janeiro.

This thesis presents a study on semi-analytic methods for modeling waveguides with complex-shaped boundaries. The electromagnetic fields inside inhomogeneous and anisotropic media are solved via cylindrical harmonics as a basis for other numerical approaches, including the regular perturbation method (RPM), the cavity-material perturbation method (CMPM), and the point-matching method (PMM). The novel semi-analytic solutions we have explored here can be employed for the analysis of wireless communication along tunnels and boreholes as well as for the modeling of realistic logging-while-drilling (LWD) sensors and their environments at low-frequency geophysical problems. We studied the potential of the RPM when combining it with the transformation optics (TO) principles to analyze an eccentric coaxial waveguide filled with anisotropic materials. Furthermore, we have extended the classical CMPM proposed by Harrington to handling anisotropic media for solving the cutoff wavenumbers of the modal fields in the same eccentric coaxial waveguide in an approximated but numerically efficient manner. Another perturbation solution is proposed here and combines the low-order corrections from RPM into the CMPM for providing high-order corrections to the cutoff wavenumbers of the modes supported in this guide. A mathematical formulation of a semi-analytic point-matching method for solving more complex anisotropic-filled waveguides with an arbitrary number of layers is also presented. An improved version of this method is introduced for modeling non-circular multi-layered cylindrical guided structures. Such point-matching-based solutions represent good alternatives to brute-force approaches such as finite-element and finite-difference methods and motivate further investigations. We present a series of validation results showing the accuracy, efficiency, and potential limitations of the explored methods.

Keywords

Anisotropic media; Conformal mapping; Cylindrical harmonics; Perturbation techniques; Point-matching method.

Resumo

Johnes Ricardo Gonçalves; Simon da Rosa, Guilherme; Teixeira, Fernando Lisboa. **Métodos Semianalíticos para a Análise da Propagação Eletromagnética em Guias de Onda Anisotrópicos e não homogêneos com Seção Transversal Arbitrária Usando Harmônicos Cilíndricos**. Rio de Janeiro, 2022. 116p. Tese de Doutorado – Departamento de Engenharia Elétrica, Pontifícia Universidade Católica do Rio de Janeiro.

Esta tese apresenta um estudo sobre métodos semianalíticos para modelagem de guias de ondas com contornos complexos. Os campos eletromagnéticos dentro de meios não homogêneos e anisotrópicos são resolvidos por meio de harmônicos cilíndricos como base para outras abordagens numéricas, como o método de perturbação regular (RPM), o método de perturbação de material em cavidade (CMPM) e o método de casamento de pontos (PMM). As novas soluções semianalíticas que exploramos aqui podem ser empregadas para a análise de comunicação sem fio ao longo de túneis, bem como para a modelagem de sensores realistas de perfilagem durante a perfuração em problemas geofísicos de baixa frequência. Estudamos o potencial do RPM ao combiná-lo com os princípios da transformação óptica (TO) para analisar um guia de onda coaxial excêntrico preenchido com materiais anisotrópicos. Além disso, estendemos o CMPM clássico proposto por Harrington para lidar com meios anisotrópicos para resolver os números de onda de corte dos campos modais no mesmo guia de onda de maneira aproximada, mas numericamente eficiente. Outra solução de perturbação é proposta combinando as correções de baixa ordem do RPM no CMPM para fornecer correções de alta ordem para os números de onda de corte dos modos suportados pelo guia. Uma formulação matemática de um método semianalítico baseado em PMM para resolver guias de onda preenchidos com meios anisotrópicos e com camadas arbitrárias também é apresentada. Uma versão melhorada deste método é introduzida para modelar estruturas guiadas cilíndricas de múltiplas camadas não circulares. Essas soluções baseadas em casamento de pontos representam boas alternativas para abordagens de força bruta, como métodos de elementos finitos e de diferenças finitas.

Palavras-chave

Meios anisotrópicos; Mapeamento conformal; Harmônicos cilíndricos; Técnicas de perturbação; Método de casamento pontual.

Table of contents

List of figures

List of tables

List of Abbreviations

CEM – Computational electromagnetics
FDTD – Finite-difference time-domain method
FEM – Finite-element method
FIT – Finite-element method
MMT – Mode-matching technique
NMM – Numerical mode-matching
MoM – Method of Moments
PEC – Perfect electric conductor
PML – Perfectly matched layer
TO – Transformation optics
RPM – Regular perturbation method
CMPM – Cavity-material perturbation method
ICMPM – Improved cavity-material perturbation method
PMM – Point-matching method
SPMM – Straightforward point-matching method
IPMM – Improved point-matching method

1
Introduction

1.1
General Introduction

Numerical and analytical models for electromagnetic analysis of inhomogeneous and anisotropic cylindrical guided structures have important applications for several real-life scenarios such as the syntheses of waveguides, filters, sensing probes, among other equipment in microwave and millimeter-wave systems. Also, these structures can be employed for the analysis of wireless communication along tunnels and boreholes as well as for the modeling of realistic logging-while-drilling (LWD) sensors and their environments at low-frequency geophysical problems.

Several computational electromagnetics (CEM) methods can be employed for solving the boundary-value problems associated with inhomogeneous and anisotropic waveguides. Today, the finite difference, finite element, and integral equation [1] based methods are prevalent techniques because their numerical implementations are relatively simple and they have become quite popular as most commercial CEM software include such solvers in their simulation engines [2–4]. Such *brute-force methods*, however, require a lot of computational resources, and even with the constant evolution of hardware and computational power, the accurate modeling of inhomogeneous and anisotropic media remains a challenging task.

Fig. 1.1 shows a typical waveguide cross-section filled with anisotropic materials this work desires to explore. Notice the cross-section is inhomogeneous, and can be seen as a non-circular multilayer waveguide. We will investigate some analytical and semi-analytical methods for solving Maxwell's equations, in an approximated manner, on the grounds of the cylindrical harmonics that solve the vector Helmholtz equation in uniaxally anisotropic media. The methods we have studied do not need the discretization of the computational domain as in the brute-force alternatives, and were carefully tailored for structures such as that shown in Fig. 1.1. In what follows, we describe our basic methodology for modeling more simple-shaped problems, as eccentric circular layers, and then, our introductory reasoning on the model for

more complex-shaped problems. Several analytic and semi-analytic techniques have been developed to determine the cutoff wavenumbers of the propagating modes in eccentric waveguides. Among them, we can mention the work in [5], where cylindrical harmonic functions were combined with the Graf's addition theorem for describing the effect of small eccentricities. In [6], specialized formulas to small eccentricities were also obtained from an eigenfunction expansion of cylindrical harmonics, but using a series of approximations to satisfy boundary conditions of the problem based on trigonometric formulae rather than the translational addition theorem. Very recently, the cutoff wavenumbers of eccentric coaxial waveguides were analyzed using a bipolar coordinate system and the corresponding Helmholtz equation solved via the method of separation of variables with proper approximations made for small eccentricities in [7, 8].

In addition to the low-order approximated analytic solutions reported above, several numerical techniques can be employed to solve the problem at hand. In the pioneer work in [9], the point-matching method was used. In [10], the finite difference method was applied to obtain the cutoff wavenumbers of the high-order transverse magnetic (TM) and transverse electric (TE) modes in an eccentric coaxial waveguide.

A more complex-shape guided structure has multiple layers, but in general, no known analytical solutions are available. In some scattering problems, where plane waves incident over cylindrical geometries with simple cross-sections, such as circles and ellipses, closed-form are available [11] and [12] in terms of special Bessel and Mathieu functions. The scattering of other complex geometries, however, requires the employment of brute-force methods, such as method of moments (MoM) [13], finite difference time domain (FDTD) [14,15] or finite element method (FEM) [16]. In addition, some methods are in a middle ground between analytical and brute-force approaches, where a series expansion in terms of special functions are employed to match the boundary conditions in cylinders with cross-sections that does not deviate a lot from circles or ellipsis. These semi-analytical methods will be denote herein was point-matching methods (PMMs)[1], and have been used with success of the years for the analysis of non-circular hollow waveguides [9, 17, 18], scattering by dielectric cylinders [19–21], and others wave-guided-devices [22, 23].

[1]These methods are also known as *field matching techniques* or *discrete mode-matching methods*.

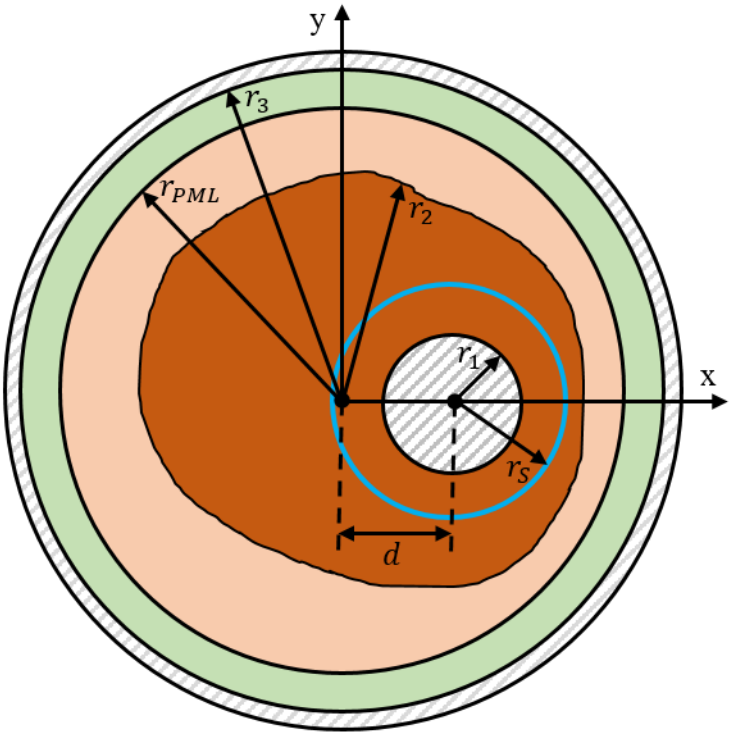

Figure 1.1: Geometry of a cylindrical waveguide with non-circular layers.

1.2 Major Research Contributions

In this Thesis we explore semi-analytical methods for modeling electromagnetic wave propagation in complex waveguided structures. The importance of the present research is due its value both in technological as well as in academic aspects for facilitating parametric studies for device and tool design with techniques far more economical than brute-force numerical approaches. Accordingly, the following topics of study correspond to our original scientific contributions:

- The formulation of the regular perturbational method (RPM) for modeling anisotropic coaxial waveguides with small eccentricities.
- A generalization version of the RPM is implemented to analyze cylindrical waveguide filled with eccentric anisotropic rod.
- An extended and more general version of Harrington's cavity-material perturbation method (CMPM) for modeling anisotropic coaxial waveguides with small eccentricities is implemented.
- The combination of two different perburbational approaches (RPM and CMPM formulations) is applied for the analysis of eccentric coaxial waveguides filled with anisotropic medium.

– The formulation of point-matching-based methods for solving complex anisotropic-filled non-circular multi-layered cylindrical guided structures.

– The formulation of a semi-analytical source expansion in terms of the cylindrical harmonics is developed in complement of the PMM formulation.

– An improved version of the PMM implementation, denoted IPMM, is developed to analyze the electromagnetic propagation tunnels.

1.3 Thesis Organization

The rest of this Thesis is organized as follows. In Chapter 2, we present a mathematical formalism for the calculation of electromagnetic fields in cylindrical and anisotropic medium using Maxwell's equations as a starting point. Also, a method based on transformation optics principles is introduced to map an eccentric coaxial waveguide into a concentric coaxial waveguide. In Chapter 3, we present the RPM to solve the wave equations resulting from the conformal mapping presented in Chapter 2. The methodology is expanded to the analysis of anisotropic waveguides filled with anisotropic rods. In Chapter 4, the effects of the eccentricity on the cutoff wavenumbers are accounted for and investigated via the anisotropic-extended CMPM. We also explore a high-order perturbation solution on combining the TO, RPM, and the CMPM approaches. In Chapter 5, two formulations of the PMM are presented for investigating waveguides filled with anisotropic medium and with arbitrary cross-sections. A mathematical formalism for source expansion in terms of cylindrical harmonics is also introduced and applied to the analysis of wireless communication along the realistic tunnels. Finally, in Chapter 6, we summarize the main contributions of the methods investigated in this research and also suggest some activities for future work.

2
Electromagnetic Fields in Anisotropic Cylindrical Structures

2.1
Introduction

This chapter presents a mathematical solution for the electromagnetic fields in cylindrical coordinates for uniaxially anisotropic and homogeneous media. We also present a mathematical formalism for the optical transformation theory [24,25] to map the eccentric coaxial guide to a conventional coaxial guide in a new coordinate system. The field solution in terms of cylindrical harmonics presented herein is the basis for the semi-analytical methods that will be examined in the following chapters of this Thesis.

2.2
Electromagnetic Fields in Cylindrical Waveguides

In this section we adopt a notation similar to that in [26, 27], where and time-harmonic dependence in the form $\exp(-i\omega t)$ is assumed and omitted. The objective here is to describe the electromagnetic fields in terms of cylindrical coordinates. The Maxwell's equations in differential forms are

$$\boldsymbol{\nabla} \times \mathbf{E} = i\omega\bar{\bar{\mu}} \cdot \mathbf{H}, \tag{2-1a}$$

$$\boldsymbol{\nabla} \times \mathbf{H} = -i\omega\bar{\bar{\epsilon}} \cdot \mathbf{E} + \mathbf{J}, \tag{2-1b}$$

$$\boldsymbol{\nabla} \cdot \left(\bar{\bar{\epsilon}} \cdot \mathbf{E}\right) = \varrho, \tag{2-1c}$$

$$\boldsymbol{\nabla} \cdot \left(\bar{\bar{\mu}} \cdot \mathbf{H}\right) = 0, \tag{2-1d}$$

where $\mathbf{E}$ and $\mathbf{H}$ are the electric and magnetic fields, respectively, and $\mathbf{J}$ and ϱ are the impressed electric current and charge densities, respectively. The medium considered here is homogeneous and uniaxially anisotropic, and characterized by the electric permittivity $\bar{\bar{\epsilon}}$ and magnetic permeability $\bar{\bar{\mu}}$ tensors represented by

$$\bar{\bar{p}} = \begin{bmatrix} p_s & 0 & 0 \\ 0 & p_s & 0 \\ 0 & 0 & p_z \end{bmatrix} \quad \text{with} \quad p = \{\mu, \epsilon\}. \tag{2-2}$$

In the above, we assume the medium defined in terms of cylindrical coordinates (ρ, ϕ, z), such the subscripts z and s are used to describe axial (along z) and transversal (to z) components, respectively.

2.2.1 Axial Fields

We can decompose the electromagnetic fields into axial and transversal components as follows:

$$\mathbf{G} = \mathbf{G}_s + \hat{z}G_z, \tag{2-3}$$

where $\mathbf{G}_s = \{\mathbf{E}_s, \mathbf{H}_s\}$ and $G_z = \{E_z, H_z\}$. In addition, we can write

$$\boldsymbol{\nabla} = \boldsymbol{\nabla}_s + \hat{z}\frac{\partial}{\partial z}, \tag{2-4}$$

where $\boldsymbol{\nabla}_s$ is a two-dimensional nabla operator given by

$$\boldsymbol{\nabla}_s = \hat{\rho}\frac{\partial}{\partial \rho} + \hat{\phi}\frac{1}{\rho}\frac{\partial}{\partial \phi}. \tag{2-5}$$

By taking the curl on (2-1a) and projecting the result in $\hat{z}$, we obtain

$$\hat{z} \cdot \Big[\boldsymbol{\nabla} \times (\boldsymbol{\nabla} \times \mathbf{E})\Big] = i\omega\hat{z} \cdot \Big[\boldsymbol{\nabla} \times (\bar{\bar{\mu}} \cdot \mathbf{H})\Big]. \tag{2-6}$$

The left-hand side of the above equation can be rewritten by using vector identities

$$\begin{aligned}\hat{z} \cdot \Big[\boldsymbol{\nabla} \times (\boldsymbol{\nabla} \times \mathbf{E})\Big] &= \hat{z} \cdot \Big[\boldsymbol{\nabla}(\boldsymbol{\nabla} \cdot \mathbf{E}) - (\boldsymbol{\nabla} \cdot \boldsymbol{\nabla})\mathbf{E}\Big] \\ &= \frac{\partial}{\partial z}(\boldsymbol{\nabla} \cdot \mathbf{E}) - \nabla^2 E_z,\end{aligned} \tag{2-7}$$

where ∇^2 is the scalar Laplacian operator in cylindrical coordinates given by

$$\nabla^2 = \frac{1}{\rho}\frac{\partial}{\partial \rho}\left(\rho\frac{\partial}{\partial \rho}\right) + \frac{1}{\rho^2}\frac{\partial^2}{\partial \phi^2} + \frac{\partial^2}{\partial z^2}. \tag{2-8}$$

By exploring the Gauss equation (2-1c), we can obtain

$$\begin{aligned}\boldsymbol{\nabla} \cdot (\bar{\bar{\epsilon}} \cdot \mathbf{E}) &= \left(\boldsymbol{\nabla}_s + \hat{z}\frac{\partial}{\partial z}\right) \cdot (\epsilon_s \mathbf{E} + \hat{z}\epsilon_z E_z) \\ &= \epsilon_s \boldsymbol{\nabla}_s \cdot \mathbf{E}_s + \epsilon_z \frac{\partial E_z}{\partial z} \\ &= \epsilon_s \boldsymbol{\nabla} \cdot \mathbf{E} - \epsilon_s \left(1 - \frac{\epsilon_z}{\epsilon_s}\right)\frac{\partial E_z}{\partial z} = 0.\end{aligned} \tag{2-9}$$

Using the above result in (2-7) allows us to obtain

$$\hat{z} \cdot \Big[\boldsymbol{\nabla} \times (\boldsymbol{\nabla} \times \mathbf{E})\Big] = \left(1 - \frac{\epsilon_z}{\epsilon_s}\right) \frac{\partial^2 E_z}{\partial z^2} - \nabla^2 E_z. \tag{2-10}$$

By using the Ampere's Law (2-1b) into the above, we can obtain

$$\begin{aligned} \hat{z} \cdot \Big[\boldsymbol{\nabla} \times (\boldsymbol{\nabla} \times \mathbf{E})\Big] &= i\omega \hat{z} \cdot \Big[\boldsymbol{\nabla} \times (\bar{\bar{\mu}} \cdot \mathbf{H})\Big] \\ &= i\omega \mu_s \hat{z} \cdot (\boldsymbol{\nabla} \times \mathbf{H}) \\ &= \omega^2 \mu_s \epsilon_z E_z. \end{aligned} \tag{2-11}$$

Finally, combining (2-10) and (2-11) sides, we have a wave equation for E_z given by

$$\begin{aligned} \nabla^2 E_z - \left(1 - \frac{\epsilon_z}{\epsilon_s}\right) \frac{\partial^2 E_z}{\partial z^2} + \omega^2 \mu_s \epsilon_z E_z = 0 \\ \nabla_s^2 E_z + \frac{\epsilon_z}{\epsilon_s} \frac{\partial^2 E_z}{\partial z^2} + \omega^2 \mu_s \epsilon_z E_z = 0, \end{aligned} \tag{2-12}$$

where ∇_s^2 is the two-dimensional Laplacian operator transversal in cylindrical coordinates:

$$\nabla_s^2 = \nabla^2 - \frac{\partial^2}{\partial z^2}. \tag{2-13}$$

Similarly, we can obtain a wave equation for H_z dual to (2-12), i.e,

$$\nabla_s^2 H_z + \frac{\mu_z}{\mu_s} \frac{\partial^2 H_z}{\partial z^2} + \omega^2 \mu_z \epsilon_s H_z = 0. \tag{2-14}$$

Equations (2-12) and (2-14) are Helmholtz differential equations in cylindrical coordinates for the axial fields E_z and H_z in an uniaxial medium described by the tensors (2-2). The variable separation method [26–28] will now be used to seek the solutions. By assuming a z-variation in the form of $\exp(ik_z z)$, we can write (2-12) and (2-14) in a compact form as follows:

$$\left(\nabla_s^2 + \frac{p_z}{p_s} k_\rho^2\right) G(\rho, \phi, z) = 0, \tag{2-15}$$

where $p = \{\mu, \epsilon\}$, $k_s^2 = \omega^2 \mu_s \epsilon_s$, $k_\rho^2 = k_s^2 - k_z^2$, and k_z is axial wavenumber. We can write $G = \{E_z, H_z\}$ as the product of three functions that depend on (ρ, ϕ, z), namely,

$$G(\rho, \phi, z) = B_n(\beta^{e,h}\rho)\Phi(n\phi)Z(k_z z), \tag{2-16}$$

where $\Phi(n\phi)$ and $Z(k_z z)$ are harmonic functions and $B_n(\beta^{e,h}\rho)$ is a linear combination of solutions to the Bessel differential equation of integer order $n = \{0, \pm 1, \pm 2, \dots\}$, i.e.[1]

$$B_n(\beta^{e,h}\rho) = A^n H_n(\beta^{e,h}\rho) + B^n J_n(\beta^{e,h}\rho), \tag{2-17}$$

where H_n and J_n are the first kind Hankel and Bessel functions of order n, A^n and B^n are constants to be found by enforcing the boundary conditions, $\beta^{e,h} = \alpha^{e,h} k_\rho$. We have also defined the anisotropy coefficients $\alpha^{e,h}$ given by

$$\alpha^e = \sqrt{\frac{\epsilon_z}{\epsilon_s}} \quad \text{and} \quad \alpha^h = \sqrt{\frac{\mu_z}{\mu_s}}. \tag{2-18}$$

The general solution for (2-15) can be written as

$$G(\rho, \phi, z) = \sum_{p=1}^{\infty} \sum_{n=-\infty}^{\infty} \Big[A^n H_n(\beta\rho) + B^n J_n(\beta\rho) \Big] e^{in\phi + ik_{z,np} z}, \tag{2-19}$$

where $\exp(ik_{z,np}z)$ indicates a wave propagating in the direction of positive z. It is important to emphasize that the azimuthal sum covers both negative and positive integers values of n. Another representation using sine and cosine functions is also possible, and in this case, the summation over positive integer values of n is preferable.

The above solution for cylindrical waveguides will be used as a starting point for the Regular Perturbation Method (RPM) and the Point-Matching Method (PMM) which will be detailed in the next Chapters 3 and 5, respectively. For the RPM, this solution is used entirely to solve the fields described as zeroth-order, and for the PMM it is used to expand the fields as a series of cylindrical harmonics and appropriately applied over a set of points to enforce the boundary conditions of the complex geometry.

2.2.2 Transversal Fields

The transversal (to z) field components can be determined from the axial ones (E_z e H_z) bt starting from the Faraday's (2-1a) and Ampere's (2-1b) Laws:

[1]Notice that the first-kind Hankel function is usually denoted by $H_n^{(1)}(\cdot)$. To shorten the notation, we drop the superscript (1) here. Note that any linear combination of a pair of linear independent solutions for the Bessel differential equation of integer order n could be used in the solution of (2-17). In particular, the solution may be alternatively written as a linear combination of a Bessel function and a Newman function, i.e., $B_n(\cdot) = A^n J_n(\cdot) + B^n Y_n(\cdot)$, or of a pair of first- and second-kind Hankel functions.

$$\boldsymbol{\nabla}_s \times (\hat{z}E_z) + ik_z\hat{z} \times \mathbf{E}_s = i\omega\mu_s\mathbf{H}_s, \tag{2-20a}$$

$$\boldsymbol{\nabla}_s \times (\hat{z}H_z) = i\omega\mu_z H_z, \tag{2-20b}$$

$$\boldsymbol{\nabla}_s \times (\hat{z}H_z) + ik_z\hat{z} \times \mathbf{H}_s = -i\omega\epsilon_s\mathbf{E}_s, \tag{2-21a}$$

$$\boldsymbol{\nabla}_s \times (\hat{z}E_z) = -i\omega\epsilon_z E_z. \tag{2-21b}$$

By taking the $\hat{z}\times$ in both sides of (2-20a) and replacing (2-21a) in right-hand side of the resulting equation, we can obtain

$$\hat{z} \times \boldsymbol{\nabla}_s \times (\hat{z}E_z) + ik_z\hat{z} \times \hat{z} \times \mathbf{E}_s = \frac{i\omega\mu_s}{ik_z}\left(-\boldsymbol{\nabla}_s \times (\hat{z}H_z) - i\omega\epsilon_s\boldsymbol{E}_s\right). \tag{2-22}$$

The left-hand side of the above is readily simplifies via the vector identity

$$\mathbf{A} \times \mathbf{B} \times \mathbf{C} = \mathbf{B}(\mathbf{A} \cdot \mathbf{C}) - \mathbf{C}(\mathbf{A} \cdot \mathbf{B}). \tag{2-23}$$

After some mathematical manipulations, we can obtain the transverse electric field

$$\mathbf{E}_s = \frac{1}{k_\rho^2}\Big[ik_z\boldsymbol{\nabla}_s E_z + i\omega\mu_s\boldsymbol{\nabla}_s \times (\hat{z}H_z)\Big]. \tag{2-24}$$

Similarly, a dual equation can be obtained for the transverse magnetic field:

$$\mathbf{H}_s = \frac{1}{k_\rho^2}\Big[ik_z\boldsymbol{\nabla}_s H_z - i\omega\epsilon_s\boldsymbol{\nabla}_s \times (\hat{z}E_z)\Big]. \tag{2-25}$$

2.3 Selected Case Studies (to be Solved)

The electromagnetic field described in terms of cylindrical harmonics will be employed in this thesis for the analysis of the case studies listed below:

- Anisotropic coaxial waveguides with small eccentricities.
- Eccentric partially-filled circular waveguides.
- The electromagnetic propagation in non-circular invaded boreholes and tunnels and boreholes.

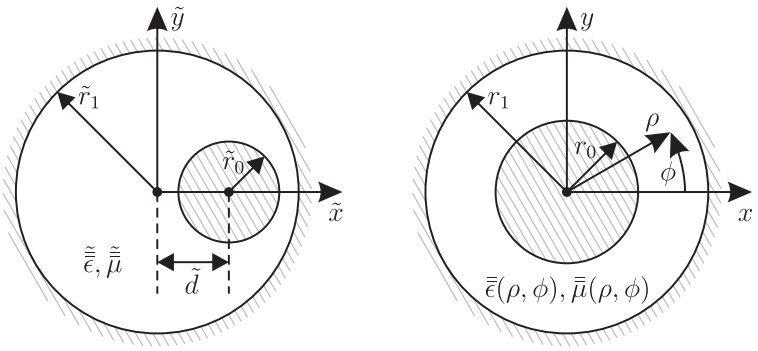

2.1(a): 2.1(b):

Figure 2.1: (a) Geometry of an eccentric coaxial waveguide in the plane $\tilde{z} = 0$. (b) Geometry of the transformed waveguide in the plane $z = 0$. Perfect electric conductors are indicated by the stripes.

2.3.1 Transformation Optics

In this section, we describe the transformation optics (TO) technique for helping us modeling eccentric circular boundary-value problems. Consider the cross-section of an eccentric coaxial waveguide (see Fig. 2.1(a)) located on a $\tilde{z}$-plane, where the outer and inner radii are represented by $\tilde{r}_1$ e $\tilde{r}_0$, respectively, $\tilde{d}$ represents the distance between the centers of each cylinder and the anisotropic medium is characterized by electrical permittivity tensor $\tilde{\bar{\epsilon}} = \text{diag}(\tilde{\epsilon}_s, \tilde{\epsilon}_s, \tilde{\epsilon}_z)$ and magnetic permeability tensor $\tilde{\bar{\mu}} = \text{diag}(\tilde{\mu}_s, \tilde{\mu}_s, \tilde{\mu}_z)$. Fig. 2.1(b) shows the cross-section of a conventional coaxial waveguide resulting from a conformal mapping as applied to the guide in Fig. 2.1(a). The new waveguide located on the z-plane has inner r_0 and outer r_1 radii and non-homogeneous anisotropic medium characterized in polar coordinate by $\bar{\bar{\epsilon}}(\rho, \phi)$ e $\bar{\bar{\mu}}(\rho, \phi)$.

The theory of transformation optics used in this work assumes that the relation between planes tilde and non-tilde is given by [24]

$$s = \tilde{x}_2 \frac{r_1}{\tilde{r}_1} \frac{\tilde{s} - \tilde{x}_1}{\tilde{s} - \tilde{x}_2}, \tag{2-26}$$

where $\tilde{x}_1$ e $\tilde{x}_2$ are the roots of the equations

$$\begin{cases} \tilde{x}_1 \tilde{x}_2 = \tilde{r}_1^2 \\ (\tilde{x}_1 - \tilde{d})(\tilde{x}_2 - \tilde{d}) = \tilde{r}_0^2, \end{cases} \tag{2-27}$$

to give

$$\tilde{x}_2 = \tilde{a} - (\tilde{a}^2 - \tilde{r}_1^2)^{1/2}, \text{ with } \tilde{a} = (\tilde{r}_1^2 - \tilde{r}_0^2 + \tilde{d}^2)/(2\tilde{d}), \tag{2-28}$$

$$\tilde{x}_1 = \tilde{r}_1^2/\tilde{x}_2. \tag{2-29}$$

The original eccentric electromagnetic problem depicted in Fig. 2.1(a) can be transformed into the concentric geometry depicted in Fig. 2.1(b) by using transformation optics principles [29–32]. As noted in [33], the electromagnetic problem in the non-tilde coordinates (x, y, z) can be related to the one in $(\tilde{x}, \tilde{y}, \tilde{z})$ through the mapping below

$$\mathbf{G} = \bar{\bar{J}} \cdot \tilde{\mathbf{G}}, \tag{2-30}$$

$$\bar{\bar{p}} = |\bar{\bar{J}}|^{-1} \bar{\bar{J}} \cdot \bar{\bar{\tilde{p}}} \cdot \bar{\bar{J}}^T, \tag{2-31}$$

where the electric and magnetic fields are represented by $\mathbf{G} = \{\mathbf{E}, \mathbf{H}\}$, respectively, $\bar{\bar{\mu}}$ and $\bar{\bar{\epsilon}}$ are the permeability and permittivity tensors in the transformed space represented by $\bar{\bar{p}} = \{\bar{\bar{\mu}}, \bar{\bar{\epsilon}}\}$, and $\bar{\bar{J}}$ is the associated Jacobian transformation matrix. By assuming $r_1 = \tilde{r}_1$, we can express the transformed constitutive tensors via [33]

$$\bar{\bar{p}} = \begin{bmatrix} \tilde{p}_s & 0 & 0 \\ 0 & \tilde{p}_s & 0 \\ 0 & 0 & |\bar{\bar{J}}|^{-1}\tilde{p}_z \end{bmatrix} \quad \text{with} \quad p = \{\mu, \epsilon\}. \tag{2-32}$$

We can write $\bar{\bar{J}}$ as

$$\bar{\bar{J}} = \bar{\bar{R}}(\phi) \cdot \bar{\bar{J}}_{xyz} \cdot \bar{\bar{R}}^T(\tilde{\phi}), \tag{2-33}$$

where $\bar{\bar{J}}_{xyz}$ is the Jacobian transformation tensor that transforms $(\tilde{x}, \tilde{y}, \tilde{z}) \rightarrow (x, y, z)$ and $\bar{\bar{R}}$ is the matrix that transforms the components from Cartesian to cylindrical, given by

$$\bar{\bar{J}}_{xyz} = \begin{bmatrix} \frac{\partial x}{\partial \tilde{x}} & \frac{\partial x}{\partial \tilde{y}} & \frac{\partial x}{\partial \tilde{z}} \\ \frac{\partial y}{\partial \tilde{x}} & \frac{\partial y}{\partial \tilde{y}} & \frac{\partial y}{\partial \tilde{z}} \\ \frac{\partial z}{\partial \tilde{x}} & \frac{\partial z}{\partial \tilde{y}} & \frac{\partial z}{\partial \tilde{z}} \end{bmatrix} \quad \text{and} \quad \bar{\bar{R}}(\phi) = \begin{bmatrix} \cos\phi & \sin\phi & 0 \\ -\sin\phi & \cos\phi & 0 \\ 0 & 0 & 1 \end{bmatrix}. \tag{2-34}$$

It is important to emphasize that the mapping above satisfies the Cauchy-Riemann conditions [32, 34], i.e.,

$$\frac{\partial x}{\partial \tilde{x}} = \frac{\partial y}{\partial \tilde{y}}, \quad \frac{\partial x}{\partial \tilde{y}} = -\frac{\partial y}{\partial \tilde{x}}, \tag{2-35}$$

and can also show that

$$\frac{\partial z}{\partial \tilde{z}} = 1, \quad \frac{\partial z}{\partial \tilde{x}} = \frac{\partial z}{\partial \tilde{x}} = 0 \quad \text{and} \quad \frac{\partial x}{\partial \tilde{z}} = \frac{\partial y}{\partial \tilde{z}} = 0. \tag{2-36}$$

By combining (2-34), (2-35), and (2-36) in (2-33), after some mathematical manipulations we can obtain

$$\bar{\bar{J}} = \begin{bmatrix} J_{11} & J_{12} & 0 \\ -J_{12} & J_{11} & 0 \\ 0 & 0 & 1 \end{bmatrix}, \tag{2-37}$$

where

$$J_{11} = \frac{\partial x}{\partial \tilde{x}} \cos(\phi - \tilde{\phi}) - \frac{\partial x}{\partial \tilde{y}} \sin(\phi - \tilde{\phi}), \tag{2-38}$$

$$J_{12} = \frac{\partial x}{\partial \tilde{x}} \sin(\phi - \tilde{\phi}) + \frac{\partial x}{\partial \tilde{y}} \cos(\phi - \tilde{\phi}). \tag{2-39}$$

The determinant of $\bar{\bar{J}}$ is readily given by

$$|\bar{\bar{J}}| = \left(\frac{\partial x}{\partial \tilde{x}}\right)^2 + \left(\frac{\partial x}{\partial \tilde{y}}\right)^2, \tag{2-40}$$

Recovering that $r_1 = \tilde{r}_1$, equation (2-26) provides

$$\frac{\partial x}{\partial \tilde{x}} = \left[(\tilde{x} - \tilde{x}_2)^2 - \tilde{y}^2\right] \frac{\tilde{x}_2(\tilde{x}_1 - \tilde{x}_2)}{\left[(\tilde{x} - \tilde{x}_2)^2 + \tilde{y}^2\right]^2}, \tag{2-41}$$

$$\frac{\partial x}{\partial \tilde{y}} = 2\tilde{y}(\tilde{x} - \tilde{x}_2) \frac{\tilde{x}_2(\tilde{x}_1 - \tilde{x}_2)}{\left[(\tilde{x} - \tilde{x}_2)^2 + \tilde{y}^2\right]^2}. \tag{2-42}$$

The inverse of the Jacobian determinant $|\bar{\bar{J}}|^{-1}$ can expressed in polar coordinates in the s-plane [33, 35]. From (2-26), we have

$$J = \frac{ds}{d\tilde{s}} = \frac{\tilde{x}_2(\tilde{x}_1 - \tilde{x}_2)}{(\tilde{s} - \tilde{x}_2)^2}. \tag{2-43}$$

Since $\tilde{s} = \tilde{x}_2(s - \tilde{x}_1)/(s - \tilde{x}_2)$, we have

$$\begin{aligned} \frac{ds}{d\tilde{s}} &= \frac{(s - \tilde{x}_2)^2}{\tilde{x}_2(\tilde{x}_2 - \tilde{x}_1)}, \\ \left|\frac{ds}{d\tilde{s}}\right| &= \frac{(x^2 + y^2 - 2x\tilde{x}_2 + \tilde{x}_2^2)^2}{\tilde{x}_2^2(\tilde{x}_2 - \tilde{x}_1)^2}, \\ |J| &= \frac{(1 - 2\rho\cos(\phi)/\tilde{x}_2 + \rho^2/\tilde{x}_2^2)^2}{(1 - \tilde{x}_1/\tilde{x}_2)^2}. \end{aligned} \tag{2-44}$$

Finally, we can obtain

$$|\bar{\bar{J}}|^{-1} = \frac{(1-\tilde{x}_1/\tilde{x}_2)^2}{(1-2\rho\cos(\phi)/\tilde{x}_2+\rho^2/\tilde{x}_2^2)^2}. \tag{2-45}$$

3
Regular Perturbation Method

3.1
Introduction

In this chapter, we present a perturbation solution for the Helmholtz equation associated with the electromagnetic fields in an anisotropic and inhomogeneous medium. Our method is parallel in some aspects to the Rayleigh-Schrodinger Perturbation Theory [36, Ch. 15], but is strongly inspired by the regular perturbation methods (RPMs) presented in [27, 33, 37, 38].

We can find in literature several works that have employed transformation optics principles [29, 39] to simplify the eccentric problem. In [40], the eigenvalue problem of an eccentric coaxial waveguide was solved via a conformal mapping combined with the finite-element method, while in [41] the conformal mapping was combined with a finite-difference method. In [42], the eccentric waveguide was analyzed by using a conformal transformation, and approximated formulas were obtained for expressing the field solutions in terms of cylindrical harmonics in the mapped (concentric) space. A similar technique was applied to analyze the propagating and evanescent modes in eccentric-core optical fibers in [43]. In [44], transformation optics was applied to solve eccentric cylindrical problems. In [33], transformation optics was used in conjunction with a perturbation series to analyze electromagnetic well-logging sensors in eccentric boreholes.

In this chapter, we present an efficient alternative approach by employing conformal transformation optics to map the original (eccentric) problem shown in Fig. 2.1(a) into a concentric waveguide shown in Fig. 2.1(b). Then, we solve the resulting wave equation in the transformed (concentric) domain by employing the methodology for approximating non-conventional differential equations described in [27, 37, 45]. A regular perturbation method (RPM) is then established and the field solutions are obtained as a power series with respect to the eccentricity parameter. We then solve three second-order differential equations to compute the zeroth-, first-, and second-order corrections for TM and TE modes of coaxial waveguides with small eccentricities. In addiction, we also employed a generalization of RPM for the case where

the inner conductor is replaced by an anisotropic rod. A key contribution from this work is the description of how to properly enforce the boundary and the orthogonality conditions to compute zeroth-, first-, and second-order corrections for transverse magnetic (TM), transverse electric (TE), and hybrid modes for such types of waveguides. Several scenarios are studied and validated against works in literature and brute-force methods as finite-element method (FEM) and finite-integration method (FIT).

3.2 Mathematical Formulation

Based on the conformal mapping theory described in Section 2.3.1, the transformed problem (Fig. 2.1(b)) is non-homogeneous with dependence (ρ, ϕ) characterized by $\bar{\bar{p}} = \mathrm{diag}(p_s, p_s, p_z(\rho, \phi))$. Since $p_z(\rho, \phi)$ is independent of z, we can assume the $\exp(\pm ik_z z)$ dependence for the fields propagating for $z \gtrless 0$, where k_z is the axial wavenumber.

The problem at hand can be solved by decomposing the electromagnetic fields into a sum of transverse magnetic to z (TM) and transverse electric to z (TE) modes [28, Sec. 3-12]. It is expedient to solve the axial E_z and H_z field components and then compute the transverse components of the fields in cylindrical coordinates. The wave equation for the axial electric and magnetic fields of the concentric scenario depicted in Fig. 2.1(b) satisfies

$$\left(\nabla_s^2 + \frac{p_z(\rho, \phi)}{p_s} k_\rho^2\right) G(\rho, \phi, z) = 0, \tag{3-1}$$

where ∇_s^2 is the transversal (to z) Laplacian operator in polar coordinates, $k_\rho^2 = k_s^2 - k_z^2$, $k_s^2 = \omega^2 \mu_s \epsilon_s$, $G = \{E_z, H_z\}$, and $p = \{\epsilon, \mu\}$. The radial and azimuthal dependence of p_z makes the above differential equation too complicated to be solved in closed-form. However, in view of (2-28) and (2-29), we can express the displacement $\tilde{d}$ and the radii $\tilde{r}_0$ and $\tilde{r}_1$ as a function of $\tilde{x}_2$ as depicted in Fig. 3.1. Notice that in the limit $\tilde{d} \to 0$, we have $\tilde{x}_1 \to 0$ and $\tilde{x}_2 \to \infty$. In this way, a perturbation solution can be sought by expanding p_z as the power series

$$p_z(\rho, \phi) = p_{0,z} \left[1 + \frac{4\rho}{\tilde{x}_2} \cos(\phi) + \frac{2\rho^2}{\tilde{x}_2^2} \left(3\cos(2\phi) + 2\right) + \mathcal{O}(\tilde{x}_2^{-3})\right], \tag{3-2}$$

where $p_{0,z} = \tilde{p}_z \left(1 - \tilde{x}_1/\tilde{x}_2\right)^2$. The solution for (3-1) can also be expressed as a

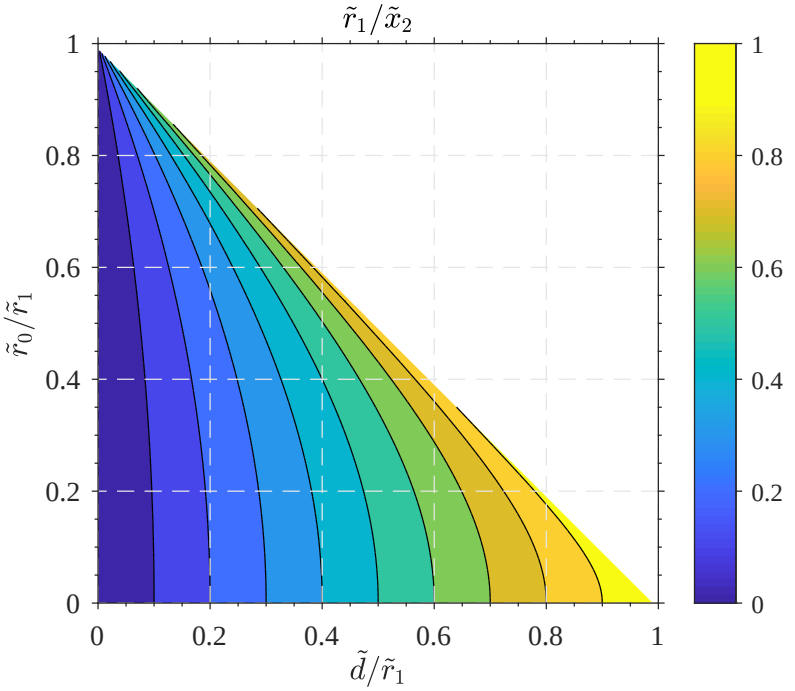

Figure 3.1: Relation between $\tilde{r}_1/\tilde{x}_2$ and geometric parameters $\tilde{d}$ and $\tilde{r}_0$ when $\tilde{r}_1$ is kept fixed.

power series in terms of $\tilde{x}_2^{-1}$ by assuming

$$G(\rho,\phi,z) = \left[G_0(\rho,\phi) + \sum_{j=1}^{\infty} \tilde{x}_2^{-j} G_j(\rho,\phi)\right] e^{ik_z z}, \tag{3-3}$$

$$k_z^2 = k_{0,z}^2 \left(1 + \sum_{j=1}^{\infty} \tilde{x}_2^{-j} \alpha_j\right), \tag{3-4}$$

for $z > 0$. In the above, G_0 and $k_{0,z}$ are the axial fields and axial wavenumber associated with the zeroth-order problem, i.e, with $\tilde{x}_2^{-1} \to 0$. Higher-order corrections are associated with the functions G_j and the constants α_j, with $j = \{1, 2, 3, \dots\}$.

By using (3-2), (3-3), and (3-4) into (3-1) and after some algebraic simplifications, we obtain

$$\left(\nabla_s^2 + \alpha_0^2 k_{0,\rho}^2\right) G_0 = 0, \tag{3-5a}$$

$$\left(\nabla_s^2 + \alpha_0^2 k_{0,\rho}^2\right) G_1 = \alpha_0^2 \left(\alpha_1 k_{0,z}^2 - 4\rho\cos(\phi) k_{0,\rho}^2\right) G_0, \tag{3-5b}$$

$$\begin{aligned}\left(\nabla_s^2 + \alpha_0^2 k_{0,\rho}^2\right) G_2 = \alpha_0^2 \Big[&\alpha_2 k_{0,z}^2 G_0 + 4\rho\cos(\phi)\alpha_1 k_{0,z}^2 G_0 \\ &- 2\rho^2 \left(3\cos(2\phi) + 2\right) k_{0,\rho}^2 G_0 \\ &+ \alpha_1 k_{0,z}^2 G_1 - 4\rho\cos(\phi) k_{0,\rho}^2 G_1\Big],\end{aligned} \tag{3-5c}$$

by retaining correction terms up to $\tilde{x}_2^0$, $\tilde{x}_2^{-1}$, and $\tilde{x}_2^{-2}$, respectively. Notice we have omitted the argument of G_j to simplify the notation and have introduced the constants $\alpha_0 = (p_{0,z}/p_s)^{1/2}$ and $k_{0,\rho}^2 = k_s^2 - k_{0,z}^2$. The computation of higher order terms is possible but mathematically cumbersome. In order to obtain the unknown functions G_j and constants α_j, we first solve G_0 in (3-5a). Next, G_1 can be obtained by solving (3-5b), where the enforcement of appropriate boundary conditions allows us to obtain the constant α_1. Similarly, we can obtain G_2 and α_2 in view of (3-5c).

3.3 Zeroth-Order Fields

The zeroth-order differential equation in (3-5a) has a well-known solution in terms of cylindrical and azimuthal harmonics [28, Ch. 5]. The axial fields G_0 correspond to a concentric coaxial waveguide filled with an uniaxial anisotropic media with constitutive tensors $\bar{\bar{p}}_0 = \mathrm{diag}(p_s, p_s, p_{0,z})$ with $p = \{\mu, \epsilon\}$. The elementary solution for (3-5a) can be written as [27]

$$G_0 = B_n(\beta\rho)e^{in\phi}, \tag{3-6}$$

where B_n is a linear combination of Bessel functions of integer order $n = \{0, \pm1, \pm2, \dots\}$ discussed earlier in the Section 2.2.1, given by

$$B_n(\beta\rho) = A_0^n H_n(\beta\rho) + B_0^n J_n(\beta\rho), \tag{3-7}$$

where H_n and J_n are the first kind Hankel and Bessel functions of order n, $\beta = \alpha_0 k_{0,\rho}$, and A_0^n and B_0^n are constants to be found by enforcing the boundary conditions of the zeroth-order fields at $\rho = r_0$ and $\rho = r_1$. In addition, the zeroth-order axial wavenumber $k_{0,z}$ satisfies $k_s^2 = k_{0,\rho}^2 + k_{0,z}^2$, with $\Im m(k_{0,z}) \geq 0$.

3.3.1 TM Fields

The boundary conditions $E_z = 0$ at $\rho = r_0$ and $\rho = r_1$ render

$$A_0^n = J_n(\beta r_1), \quad B_0^n = -H_n(\beta r_1), \tag{3-8}$$

with β satisfying

$$J_n(\beta r_1)H_n(\beta r_0) - H_n(\beta r_1)J_n(\beta r_0) = 0, \tag{3-9}$$

for $n = \{0, \pm1, \pm2, \dots\}$.

3.3.2 TE Fields

The boundary conditions $\partial H_z/\partial\rho = 0$ at $\rho = r_0$ and $\rho = r_1$ render

$$A_0^n = J_n'(\beta r_1), \quad B_0^n = -H_n'(\beta r_1), \tag{3-10}$$

with β satisfying

$$J_n'(\beta r_1)H_n'(\beta r_0) - H_n'(\beta r_1)J_n'(\beta r_0) = 0, \tag{3-11}$$

for $n = \{0, \pm1, \pm2, \dots\}$.

3.3.3 TEM Fields

A transverse electromagnetic to z (TEM) mode is supported in the concentric coaxial waveguide depicted in Fig. 2.1(b). In view of (3-1), we can obtain the TEM field components in the limit $k_\rho \to 0$ of an axisymmetric TM field, i.e., with $n = 0$. By assuming a current I_0 in the inner PEC conductor, it follows that

$$A_0^n = \frac{-I_0\beta^2}{4\omega\epsilon_s}, \quad B_0^n = 0, \tag{3-12}$$

and

$$E_z = \lim_{\beta\to 0} A_0^n H_0(\beta\rho)e^{ik_z z}. \tag{3-13}$$

By using the above, we can obtain all other field components from Maxwell's equations. Finally, in the limit $\beta \to 0$, we have $k_z = k_s$ with

$$E_\rho = \sqrt{\frac{\mu_s}{\epsilon_s}}\frac{I_0}{2\pi\rho}e^{ik_s z}, \tag{3-14}$$

$$H_\phi = \frac{I_0}{2\pi\rho}e^{ik_s z}, \tag{3-15}$$

supplemented by $E_\phi = E_z = 0$ and $H_\rho = H_z = 0$. These are the usual TEM fields of a coaxial waveguide, for $z > 0$ [46]. Since $k_\rho = 0$, no high-order corrections are expected for this field. Accordingly, in view of (3-3) and (3-4), the TEM field is associated with $G_j = 0$ and $\alpha_j = 0$, for $j > 0$.

3.4 First-Order Fields

By replacing (3-6) in (3-5b) and after some simplifications, we obtain

$$\left(\nabla_s^2 + \beta^2\right) G_1 = \alpha_1 \frac{p_{0,z}}{p_s} k_{0,z}^2 B_n(\beta\rho) e^{in\phi} - 2\beta^2 \rho B_n(\beta\rho) \left(e^{i(n+1)\phi} + e^{i(n-1)\phi}\right). \tag{3-16}$$

The general solution for G_1 is a combination of the homogeneous G_1^h solution and a particular G_1^p solution. The orthogonality of the azimuthal harmonic functions present in the nonhomogeneous solution allows us to use the ansatz [38, eq. (11)]

$$G_1^p = R_1^n(\rho)\, e^{in\phi} + R_1^{n-1}(\rho)\, e^{i(n-1)\phi} + R_1^{n+1}(\rho)\, e^{i(n+1)\phi}, \tag{3-17}$$

where $R_1^m(\rho)$, for $m = \{n, n \pm 1\}$, are ρ-dependent functions. Consequently, we can show that the homogeneous solution satisfies

$$\left(\nabla_s^2 + \beta^2\right) G_1^h = L_n G_1^n e^{in\phi} + L_{n+1} G_1^{n+1} e^{i(n+1)\phi} + L_{n-1} G_1^{n-1} e^{i(n-1)\phi}, \tag{3-18}$$

where we have introduced the Bessel differential operator

$$L_m = \frac{d^2}{d\rho^2} + \frac{1}{\rho}\frac{d}{d\rho} + \beta^2 - \frac{m^2}{\rho^2}, \quad \text{for} \quad m = n, n \pm 1. \tag{3-19}$$

By noting the linear independence of the $e^{im\phi}$ terms, the solution of (3-18) can be written as combination of cylindrical function of order m, i.e.

$$G_1^m = A_1^m H_m(\beta\rho) + B_1^m J_m(\beta\rho), \tag{3-20}$$

where $m = \{n, n \pm 1\}$. Again, the constants A_1^m and B_1^m follow from the boundary conditions.

The particular solution G_1^p in (3-17) is found on comparing $L_m[R_1^m(\rho)e^{im\phi}]$ with their counterparts in (3-16):

$$L_n R_1^n = \alpha_1 \frac{p_{0,z}}{p_s} k_{0,z}^2 B_n(\beta\rho), \tag{3-21a}$$

$$L_{n+1} R_1^{n+1} = -2\beta^2 \rho B_n(\beta\rho), \tag{3-21b}$$

$$L_{n-1} R_1^{n-1} = -2\beta^2 \rho B_n(\beta\rho). \tag{3-21c}$$

The above equations can solved by using the results of the operator L_m over $\rho^q B_p(\beta\rho)$ available in [27, 45], where B_p is a linear combination of cylindrical

function with integer order p, and m, p, and q are parameters to be matched. Then, after some simplifications, we obtain the general solution as

$$\begin{aligned} G_1 = &\left[A_1^n H_n + B_1^n J_n - \alpha_1 \frac{p_{0,z}}{p_s} k_{0,z}^2 \frac{\rho}{2\beta} B_n'\right] e^{in\phi} \\ &+ \left[A_1^{n+1} H_{n+1} + B_1^{n+1} J_{n+1} + \frac{\beta}{2}\rho^2 B_{n-1}\right] e^{i(n+1)\phi} \\ &+ \left[A_1^{n-1} H_{n-1} + B_1^{n-1} J_{n-1} - \frac{\beta}{2}\rho^2 B_{n+1}\right] e^{i(n-1)\phi}, \end{aligned} \tag{3-22}$$

where B_n' is the first derivative of (3-7) with respect to the argument and $B_{n\pm1}$ is given by (3-7) but with cylindrical functions of order $n \pm 1$. To shorten the notation, we drop the argument $(\beta\rho)$ of all cylindrical functions, restoring it later as needed. As noted, the constants α_1, A_1^m and B_1^m are obtained by enforcing the boundary conditions of the first-order fields at $\rho = r_0$ and $\rho = r_1$. The boundary conditions split up into three independent equations because of the azimuthal orthogonality. For the fields with $\exp(in\phi)$ factors, only the trivial solution with $\alpha_1 = 0$ and $A_1^n = B_1^n = 0$ is possible. As a consequence, there is no first-order correction for the axial wavenumber k_z. For the fields with $\exp(i(n \pm 1)\phi)$ factors, we obtain non-zero $A_1^{n\pm1}$ and $B_1^{n\pm1}$ by enforcing $E_z = 0$ and $\partial H_z/\partial\rho = 0$ at $\rho = r_0$ and $\rho = r_1$. Accordingly, the first-order axial fields can be written in a compact form as

$$G_1 = G_1^{n+1} e^{i(n+1)\phi} + G_1^{n-1} e^{i(n-1)\phi}, \tag{3-23}$$

where

$$G_1^{n\pm1}(\beta\rho) = B_{n\pm1}^{1\pm}(\beta\rho) \pm \frac{\beta}{2}\rho^2 B_{n\mp1}(\beta\rho), \tag{3-24}$$

with

$$B_{n\pm1}^{1\pm}(\beta\rho) = A_1^{n\pm1} H_{n\pm1}(\beta\rho) + B_1^{n\pm1} J_{n\pm1}(\beta\rho). \tag{3-25}$$

Note that the argument of cylindrical functions in (3-24) and (3-25) have been restored for clarity.

3.5 Second-Order Fields

By replacing (3-6) and (3-23) in (3-5c), and after some simplifications, we obtain

$$\begin{aligned}\left(\nabla_s^2+\beta^2\right)G_2 = &\left(F_1B_n-\frac{F_2}{2}G_1^{n+1}-\frac{F_2}{2}G_1^{n-1}\right)e^{in\phi}\\ &-\left(\frac{F_3}{2}B_n+\frac{F_2}{2}G_1^{n+1}\right)e^{i(n+2)\phi}\\ &-\left(\frac{F_3}{2}B_n+\frac{F_2}{2}G_1^{n-1}\right)e^{i(n-2)\phi},\end{aligned} \tag{3-26}$$

where

$$F_1=\alpha_0^2\left(\alpha_2k_{0,z}^2-4\rho^2k_{0,\rho}^2\right), \tag{3-27}$$

$$F_2=\alpha_0^2 4\rho k_{0,\rho}^2, \tag{3-28}$$

$$F_3=\alpha_0^2 6\rho^2 k_{0,\rho}^2. \tag{3-29}$$

The general second-order solution can be written as a combination of homogeneous and particular solutions, that is, $G_2=G_2^h+G_2^p$. Again, the orthogonality in terms of ϕ in the nonhomogeneous parcel allows us to introduce the ansatz

$$G_2^p(\rho,\phi)=R_2^n\,e^{in\phi}+R_2^{n+2}\,e^{i(n+2)\phi}+R_2^{n-2}\,e^{i(n-2)\phi}, \tag{3-30}$$

where $R_2^m(\rho)$, for $m=\{n,n\pm2\}$, are ρ-dependent functions. The homogeneous solution now satisfies

$$\begin{aligned}\left(\nabla_s^2+\beta^2\right)G_2^h = &L_nG_2^ne^{in\phi}+L_{n+2}G_2^{n+2}e^{i(n+2)\phi}\\ &+L_{n-2}G_2^{n-2}e^{i(n-2)\phi},\end{aligned} \tag{3-31}$$

which can be solved by using

$$G_2^m=A_2^mH_m(\beta\rho)+B_2^mJ_m(\beta\rho), \tag{3-32}$$

with A_2^m and B_2^m determined from the boundary conditions. Next, by comparing (3-26) with (3-30), we obtain

$$L_nR_2^n=F_1B_n-\frac{F_2}{2}G_1^{n+1}-\frac{F_2}{2}G_1^{n-1}, \tag{3-33a}$$

$$L_{n+2}R_2^{n+2}=-\left(\frac{F_3}{2}B_n+\frac{F_2}{2}G_1^{n+1}\right), \tag{3-33b}$$

$$L_{n-2}R_2^{n-2}=-\left(\frac{F_3}{2}B_n+\frac{F_2}{2}G_1^{n-1}\right). \tag{3-33c}$$

Again, using the results of the operator L_m over $\rho^q B_p(\beta\rho)$ available in [27] we obtain the general solution. In Appendix A the process for determining the second-order solution is described in more detail. However, the general solution is given by

$$\begin{aligned} G_2(\rho,\phi) = &\Big[A_2^n H_n + B_2^n J_n - \alpha_2 F + P\Big] e^{in\phi} \\ &+ \Big[A_2^{n+2} H_{n+2} + B_2^{n+2} J_{n+2} + \Omega_+\Big] e^{i(n+2)\phi} \\ &+ \Big[A_2^{n-2} H_{n-2} + B_2^{n-2} J_{n-2} - \Omega_-\Big] e^{i(n-2)\phi}, \end{aligned} \tag{3-34}$$

where

$$F(\beta\rho) = \alpha_0^2 k_{0,z}^2 \frac{\rho}{2\beta} B_n'(\beta\rho), \tag{3-35}$$

$$\begin{aligned} P(\beta\rho) = &-\frac{\beta^2}{4}\rho^4 B_n(\beta\rho) \\ &+ \frac{\beta}{2}\rho^2 \left[B_{n-2}^{1-}(\beta\rho) - B_{n+2}^{1+}(\beta\rho)\right], \end{aligned} \tag{3-36}$$

$$\begin{aligned} \Omega_\pm(\beta\rho) = &\frac{\beta}{2}\rho^2 B_n^{1\pm}(\beta\rho) + \frac{\beta}{2}\rho^3 B_{n\mp1}(\beta\rho) \\ &+ \frac{\beta^2}{8}\rho^4 B_{n\mp2}(\beta\rho). \end{aligned} \tag{3-37}$$

Note that in (3-36), $B_{n\pm2}^{1\pm}$ is given by (3-25) but with cylindrical functions of order $n \pm 2$. In (3-37), $B_{n\pm2}$ is given by (3-7) but with cylindrical functions of order $n \pm 2$. Also, the argument of cylindrical functions in (3-35), (3-36) and (3-37) have been restored for clarity.

The boundary conditions can be split up into three independent equations because of the azimuthal orthogonality, but the presence of the function P makes the trivial solution $\alpha_2 = 0$ and $A_2^n = B_2^n = 0$ impossible. Consequently, the term associated with $\exp(in\phi)$ in (3-34) will be present, and we have *three* constants to be determined, namely, α_2, A_2^n and B_2^n. *Two* linearly independent equations are obtained by enforcing the boundary conditions of the second-order fields associated with $\exp(in\phi)$ at $\rho = r_0$ and $\rho = r_1$. In addition, we should enforce the orthogonality between G_2 and G_0 in the polar domain $r_0 < \rho < r_1$ and $0 < \phi < 2\pi$ to obtain an additional constraint equation. Note that the orthogonality between functions G_2 and G_1 is trivially satisfied when examining their azimuthal dependencies.

For the fields in terms of $\exp(i(n \pm 2)\phi)$, we can obtain non-zero $A_2^{n\pm2}$ and $B_2^{n\pm2}$ by enforcing $E_z = 0$ and $\partial H_z/\partial\rho = 0$ at $\rho = r_0$ and $\rho = r_1$.

3.5.1 Orthogonality Condition

Based on the cross-sectional inner product

$$\langle f, g\rangle_{\rho\phi} = \int_0^{2\pi}\int_{r_0}^{r_1} f(\rho,\phi)\, g^*(\rho,\phi)\, \rho\, d\rho\, d\phi, \tag{3-38}$$

the orthogonality between G_2 and G_0 requires

$$\langle G_2(\rho,\phi), G_0(\rho,\phi)\rangle_{\rho\phi} = 0 \tag{3-39}$$

for all $n = 0, \pm1, \pm2, \ldots$. By substituting (3-6) and (3-34) in the above, after solving the integral over ϕ, we obtain

$$\alpha_2 = \alpha_2^H A_2^n + \alpha_2^J B_2^n + \alpha_2^P, \tag{3-40}$$

where

$$\alpha_2^H = \frac{\langle B_n, H_n\rangle_\rho}{\langle B_n, F\rangle_\rho},\ \alpha_2^J = \frac{\langle B_n, J_n\rangle_\rho}{\langle B_n, F\rangle_\rho},\ \alpha_2^P = \frac{\langle B_n, P\rangle_\rho}{\langle B_n, F\rangle_\rho}, \tag{3-41}$$

with

$$\langle f, g\rangle_\rho = \int_{r_0}^{r_1} f(\rho)\, g^*(\rho)\, \rho\, d\rho. \tag{3-42}$$

Notice that (3-40) is supplemented by other two conditions at $\rho = r_0$ and $\rho = r_1$. In case of a TM^z field, we have

$$A_2^n H_n(\beta r_0) + B_2^n J_n(\beta r_0) - \alpha_2 F(\beta r_0) + P(\beta r_0) = 0, \tag{3-43}$$
$$A_2^n H_n(\beta r_1) + B_2^n J_n(\beta r_1) - \alpha_2 F(\beta r_1) + P(\beta r_1) = 0. \tag{3-44}$$

Then, we obtain α_2, A_2^n and B_2^n by solving the linear system of equations (3-40), (3-43), and (3-44).

In case of a TE^z field, we have

$$A_2^n H_n'(\beta r_0) + B_2^n J_n'(\beta r_0) - \alpha_2 F'(\beta r_0) + P'(\beta r_0) = 0, \tag{3-45}$$
$$A_2^n H_n'(\beta r_1) + B_2^n J_n'(\beta r_1) - \alpha_2 F'(\beta r_1) + P'(\beta r_1) = 0, \tag{3-46}$$

where the $'$ represents derivative with respect to the argument. Finally, α_2, A_2^n and B_2^n are given by solving the linear system of equations (3-40), (3-45) and (3-46).

3.6 Numerical Results

In order to validate our method, we consider a waveguide with $\tilde{r}_1 = 5$ mm, $\tilde{r}_0 = 0.05\tilde{r}_1$ and the eccentricity $\tilde{d}_0 = 0.05\tilde{r}_1$, assuming the medium as vacuum. This problem was considered before in [7] and is used to evaluate the accuracy of the perturbation series obtained here. Table 3.1 shows the cutoff wavenumbers $k_{\rho c} = (\omega^2\epsilon_s\mu_s - k_z^2)^{1/2}$ for the dominant TE_{np} and TM_{np} modes obtained by (a) the finite-element method (FEM) from CST Studio Suite [2], (b) the regular perturbation method (RPM), and (c) reference [7]. Relative errors were computed using the FEM solution as a reference. Good agreement is observed among the different methods. The RPM results have relative error no larger than 0.020%, while the observed error in the technique present in [7] varies in the range of 0.194% to 0.633%.

To further investigate the accuracy of the perturbation solutions presented here, we consider the same waveguide considered before, but now with different eccentricity offsets $\tilde{d} = \{0.10\tilde{r}_1, 0.15\tilde{r}_1, 0.20\tilde{r}_1\}$. This choice was motivated because the perturbation parameter $\tilde{x}_2$ is more sensitive to $\tilde{d}$, as shown in Fig. 3.1. Fig. 3.2 shows the cutoff wavenumber of the principal modes as a function of the normalized offsets $\tilde{d}/\tilde{r}_1$. The results obtained via the perturbation solutions show good agreement with those from FEM when $\tilde{d}/\tilde{r}_1$ is less than 2.6% but, as expected, gradually deteriorates as the eccentricity distance increases. Still, the RPM provides good approximation in all the tested cases. For example, the TM_{01} results show a relative error of only 2.6% for $\tilde{d}/\tilde{r}_1 = 20\%$.

The effect of the eccentricity $\tilde{d}$ in the field distributions over the waveguide cross-section can also be evaluated by the RPM. Fig. 3.3 shows the normalized axial magnetic field patterns for the TE_{11} and TE_{21} modes with $\tilde{r}_0 = 0.05\tilde{r}_1$ and $\tilde{d} = 0.05\tilde{r}_1$. Good agreement is observed versus the FEM results. In addition, Fig. 3.4 compares the axial electric field of the TM_{01} mode as $\tilde{d}$ increases. Good agreement is again observed versus the FEM results, but small deviations become apparent when $\tilde{d} = 0.15\tilde{r}_1$ as a consequence of the limited azimuth variations the second-order correction in (3-34) provides.

Finally, we consider waveguides filled with anisotropic materials, described by $\tilde{\epsilon}_s = \epsilon_0\tilde{\epsilon}_{rs}$, $\tilde{\epsilon}_z = \epsilon_0\tilde{\epsilon}_{rz}$, and $\tilde{\mu}_s = \tilde{\mu}_z = \tilde{\mu}_0$, where ϵ_0 and μ_0 are the vacuum values. The geometry has $\tilde{r}_1 = 5$ mm, $\tilde{r}_0 = 0.05\tilde{r}_1$, and a large eccentricity offset $\tilde{d} = 0.2\tilde{r}_1$. Fig. 3.5 shows results for the cutoff wavenumbers of the TM_{01} mode as a function of $\tilde{\epsilon}_{rs}$ and $\tilde{\epsilon}_{rs}$. As a reference solution, we use the finite-integration technique (FIT) from [2] and the RPM solution.

The computational cost for solving the first 15 cutoff wavenumbers

(including TEM, TM and TE modes) required by the presented perturbation methods is compared with that of FIT in Table 3.2 for the anisotropic waveguide with $\tilde{\epsilon}_{rs} = 5$ and $\tilde{\epsilon}_{rz} = 1$ (case 1). In addition, Table 3.3 show the CPU time and memory required for the problem with $\tilde{\epsilon}_{rs} = 1$ and $\tilde{\epsilon}_{rz} = 5$ (case 2). Our numerical results were obtained using a Matlab code running on a PC with a 3.40-GHz Intel Core i7-4930K processor. In contrast, the FIT results were obtained using a dedicated HP Z800 Workstation with a dual quad-core 2.40-GHz Intel Xeon E5620 processor. Notice we have computed only the port modes by using the standard options in the FIT solver of CST [2].

Table 3.1: Cutoff wavenumbers obtained by the FEM from [2], results from [7], and from RPM. The relative errors were computed using the FEM solution as reference.

	FEM	RPM		Work in [7]	
Mode	$k_{\rho c}$ (m^{-1})	$k_{\rho c}$ (m^{-1})	Error (%)	$k_{\rho c}$ (m^{-1})	Error (%)
TE_{11}	366.156	366.230	0.020	367.226	0.292
TE_{21}	610.692	610.796	0.017	612.837	0.351
TE_{31}	840.159	840.234	0.009	842.354	0.261
TM_{01}	610.692	610.674	-0.003	614.559	0.633
TM_{11}	775.540	775.698	0.020	774.038	-0.194
TM_{21}	1027.331	1027.383	0.005	1029.802	0.241

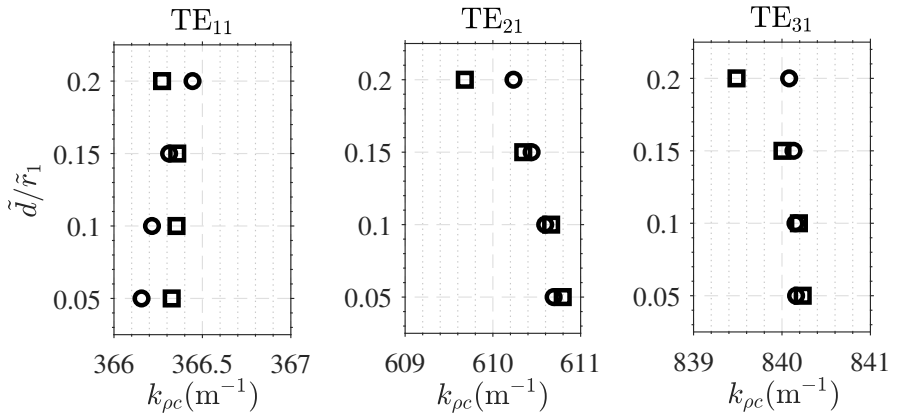

3.2(a):

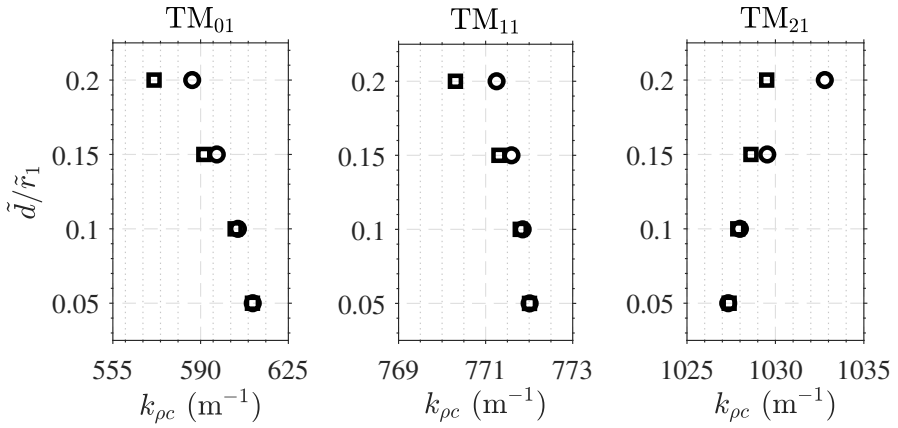

3.2(b):

Figure 3.2: Cutoff wavenumbers for (a) TE and (b) TM modes as a function of the normalized eccentricity distance $\tilde{d}/\tilde{r}_1$ obtained by FEM ($\circ$) and by RPM ($\square$).

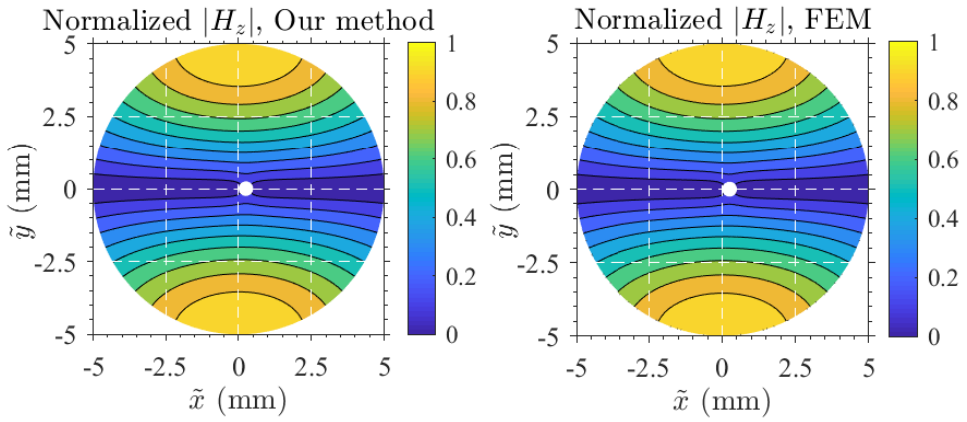

3.3(a):

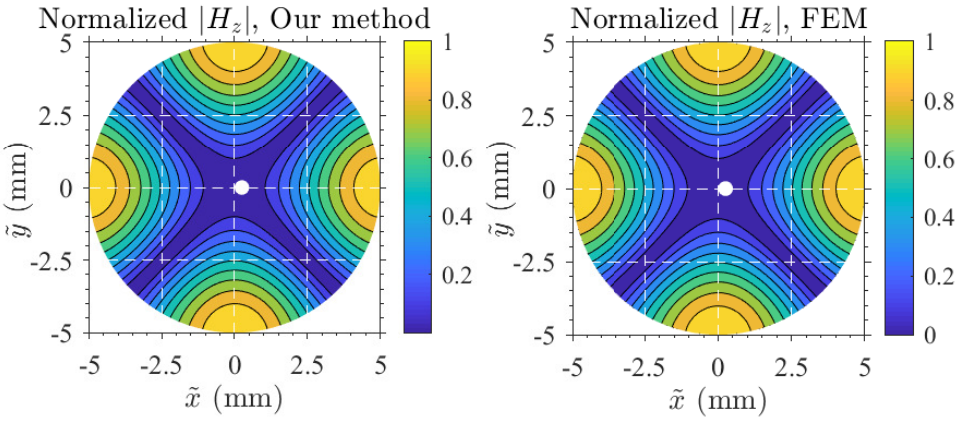

3.3(b):

Figure 3.3: Normalized axial magnetic field patterns for TE_{11} and TE_{21} modes calculated by using the RPM (left) and by FEM [2] (right). (a) TE_{11} mode. (b) TE_{21} mode.

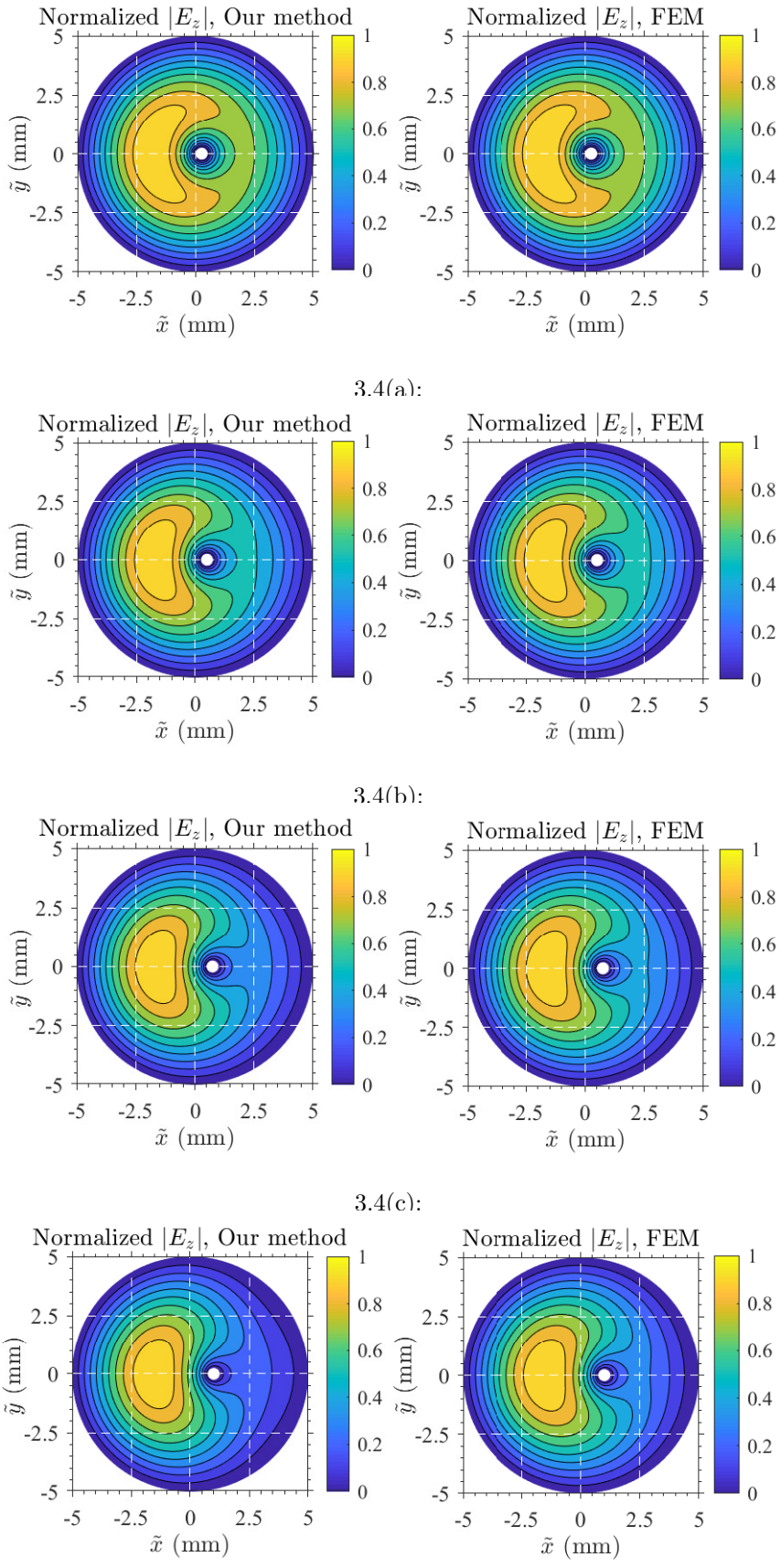

3.4(a):

3.4(b):

3.4(c):

3.4(d):

Figure 3.4: Normalized axial electric field patterns for the TM_{01} mode calculated by using the RPM (left) and by FEM from [2] (right) for different values of the eccentricities $\tilde{d}$. (a) $\tilde{d} = 0.05\tilde{r}_1$. (b) $\tilde{d} = 0.10\tilde{r}_1$. (c) $\tilde{d} = 0.15\tilde{r}_1$. (d) $\tilde{d} = 0.20\tilde{r}_1$.

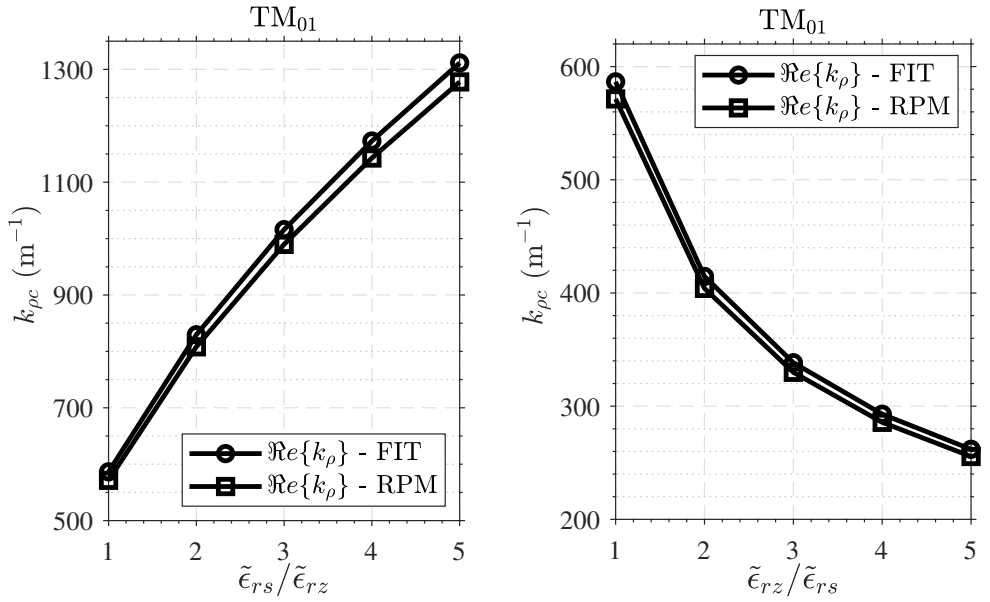

3.5(a): 3.5(b):

Figure 3.5: Cutoff wavenumbers for TM_{01} mode as a function of the anisotropic permittivity ratio: (a) $\tilde{\epsilon}_{rs}/\tilde{\epsilon}_{rz}$, with $\tilde{\epsilon}_{rz} = 1$. (b) $\tilde{\epsilon}_{rz}/\tilde{\epsilon}_{rs}$, with $\tilde{\epsilon}_{rs} = 1$.

Table 3.2: Computational Cost for Case 1

	CPU time	Memory Peak
FIT	15 min, 44.00 s	4401.58 MB
RPM	16.72 s	25.12 MB
CMPM	2.07 s	1.05 MB

Table 3.3: Computational Cost for Case 2

	CPU time	Memory Peak
FIT	22 min, 27.10 s	3791.30 MB
RPM	21.60 s	25.13 MB
CMPM	2.43 s	2.12 MB

3.7
Circular Waveguide Loaded with Eccentric Anisotropic Rods

Consider a circular waveguide bounded by a perfect electric conductor (PEC) of radius $\tilde{r}_1$ and loaded with an inner circular dielectric cylinder of radius $\tilde{r}_0$ offset by a distance $\tilde{d}$ from the longitudinal axis, as shown in Fig. 3.6(a). This is a two-region problem, and distinctions between inner and outer media will be done via the symbols I and II, respectively. The inner rod is an uniaxially anisotropic media defined by the complex-valued permeability and permittivity tensors $\bar{\bar{\tilde{p}}}_{\rm I} = \text{diag}(\tilde{p}_{s,\rm I}, \tilde{p}_{s,\rm I}, \tilde{p}_{z,\rm I})$, with $p = \{\mu, \epsilon\}$, represented in cylindrical coordinates. Similarly, medium II is characterized by $\bar{\bar{\tilde{p}}}_{\rm II} = \text{diag}(\tilde{p}_{s,\rm II}, \tilde{p}_{s,\rm II}, \tilde{p}_{z,\rm II})$. Remembering that we adopt the notation, where the time-harmonics factor $\exp(-i\omega t)$ is assumed and suppressed. As discussed in [47], the problem at hand can be transformed into a two-region *concentric* circular waveguide problem filled with anisotropic and inhomogeneous materials, as depicted in the non-tilted cylindrical coordinates (ρ, ϕ, z) in Fig. 2.1(b). The regions I and II cover the domains $0 \leq \rho < r_0$ and $r_0 < \rho \leq r_1$, respectively. The associated wave equation for the axial electric and magnetic fields can then be solved as a power series for small eccentricities via RPM. According to [47, Eqs. (10)–(11)], the axial field $G = \{E_z, H_z\}$ can be approximated by

$$G = \Big[G_0(\rho,\phi) + \tilde{x}_2^{-1}\, G_1(\rho,\phi) + \tilde{x}_2^{-2}\, G_2(\rho,\phi)\Big] e^{ik_z z}, \tag{3-47}$$

$$k_z^2 = k_{0,z}^2 \Big(1 + \tilde{x}_2^{-1}\, \alpha_1 + \tilde{x}_2^{-2}\, \alpha_2\Big), \tag{3-48}$$

where $\tilde{x}_2^{-1}$ is a small parameter that vanishes as $\tilde{d} \to 0$. $G_0(\rho,\phi)$ and $k_{0,z}$ represent the axial fields and the wavenumber of the zeroth-order problem (i.e., with $\tilde{x}_2^{-1} \to 0$). First- and second-order field corrections are given by $G_1(\rho,\phi)$ and $G_2(\rho,\phi)$, respectively. The factors α_1 and α_2 are first- and second-order corrections to the axial wavenumber. The transverse field components can be expressed as a combinations of the axial ones [28, Ch. 5], [46, Ch. 9], and we can express them as a series in terms of $\tilde{x}_2^{-1}$. For instance, the azimuth component of the electric and magnetic field can be written as

$$G_\phi = \Big[G_{0,\phi}(\rho,\phi) + \tilde{x}_2^{-1}\, G_{1,\phi}(\rho,\phi) + \tilde{x}_2^{-2}\, G_{2,\phi}(\rho,\phi)\Big] e^{ik_z z}, \tag{3-49}$$

where $G_\phi = \{E_\phi, H_\phi\}$ and $G_{j,\phi}(\rho,\phi)$, for $j = \{0,1,2\}$, represents the zeroth-, first-, and second-order RPM contributions, respectively.

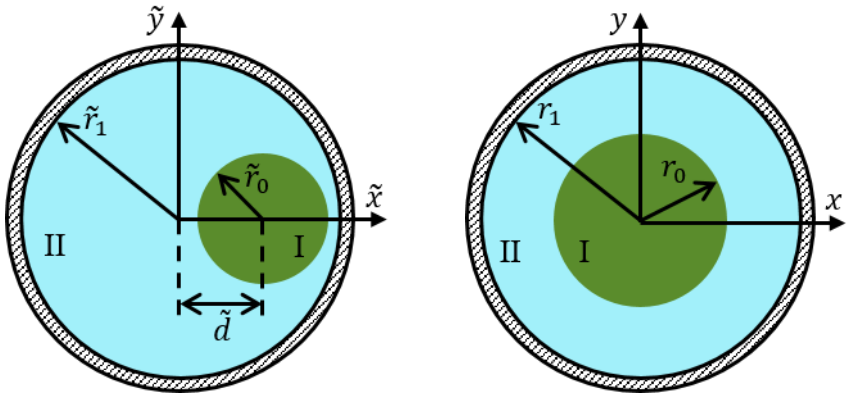

3.6(a): 3.6(b):

Figure 3.6: (a) Geometry of a circular waveguide loaded with an eccentric anisotropic dielectric cylinder in the plane $\tilde{z} = 0$. (b) Transformed waveguide in the plane $z = 0$. Perfect electric conductors are indicated by the stripes.

The zeroth-order field solutions are given by

$$G_0^{\mathrm{I}}(\rho, \phi) = A_{0,\mathrm{I}}^n J_n(\beta_{\mathrm{I}}\rho)\, e^{in\phi}, \tag{3-50a}$$

$$G_0^{\mathrm{II}}(\rho, \phi) = B_n(\beta_{\mathrm{II}}\rho)\, e^{in\phi}, \tag{3-50b}$$

where $B_n(\beta_{\mathrm{II}}\rho) = A_{0,\mathrm{II}}^n J_n(\beta_{\mathrm{II}}\rho) + B_{0,\mathrm{II}}^n H_n(\beta_{\mathrm{II}}\rho)$. J_n and H_n are Bessel and Hankel functions of the first kind and integer order n, $\beta_{\{\mathrm{I,II}\}} = \alpha_{0,\{\mathrm{I,II}\}}\, k_{0,\rho,\{\mathrm{I,II}\}}$ with $k_{0,\rho,\{\mathrm{I,II}\}}^2 = k_{s,\{\mathrm{I,II}\}}^2 - k_{0,z}^2$, $\alpha_{0,\{\mathrm{I,II}\}} = (p_{0,z,\{\mathrm{I,II}\}}/p_{s,\{\mathrm{I,II}\}})^{1/2}$ and $p = \{\mu, \epsilon\}$. See [47] for further details. The coupling of transverse magnetic and electric fields should be considered while solving the problem depicted in Fig. 2.1(b). The coefficients $A_{0,\mathrm{I}}^n$, $A_{0,\mathrm{II}}^n$, and $B_{0,\mathrm{II}}^n$ for E_z and H_z fields comprise six unknowns to be solved on forcing the boundary conditions at $\rho = r_0$ (continuity of tangential fields) and at $\rho = r_1$ (vanishing of the tangential electric field over the PEC boundary in region II), given by,

$$E_z^{\mathrm{I}}(r_0, \phi, z) = E_z^{\mathrm{II}}(r_0, \phi, z), \tag{3-51a}$$

$$E_\phi^{\mathrm{I}}(r_0, \phi, z) = E_\phi^{\mathrm{II}}(r_0, \phi, z), \tag{3-51b}$$

$$H_z^{\mathrm{I}}(r_0, \phi, z) = H_z^{\mathrm{II}}(r_0, \phi, z), \tag{3-51c}$$

$$H_\phi^{\mathrm{I}}(r_0, \phi, z) = H_\phi^{\mathrm{II}}(r_0, \phi, z), \tag{3-51d}$$

$$E_z^{\mathrm{II}}(r_1, \phi, z) = 0, \quad \text{and} \tag{3-51e}$$

$$E_\phi^{\mathrm{II}}(r_1, \phi, z) = 0. \tag{3-51f}$$

A characteristic equation in determinant form is then obtained, and the discrete values of $k_{0,z}$ (and corresponding coefficients $A_{0,\mathrm{I}}^n$, $A_{0,\mathrm{II}}^n$, and $B_{0,\mathrm{II}}^n$ for the axial fields) that contribute to our modal solution can be obtained using

well-known procedures for a two-dielectric problem described in [28, Ch. 5]. In general, the fields are hybrid[1], but under azimuthally-invariant ($n = 0$) conditions, TM and TE fields become decoupled.

Once the zeroth-order field are solved, we can establish the first-order axial fields via section 3.4

$$\begin{aligned} G_1^{\mathrm{I}}(\rho,\phi) &= \Big[A_{1,\mathrm{I}}^{n-1} J_{n-1}(\beta_{\mathrm{I}}\rho) - \frac{\beta_{\mathrm{I}}\rho^2}{2} A_{0,\mathrm{I}}^{n} J_{n+1}(\beta_{\mathrm{I}}\rho)\Big] e^{i(n-1)\phi}, \\ &\quad + \Big[A_{1,\mathrm{I}}^{n+1} J_{n+1}(\beta_{\mathrm{I}}\rho) + \frac{\beta_{\mathrm{I}}\rho^2}{2} A_{0,\mathrm{I}}^{n} J_{n-1}(\beta_{\mathrm{I}}\rho)\Big] e^{i(n+1)\phi}, \qquad (3\text{-}52a) \\ G_1^{\mathrm{II}}(\rho,\phi) &= \Big[B_{n-1}^{1-}(\beta_{\mathrm{II}}\rho) - \frac{\beta_{\mathrm{II}}}{2}\rho^2 B_{n+1}(\beta_{\mathrm{II}}\rho)\Big] e^{i(n-1)\phi} \\ &\quad + \Big[B_{n+1}^{1+}(\beta_{\mathrm{II}}\rho) + \frac{\beta_{\mathrm{II}}}{2}\rho^2 B_{n-1}(\beta_{\mathrm{II}}\rho)\Big] e^{i(n+1)\phi}, \qquad (3\text{-}52b) \end{aligned}$$

where $B_{n\pm1}^{1\pm}(\beta_{\mathrm{II}}\rho) = A_{1,\mathrm{II}}^{n\pm1} J_{n\pm1}(\beta_{\mathrm{II}}\rho) + B_{1,\mathrm{II}}^{n\pm1} H_{n\pm1}(\beta_{\mathrm{II}}\rho)$. The functions in (3-52a) and (3-52b) are used to assemble the E_z and H_z field components in the RPM first-order solution. The boundary conditions at $\rho = r_0$ and $\rho = r_1$ for $e^{i(n-1)\phi}$ terms yield a inhomogeneous 6×6 system of equations for $A_{1,\mathrm{I}}^{n-1}$, $A_{1,\mathrm{II}}^{n-1}$, and $B_{1,\mathrm{II}}^{n-1}$ for E_z and H_z fields (six unknowns). Similarly, the boundary conditions for $e^{i(n+1)\phi}$ terms yield all first-order unknowns. As noted in [47], $\alpha_1 = 0$ and there is no first-order correction in the axial wavenumber because the orthogonality between zeroth- and first-order fields.

Once the zeroth- and first-order fields are determined, the second-order axial fields write as section 3.5

$$\begin{aligned} G_2^{\mathrm{I}}(\rho,\phi) &= \Big[A_{2,\mathrm{I}}^{n} J_n(\beta_{\mathrm{I}}\rho) - \alpha_2 F_{\mathrm{I}}(\beta_{\mathrm{I}}\rho) + P_{\mathrm{I}}(\beta_{\mathrm{I}}\rho)\Big] e^{in\phi} \\ &\quad + \Big[A_{2,\mathrm{I}}^{n-2} J_{n-2}(\beta_{\mathrm{I}}\rho) - \Omega_{\mathrm{I}-}(\beta_{\mathrm{I}}\rho)\Big] e^{i(n-2)\phi} \\ &\quad + \Big[A_{2,\mathrm{I}}^{n+2} J_{n+2}(\beta_{\mathrm{I}}\rho) + \Omega_{\mathrm{I}+}(\beta_{\mathrm{I}}\rho)\Big] e^{i(n+2)\phi}, \qquad (3\text{-}53a) \\ G_2^{\mathrm{II}}(\rho,\phi) &= \Big[B_{n}^{(2)}(\beta_{\mathrm{II}}\rho) - \alpha_2 F_{\mathrm{II}}(\beta_{\mathrm{II}}\rho) + P_{\mathrm{II}}(\beta_{\mathrm{II}}\rho)\Big] e^{in\phi} \\ &\quad + \Big[B_{n-2}^{2-}(\beta_{\mathrm{II}}\rho) - \Omega_{\mathrm{II}-}(\beta_{\mathrm{II}}\rho)\Big] e^{i(n-2)\phi} \\ &\quad + \Big[B_{n+2}^{2+}(\beta_{\mathrm{II}}\rho) + \Omega_{\mathrm{II}+}(\beta_{\mathrm{II}}\rho)\Big] e^{i(n+2)\phi}, \qquad (3\text{-}53b) \end{aligned}$$

[1]In this work, we classify fields as hybrid electric (HE) and hybrid magnetic (EH) according to the definitions in [46, Sec. 9.5]

with

$$B_n^{(2)}(\beta_{\mathrm{II}}\rho) = A_{2,\mathrm{II}}^n J_n(\beta_{\mathrm{II}}\rho) + B_{2,\mathrm{II}}^n H_n(\beta_{\mathrm{II}}\rho), \tag{3-54}$$

$$B_{n\pm2}^{2\pm}(\beta_{\mathrm{II}}\rho) = A_{2,\mathrm{II}}^{n\pm2} J_{n\pm2}(\beta_{\mathrm{II}}\rho) + B_{2,\mathrm{II}}^{n\pm2} H_{n\pm2}(\beta_{\mathrm{II}}\rho), \tag{3-55}$$

$$F_{\mathrm{I}}(\beta_{\mathrm{I}}\rho) = \alpha_0 k_{0,z}^2 \frac{\rho}{2\beta_{\mathrm{I}}} A_{0,\mathrm{I}}^n J_n'(\beta_{\mathrm{I}}\rho), \tag{3-56}$$

$$F_{\mathrm{II}}(\beta_{\mathrm{II}}\rho) = \alpha_0 k_{0,z}^2 \frac{\rho}{2\beta_{\mathrm{II}}} B_n'(\beta_{\mathrm{II}}\rho), \tag{3-57}$$

$$\begin{aligned} P_{\mathrm{I}}(\beta_{\mathrm{I}}\rho) = {} & \frac{\beta_{\mathrm{I}}}{2}\rho^2\Big[A_{1,\mathrm{I}}^{n-1} J_{n-2}(\beta_{\mathrm{I}}\rho) - A_{1,\mathrm{I}}^{n+1} J_{n+2}(\beta_{\mathrm{I}}\rho)\Big] \\ & - \frac{\beta_{\mathrm{I}}^2}{4}\rho^4 A_{0,\mathrm{I}}^n J_n(\beta_{\mathrm{I}}\rho), \end{aligned} \tag{3-58}$$

$$\begin{aligned} P_{\mathrm{II}}(\beta_{\mathrm{II}}\rho) = {} & \frac{\beta_{\mathrm{II}}}{2}\rho^2\Big[B_{n-2}^{1-}(\beta_{\mathrm{II}}\rho) - B_{n+2}^{1+}(\beta_{\mathrm{II}}\rho)\Big] \\ & - \frac{\beta_{\mathrm{II}}^2}{4}\rho^4 B_n(\beta_{\mathrm{II}}\rho), \end{aligned} \tag{3-59}$$

$$\begin{aligned} \Omega_{\mathrm{I}\pm}(\beta_{\mathrm{I}}\rho) = {} & \frac{\beta_{\mathrm{I}}}{2}\rho^2 A_{1,\mathrm{I}}^{n\pm1} J_n(\beta_{\mathrm{I}}\rho) + \frac{\beta_{\mathrm{I}}}{2}\rho^3 A_{0,\mathrm{I}}^n J_{n\mp1}(\beta_{\mathrm{I}}\rho) \\ & + \frac{\beta_{\mathrm{I}}^2}{8}\rho^4 A_{0,\mathrm{I}}^n J_{n\mp2}(\beta_{\mathrm{I}}\rho), \end{aligned} \tag{3-60}$$

$$\begin{aligned} \Omega_{\mathrm{II}\pm}(\beta_{\mathrm{II}}\rho) = {} & \frac{\beta_{\mathrm{II}}}{2}\rho^2 B_n^{1\pm}(\beta_{\mathrm{II}}\rho) + \frac{\beta_{\mathrm{II}}}{2}\rho^3 B_{n\mp1}(\beta_{\mathrm{II}}\rho) \\ & + \frac{\beta_{\mathrm{II}}^2}{8}\rho^4 B_{n\mp2}(\beta_{\mathrm{II}}\rho), \end{aligned} \tag{3-61}$$

where the prime $'$ represents the derivative of the cylindrical functions with respect to their arguments. The functions in (3-53a) and (3-53b) are used to assemble the E_z and H_z field components for the RPM second-order solution. The boundary conditions at $\rho = r_0$ and $\rho = r_1$ for the $e^{im\phi}$ terms with $m = \{n-2, n+2\}$ yield $A_{2,\mathrm{I}}^m$, $A_{2,\mathrm{II}}^m$, and $B_{2,\mathrm{II}}^m$ (six unknowns for each m). For the $e^{in\phi}$ terms, it is required to obtain $A_{2,\mathrm{I}}^n$, $A_{2,\mathrm{II}}^n$, $B_{2,\mathrm{II}}^n$, for E_z and H_z (six unknowns), and α_2. By enforcing the boundary conditions at $\rho = r_0$ and $\rho = r_1$ we can obtain an inhomogeneous system of six equations. In addition, we should enforce the orthogonality of the zero-order fields (denoted compactly as $\mathbf{E}_0$ and $\mathbf{H}_0$) and the second-order ones ($\mathbf{E}_2$ and $\mathbf{H}_2$) over the waveguide cross-section to obtain an additional independent equation. The reaction concept [48], [46, Ch. 7] is used for this purpose, i.e., we impose[2]

$$\int_S \mathbf{E}_0 \times \mathbf{H}_2 \cdot \hat{z}\, \rho\, d\rho\, d\phi = 0, \tag{3-62}$$

where S is the cross-section of the waveguide. The resulting inhomogeneous 7×7 system of equations is then solved to obtain all the unknowns of

[2]It can be shown that the condition in (3-62) is equivalent to that used in [47, Eqs. (47)–(48)] when the zeroth-order TM and TE fields are decoupled.

Table 3.4: Cutoff frequencies f_c (GHz) obtained by FEM [49], zeroth-order RPM, and the method described in [49]. Relative errors are computed assuming the FEM solution as reference.

	FEM [49]	Zeroth-order RPM		Method in [49]	
mode	f_c	f_c	rel. error (%)	f_c	rel. error (%)
HE_{11}	86.861	86.713	0.170	86.953	0.106
HE_{21}	146.100	145.932	0.115	145.925	0.120
HE_{31}	200.574	200.637	0.031	200.772	0.099
TM_{01}	109.105	109.253	0.137	109.301	0.181
EH_{11}	183.011	182.866	0.079	182.834	0.097
EH_{32}	466.844	466.531	0.067	466.465	0.081

the second-order RPM. In Appendix C an additional detailed resolution on obtaining the generic orthogonality condition based on the reaction concept is presented, as well as the expansion of (3-62) considering the zeroth- and second-order fields for the circular anisotropic waveguide filled with eccentric anisotropic dielectric rod.

3.7.1 Numerical Results

We first consider an isotropic circular waveguide with $\tilde{r}_1 = 1$ mm, $\tilde{\epsilon}_{\mathrm{II}} = \epsilon_0$, and $\tilde{\mu}_{\mathrm{II}} = \mu_0$, loaded with an eccentric dielectric rod having $\tilde{r}_0 = 0.1\tilde{r}_1$, $\tilde{d} = 0.03\tilde{r}_1$, $\tilde{\epsilon}_{\mathrm{I}} = 3.6\epsilon_0$, and $\tilde{\mu}_{\mathrm{I}} = \mu_0$, where ϵ_0 and μ_0 are the free-space permittivity and permeability, respectively. This same geometry was considered in [49] and is used here for validation. Table 3.4 shows the cutoff frequencies (f_c, for $k_{0,z} = 0$) obtained by the FEM from [49], the zeroth-order RPM, and the approximate method in [49]. Relative errors are computed using the FEM solution as reference. Good agreement between all results is observed. The zeroth-order RPM provides similar accuracy as [49]. In what follows, we will extrapolate the eccentricity to geometries where the second-order RPM fields become relevant.

Next, consider the same waveguide but with $\tilde{r}_1 = 5$ mm and $\tilde{d} = \{0.03, 0.13, 0.23\}\tilde{r}_1$. Fig. 3.7 shows the axial wavenumbers $k_z = k_z' + ik_z''$ for the dominant modes computed at 25 GHz as a function of $\tilde{d}/\tilde{r}_1$ obtained by (a) the FEM through the CST Studio Suite software [2] and (b) using the zeroth- and second-order RPM. The results show good agreement for small $\tilde{d}/\tilde{r}_1$. The zeroth-order RPM diverges as the eccentricity distance increases, as expected, but the second-order RPM provides good approximations in all

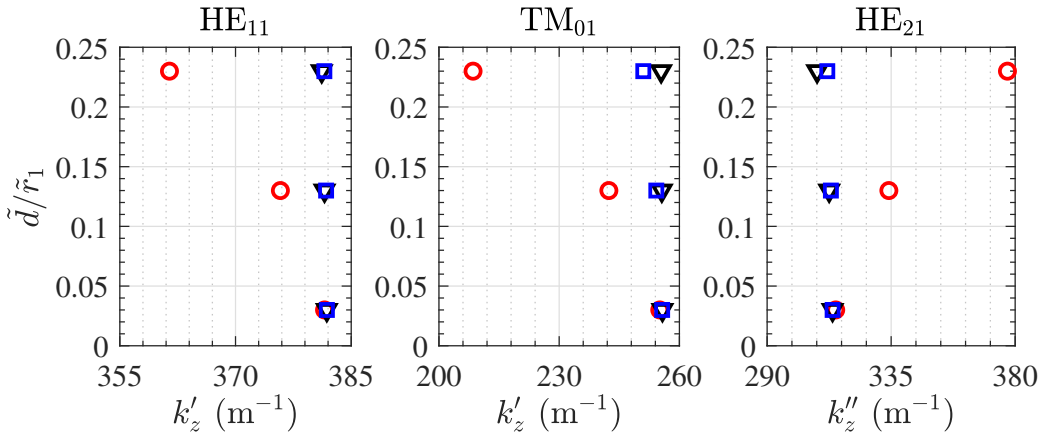

Figure 3.7: Axial wavenumbers $k_z = k'_z + ik''_z$ for the dominant modes as a function of the normalized eccentricity distance $\tilde{d}/\tilde{r}_1$ obtained by FEM (□), zeroth-order RPM (○), and second-order RPM (▽).

tested scenarios. For example, in the worst case, the TM_{01} mode shows a relative error of only 1.78% when $\tilde{d}/\tilde{r}_1 = 23\%$. Fig. 3.8 shows the normalized axial electric field patterns for the TM_{01} mode obtained when $\tilde{d}/\tilde{r}_1 = 23\%$. Good agreement is observed versus FEM results.

Finally, we consider a similar geometry as before, with $\tilde{d} = 0.23\tilde{r}_1$ but now we have different anisotropy combinations for media I and II. Fig. 3.9 we consider two scenarios for each graphic (a) and (b): Fig.(a) we consider that region II is isotropic (vacuum) and the region I is a non-magnetic material with permittivity given by $\bar{\bar{\epsilon}}_{\rm I} = \epsilon_0\,\mathrm{diag}(\tilde{\epsilon}_{rs,\rm I}, \tilde{\epsilon}_{rs,\rm I}, \tilde{\epsilon}_{rz,\rm I})$, in the first case for HE_{11} mode we varying $\tilde{\epsilon}_{rs,\rm I}$ from 1.6 to 5.6 for a fixed $\tilde{\epsilon}_{rz,\rm I} = 3.6$, and second case for TM_{01} mode we interchange the values of $\tilde{\epsilon}_{rz,\rm I}$ and $\tilde{\epsilon}_{rs,\rm I}$. In Fig. 3.9(b) we apply the same procedure, but we add to medium I a magnetic permeability described by $\bar{\bar{\mu}}_{\rm I} = \mu_0\,\mathrm{diag}(5.6, 5.6, 1.6)$ and we also consider that medium II is completely anisotropic characterized by $\bar{\bar{\mu}}_{\rm II} = \mu_0\,\mathrm{diag}(1.6, 1.6, 5.6)$ e $\bar{\bar{\epsilon}}_{\rm II} = \epsilon_0\,\mathrm{diag}(1.6, 1.6, 5.6)$, The second-order RPM result show again good agreement with FIT results from [2] with average error of 0.11% and 0.10% for HE_{11} and TM_{01} modes, respectively. Fig. 3.10 shows normalized axial electric field patterns for the TM_{01} mode obtained for case when $\tilde{\epsilon}_{rz,\rm I} = 5.6$. Good agreement is observed versus FIT results.

As a benchmark for the RPM computational cost, the CPU time required to calculate the first 15 modes for the waveguide of case B with $\tilde{\epsilon}_{rz,\rm I} = 5.6$ was 0.98 s in our Matlab code. In contrast, FIT results took 912 s to solve the same problem using the standard options of CST [2] with a 2D grid of 301×301 meshcells. All the results were obtained using an HP Z800 Workstation with a dual quad-core 2.40-GHz Intel Xeon E5620 processor.

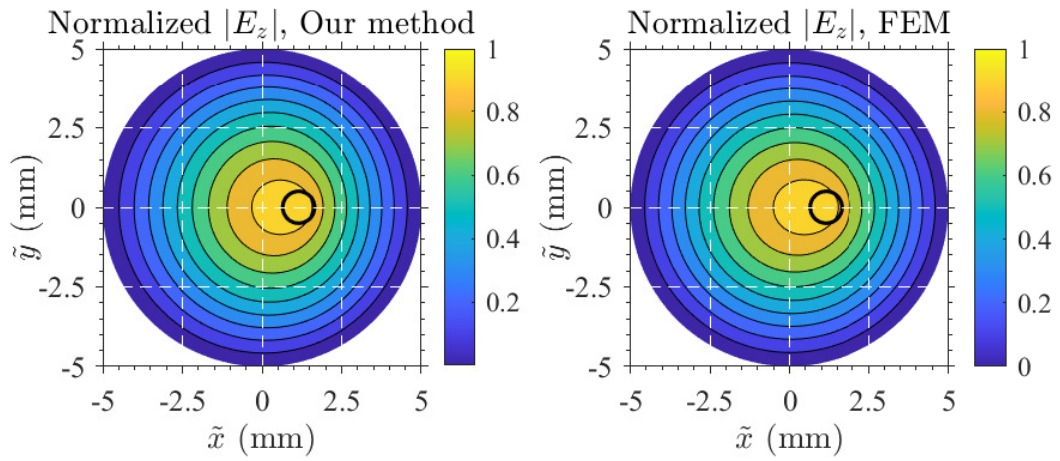

Figure 3.8: Normalized axial electric field TM_{01} mode patterns calculated using RPM (left) and FEM [2] (right). Circle with a bold line delimits the inner rod, i.e., region I.

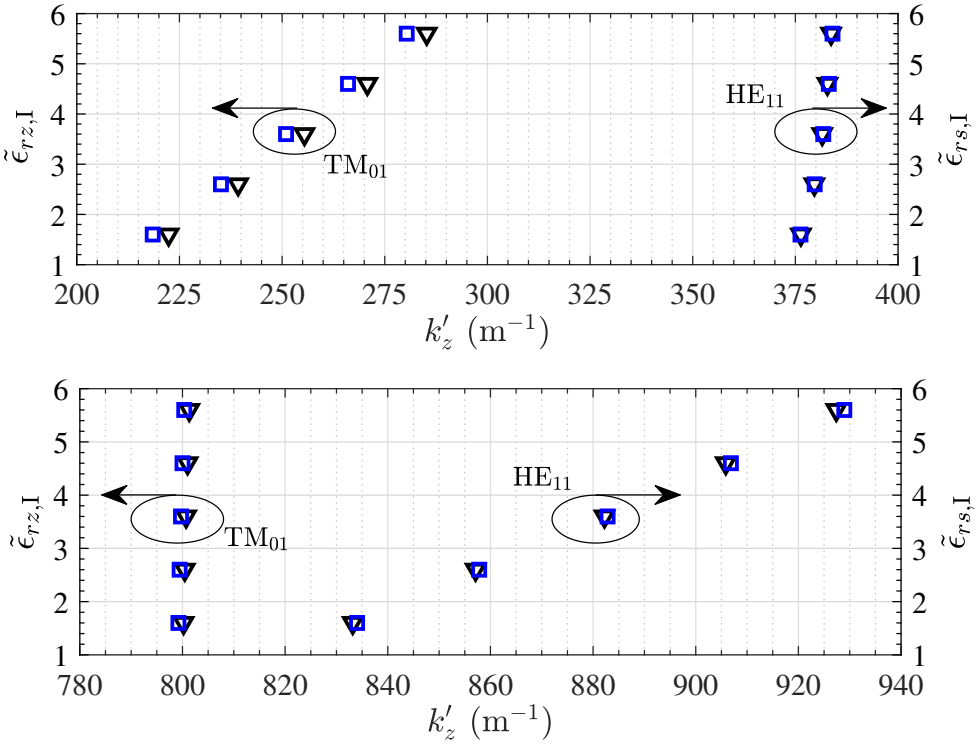

Figure 3.9: Axial wavenumbers of HE_{11} mode with $\tilde{\epsilon}_{rz,\mathrm{I}} = 3.6$ fixed and TM_{01} mode with $\tilde{\epsilon}_{rs,\mathrm{I}} = 3.6$ fixed. In upper graphic the region II is isotropic material and for lower graphic we consider full anisotropic material with $\tilde{\mu}_{rz,\mathrm{I}\backslash\mathrm{II}} = 1.6\backslash 5.6$, $\tilde{\mu}_{rs,\mathrm{I}\backslash\mathrm{II}} = 5.6\backslash 1.6$ and $\tilde{\epsilon}_{rz,\mathrm{II}} = 5.6$ and $\tilde{\epsilon}_{rz,\mathrm{II}} = 1.6$ obtained by FIT ($\square$) and by second-order RPM ($\triangledown$).

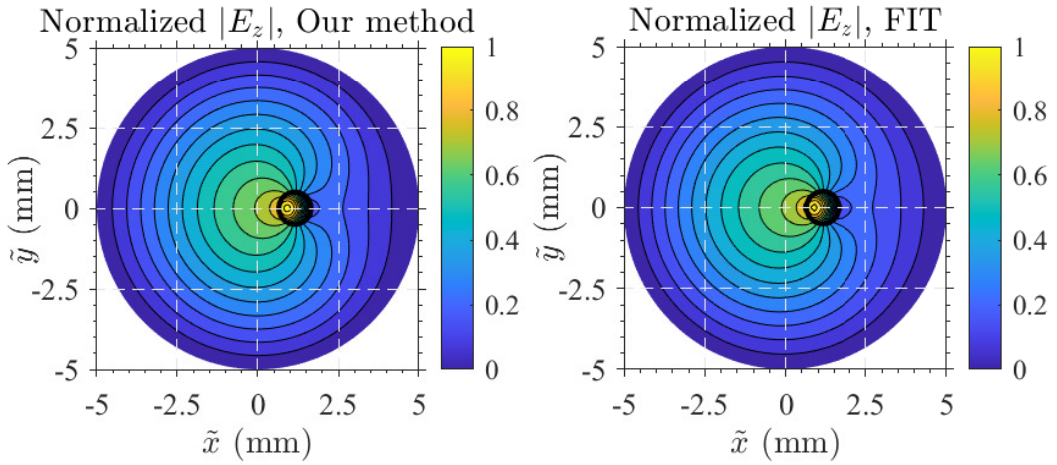

Figure 3.10: Normalized axial electric field for TM_{01} mode calculated using RPM (left) and FIT (right). Circle with a bold line delimits the inner rod.

4
Cavity-Material Perturbation Method

4.1
Introduction

In this chapter, we present an extended version of the Harrington's cavity-material perturbation method (CMPM) [28, Ch. 7] for accounting the longitudinal wavenumber of lossy inhomogenous and anisotropic waveguides. To the best of our knowledge, similar solutions are available in the literature, but are restricted for lossless cavities [50, pp. 472–475] (i.e., perturbation formulas for correcting the resonance frequency) and lossless waveguides [51, Sec. 7.3.1]. We have employed our CMPM formula for modeling anisotropic coaxial waveguides with small eccentricities. In addition, we introduce a combined RPM and CMPM formulation for providing high-order corrections in a simplified way.

4.2
Mathematical Formulation

As an alternative way to account for the effects of the inhomogeneous media presented the concentric coaxial waveguide shown in Fig. 2.1(b), we may consider the change in the propagating constant of a homogeneous-filled waveguide as due to a material perturbation. The fields in the waveguide filled with a homogeneous and uniaxially anisotropic medium described by the constitutive tensor

$$\bar{\bar{p}}_0 = \begin{bmatrix} p_s & 0 & 0 \\ 0 & p_s & 0 \\ 0 & 0 & p_{0,z} \end{bmatrix} \text{ with } p = \{\mu, \epsilon\} \tag{4-1}$$

were already described in Section 3.3. In view of (2-32), by writing $\bar{\bar{p}} = \bar{\bar{p}}_0 + \Delta\bar{\bar{p}}$, the media is then perturbed by the inhomogeneous tensor

$$\Delta\bar{\bar{p}} = \begin{bmatrix} 0 & 0 & 0 \\ 0 & 0 & 0 \\ 0 & 0 & \Delta p_z \end{bmatrix}, \tag{4-2}$$

where

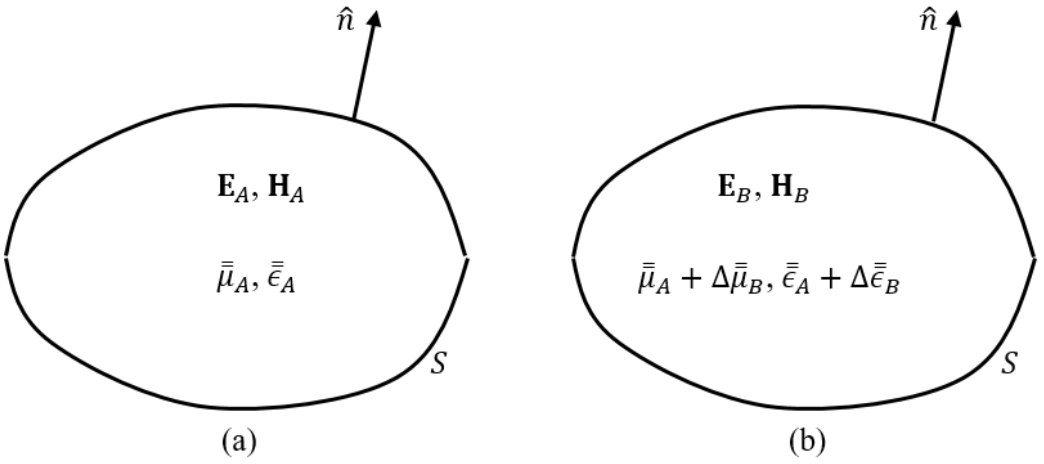

Figure 4.1: Perturbation of matter in a cavity. (a) Original cavity; (b) perturbed cavity.

$$\Delta p_z = p_{0,z}\left[\frac{4\rho}{\tilde{x}_2}\cos(\phi) + \frac{2\rho^2}{\tilde{x}_2^2}\left(3\cos(2\phi)+2\right) + \mathcal{O}(\tilde{x}_2^{-3})\right]. \tag{4-3}$$

Assume the two cavities shown in Fig. 4.1, both operating at the angular frequency ω. In Fig. 4.1(a) we have a cavity filled with a material characterized by the permeability and permittivity tensors $\bar{\bar{\mu}}_A$, and $\bar{\bar{\epsilon}}_A$, respectively, and with the electromagnetic fields $\mathbf{E}_A$, and $\mathbf{H}_A$. In the second case, shown in Fig. 4.1(b), we have the same cavity but now the matter is described by $\bar{\bar{\mu}}_A + \Delta\bar{\bar{\mu}}_B$ and $\bar{\bar{\epsilon}}_A + \Delta\bar{\bar{\epsilon}}_B$, and here the fields are denoted as $\mathbf{E}_B$ and $\mathbf{H}_B$. The Maxwell's curls equation in source-free regions can written as follows:

$$\boldsymbol{\nabla}\times\mathbf{E}_A = i\omega\bar{\bar{\mu}}_A\cdot\mathbf{H}_A, \tag{4-4a}$$
$$\boldsymbol{\nabla}\times\mathbf{H}_A = -i\omega\bar{\bar{\epsilon}}_A\cdot\mathbf{E}_A, \tag{4-4b}$$
$$\boldsymbol{\nabla}\times\mathbf{E}_B = i\omega\left(\bar{\bar{\mu}}_A + \Delta\bar{\bar{\mu}}_B\right)\cdot\mathbf{H}_B, \tag{4-4c}$$
$$\boldsymbol{\nabla}\times\mathbf{H}_B = -i\omega\left(\bar{\bar{\epsilon}}_A + \Delta\bar{\bar{\epsilon}}_B\right)\cdot\mathbf{E}_B, \tag{4-4d}$$

On dot multiplying $\mathbf{H}_B$ by (4-4a), and $\mathbf{E}_A$ by (4-4d), we obtain

$$\mathbf{H}_B\cdot\boldsymbol{\nabla}\times\mathbf{E}_A = i\omega\mathbf{H}_B\cdot\bar{\bar{\mu}}_A\cdot\mathbf{H}_A, \tag{4-5a}$$
$$\mathbf{E}_A\cdot\boldsymbol{\nabla}\times\mathbf{H}_B = -i\omega\mathbf{E}_A\cdot\left(\bar{\bar{\epsilon}}_A + \Delta\bar{\bar{\epsilon}}_B\right)\cdot\mathbf{E}_B. \tag{4-5b}$$

The sum of the preceding two equations gives

$$\boldsymbol{\nabla}\cdot(\mathbf{E}_A\times\mathbf{H}_B) = i\omega\mathbf{H}_B\cdot\bar{\bar{\mu}}_A\cdot\mathbf{H}_A + i\omega\mathbf{E}_A\cdot\left(\bar{\bar{\epsilon}}_A + \Delta\bar{\bar{\epsilon}}_B\right)\cdot\mathbf{E}_B, \tag{4-6}$$

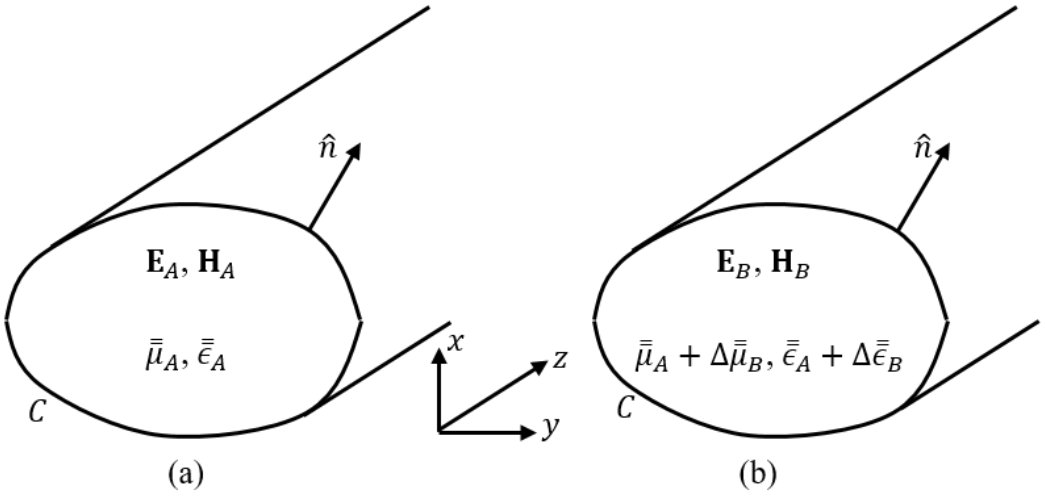

Figure 4.2: Perturbation of the matter in a cylindrical waveguide. (a) Original waveguide; (b) perturbed waveguide.

where combining the identity

$$\boldsymbol{\nabla} \cdot (\mathbf{A} \times \mathbf{B}) = \mathbf{B} \cdot \boldsymbol{\nabla} \times \mathbf{A} - \mathbf{A} \cdot \boldsymbol{\nabla} \times \mathbf{B}, \tag{4-7}$$

was employed. An analogous procedure using (4-4b) and (4-4c) allows us to obtain

$$\boldsymbol{\nabla} \cdot (\mathbf{E}_B \times \mathbf{H}_A) = i\omega \mathbf{E}_B \cdot \bar{\bar{\epsilon}}_A \cdot \mathbf{E}_A + i\omega \mathbf{H}_A \cdot \left(\bar{\bar{\mu}}_A + \Delta\bar{\bar{\mu}}_B\right) \cdot \mathbf{H}_B. \tag{4-8}$$

Subtracting (4-6) from (4-8), integrating the result in volume V, and the subsequent application of the divergence theorem allows the following result:

$$\oint_S (\mathbf{E}_A \times \mathbf{H}_B - \mathbf{E}_B \times \mathbf{H}_A) \cdot d\mathbf{S} = i\omega \int_V \left(\mathbf{E}_A \cdot \Delta\bar{\bar{\epsilon}}_B \cdot \mathbf{E}_B - \mathbf{H}_A \cdot \Delta\bar{\bar{\mu}}_B \cdot \mathbf{H}_B\right) dV. \tag{4-9}$$

Now, let us consider a perturbation problem in a waveguide instead of in a cavity. Fig. 4.2(a) shows a waveguide positioned along the z-axis. The matter of this anisotropic-filled waveguide was perturbed, and we assume this perturbation is independent of z, as depicted in the geometry in Fig. 4.2. We can assume $\mathbf{E}_0^+$ and $\mathbf{H}_0^+$ are the electric and magnetic fields traveling in the direction of $z > 0$ associated with the axial wavenumber $k_{0,z}$ in the unperturbed medium (described by the tensors $\bar{\bar{\mu}}_A$ and $\bar{\bar{\epsilon}}_A$). Accordingly, let $\mathbf{E}^-$, $\mathbf{H}^-$ and k_z be the electric and magnetic fields and the axial wavenumber for fields propagating in the direction of $z < 0$, associated with the perturbed medium (described by the tensors $\bar{\bar{\mu}}_A + \Delta\bar{\bar{\mu}}_B$ and $\bar{\bar{\epsilon}}_A + \Delta\bar{\bar{\epsilon}}_B$). In with of the theory in

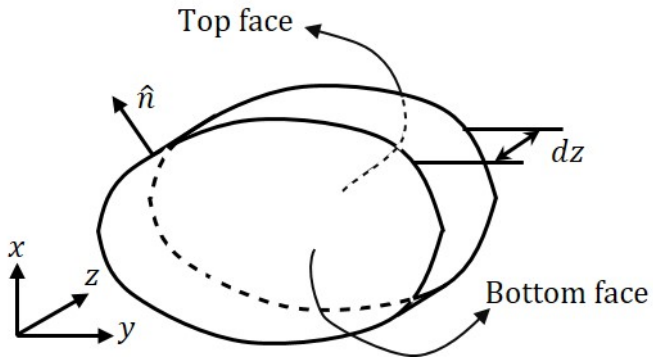

Figure 4.3: Differential slice of a cylinder with a constant cross-section.

Chapter 2, we can write

$$\begin{aligned} \mathbf{E}_A &= \mathbf{E}_0^+ \, e^{+ik_{0,z}z} \\ \mathbf{H}_A &= \mathbf{H}_0^+ \, e^{+ik_{0,z}z} \end{aligned} \quad \text{and} \quad \begin{aligned} \mathbf{E}_B &= \mathbf{E}^- e^{-ik_z z} \\ \mathbf{H}_B &= \mathbf{H}^- e^{-ik_z z}, \end{aligned} \tag{4-10}$$

where the subscript 0 refers to *unperturbed* quantities.

We can explore some useful results from (4-9) by considering that our waveguide volume can be reduced to a slice of thickness dz, as shown in Fig. 4.3. Since the lateral walls of the waveguide are truncated by a perfect electrical conductive (PEC), and assuming the unperturbed fields satisfy the boundary conditions, we have $\mathbf{E}_B \times \mathbf{H}_A \cdot \hat{z} = \mathbf{H}_A \cdot (\hat{z} \times \mathbf{E}_B) = 0$ and $\mathbf{E}_A \times \mathbf{H}_B \cdot \hat{z} = \mathbf{H}_B \cdot (\hat{z} \times \mathbf{E}_A) = 0$. Accordingly, some parts of the surface integral in (4-9) vanish, and the remaining non-null contributions are over the top and bottom cross-section areas of the slice. Furthermore, since the thickness of the slice was taken a differential distance, we can symbolic write the surface integral of (4-9) as

$$\int_{S_{\text{top}}} + \int_{S_{\text{bottom}}} = \lim_{dz\to 0} dz \, \frac{\partial}{\partial z} \int_S = -i \, (k_z - k_{0,z}) \lim_{dz\to 0} dz \int_S . \tag{4-11}$$

Then, (4-9) can alternatively written as

$$\begin{aligned} -i \, (k_z - k_{0,z}) \lim_{dz\to 0} dz \int_S (\mathbf{E}_A \times \mathbf{H}_B - \mathbf{E}_B \times \mathbf{H}_A) \cdot \hat{z} \, dS \\ = i\omega \int_V \left(\mathbf{E}_A \cdot \Delta\bar{\bar{\epsilon}}_B \cdot \mathbf{E}_B - \mathbf{H}_A \cdot \Delta\bar{\bar{\mu}}_B \cdot \mathbf{H}_B \right) dV. \end{aligned} \tag{4-12}$$

Notice from the above that the volume integral of the slice can be a reduce to

$\int_V \to dz \int_S$ in the limit $dz \to 0$, and hence reducing (4-12) to

$$-i\,(k_z - k_{0,z}) \int_S (\mathbf{E}_A \times \mathbf{H}_B - \mathbf{E}_B \times \mathbf{H}_A) \cdot \hat{z}\, dS \\ = i\omega \int_S \left(\mathbf{E}_A \cdot \Delta\bar{\bar{\epsilon}}_B \cdot \mathbf{E}_B - \mathbf{H}_A \cdot \Delta\bar{\bar{\mu}}_B \cdot \mathbf{H}_B \right) dS, \quad (4\text{-}13)$$

or, alternatively,

$$\frac{k_{0,z} - k_z}{\omega} = \frac{\int_S \left(\mathbf{E}_A \cdot \Delta\bar{\bar{\epsilon}}_B \cdot \mathbf{E}_B - \mathbf{H}_A \cdot \Delta\bar{\bar{\mu}}_B \cdot \mathbf{H}_B \right) dS}{\int_S (\mathbf{E}_A \times \mathbf{H}_B - \mathbf{E}_B \times \mathbf{H}_A) \cdot \hat{z}\, dS}. \quad (4\text{-}14)$$

The result above is an extended version of Harrington's cavity-material perturbation method (CMPM) [28, Ch. 7] for accounting the longitudinal wavenumber of lossy inhomogenous and anisotropic waveguides.

By replacing the fields in (4-10) and the medium tensors in (4-2) into (4-14), we can obtain [52]

$$\frac{k_{0,z} - k_z}{\omega} = \frac{\int_S \left(\Delta\bar{\bar{\epsilon}} \cdot \mathbf{E}^- \cdot \mathbf{E}_0^+ + \Delta\bar{\bar{\mu}} \cdot \mathbf{H}^- \cdot \mathbf{H}_0^+ \right) dS}{\int_S \left(\mathbf{E}_0^+ \times \mathbf{H}^- + \mathbf{E}^- \times \mathbf{H}_0^+ \right) \cdot \hat{z}\, dS}. \quad (4\text{-}15)$$

The result in (4-15) is exact, but not practical because the fields in the perturbed problem are unknowns. At this point, we can consider the medium and the fields coming from the optical transformation. First, by assuming the perturbation does not significantly modify the field patterns as long as the eccentricity $\tilde{d}$ is small (or $\tilde{x}_2$ is large), we can approximate $\mathbf{E}^-$ and $\mathbf{H}^-$ by its analogous non-perturbed versions, i.e., the fields associated with the npth (cylindrical) harmonic are

$$\begin{aligned} \mathbf{E}_0^+ &= \mathbf{e}_{np}(\rho)\, e^{in\phi} \\ \mathbf{H}_0^+ &= \mathbf{h}_{np}(\rho)\, e^{in\phi} \end{aligned} \quad \text{and} \quad \begin{aligned} \mathbf{E}^- &= \mathbf{e}_{-np}(\rho)\, e^{-in\phi} \\ \mathbf{H}^- &= -\mathbf{h}_{-np}(\rho)\, e^{-in\phi}. \end{aligned} \quad (4\text{-}16)$$

Please see [27] for further details. Also, the axial wavenumber can be expanded as

$$k_z \approx k_{0,z} \left(1 + \frac{\alpha_1}{2\tilde{x}_2} + \frac{\alpha_2}{2\tilde{x}_2^2} + \mathcal{O}(\tilde{x}_2^{-3}) \right), \quad (4\text{-}17)$$

where $k_{0,z}$ is the axial wavenumber of the zeroth-order solution, and α_1 and α_2 are the correction factors of first- and second-order, respectively.

Next, by substituting (4-16) and (4-2) into the numerator in the right-

hand side of (4-15), we obtain, after some simplifications,

$$\int_S \Delta\bar{\bar{\epsilon}} \cdot \mathbf{E}^- \cdot \mathbf{E}_0^+ \, dS = \frac{8\pi\epsilon_{0,z}}{\tilde{x}_2^2} \int_{r_0}^{r_1} e_{z,-np}(\rho)\, e_{z,np}(\rho)\ \rho^3 \, d\rho, \tag{4-18}$$

$$\int_S \Delta\bar{\bar{\mu}} \cdot \mathbf{H}^- \cdot \mathbf{H}_0^+ \, dS = -\frac{8\pi\mu_{0,z}}{\tilde{x}_2^2} \int_{r_0}^{r_1} h_{z,-np}(\rho)\, h_{z,np}(\rho)\, \rho^3 \, d\rho, \tag{4-19}$$

where we have retaining correction terms up to $\tilde{x}_2^{-2}$. Notice that the above equations do not have terms of order $\tilde{x}_2^{-1}$. As a consequence, there is no first-order correction in (4-17), i.e., $\alpha_1 = 0$. This is the same result obtained in Section 3.4 for the RPM.

By substituting equations (4-17), (4-18) and (4-19) in (4-15), we obtain

$$\alpha_2 = -\frac{\omega}{k_{0,z}} \frac{16\pi}{N_{np}} \left(I_{\mathrm{TM}} + I_{\mathrm{TE}}\right), \tag{4-20}$$

where

$$N_{np} = \int_S \left(\mathbf{E}_0^+ \times \mathbf{H}^- + \mathbf{E}^- \times \mathbf{H}_0^+\right) \cdot \hat{z} \, dS, \tag{4-21}$$

$$I_{\mathrm{TM}} = \epsilon_{0,z} \int_{r_0}^{r_1} e_{z,-np}(\rho)\, e_{z,np}(\rho)\, \rho^3 \, d\rho, \tag{4-22}$$

$$I_{\mathrm{TE}} = -\mu_{0,z} \int_{r_0}^{r_1} h_{z,-np}(\rho)\, h_{z,np}(\rho)\, \rho^3 \, d\rho. \tag{4-23}$$

From the above, we observe that TM_{np} and TE_{np} fields are decoupled. As a final note, the above solution indicates that $\alpha_2 = 0$ for a TEM field since (4-18) and (4-19) become zero for $k_\rho \to 0$ and $n = 0$.

By considering that $e_{z,-np}(\rho) = (-1)^n e_{z,np}(\rho)$ we can reduce the (4-22) to

$$\begin{aligned} I_{\mathrm{TM}} &= \epsilon_{0,z}(-1)^n \int_{r_0}^{r_1} e_{z,np}(\rho)^2\, \rho^3 \, d\rho \\ &= \epsilon_{0,z}(-1)^n \left[\frac{\rho^4}{6(\beta\rho)^3} d_{\mathrm{TM}} B_n(\beta\rho)^2\right]\Bigg|_{\rho=r_0}^{r1}, \end{aligned} \tag{4-24}$$

where

$$d_{\mathrm{TM}} = (\beta\rho)^3 + 2(n^2 - 1)\beta\rho. \tag{4-25}$$

Please see Appendix B for further details about the derivation of d_{TM}.

Similarly, from (4-23) we can obtain

$$I_{\mathrm{TE}} = -\mu_{0,z}(-1)^n \int_{r_0}^{r_1} h_{z,np}(\rho)^2\, \rho^3\, d\rho$$
$$= -\mu_{0,z}(-1)^n \left[\frac{\rho^4}{6(\beta\rho)^3} d_{\mathrm{TE}} B_n'(\beta\rho)^2 \right] \Bigg|_{\rho=r_0}^{r1}, \tag{4-26}$$

where

$$d_{\mathrm{TE}} = \frac{1}{\beta\rho}\Big[(\beta\rho)^4 + (\beta\rho)^2 n^2 - 2n^2(n-1)\Big]. \tag{4-27}$$

Please see Appendix B for further details about the derivation of d_{TE}. Finally, notice that N_{np} also admits closed-form solutions [27].

4.3 Improved Cavity-Material Perturbation Method

In this section, the perturbation method described in Chapters 3 is combined with the above described perturbation method to determine the cutoff wavenumber of the modes in the eccentric coaxial waveguide. We use the low-order corrections from a regular perturbation method (RPM) into the Harrington's cavity-material perturbation method (CMPM) for providing high-order corrections to the cutoff wavenumbers of TM and TE modes supported in a coaxial waveguides. The proposed methodology allows a perturbation solution that is more simple and more computationally efficient than the RPM approach, whereas more accurate than the ordinary CMPM.

In summary, a conformal transformation optics is used to map the original (eccentric) problem shown in Fig. 2.1(a) into a concentric waveguide shown in Fig. 2.1(b). Then, we solve the resulting wave equation in the transformed (concentric) domain. The RPM is established and the field solutions are obtained as a power series with respect to the eccentricity parameter. We then solve three second-order differential equations to compute the zeroth-, first-, and second-order corrections for TM and TE modes of coaxial waveguides with small eccentricities. Further details are available in Section 3.4.

The mapped waveguide in Fig. 2.1(b) has its medium characterized by the anisotropic and inhomogeneous electrical permittivity and magnetic permeability tensors $\bar{\bar{\epsilon}} = \bar{\bar{\epsilon}}_0 + \Delta\bar{\bar{\epsilon}}$, and $\bar{\bar{\mu}} = \bar{\bar{\mu}}_0 + \Delta\bar{\bar{\mu}}$, respectively, and described by (4-2).

The axial wavenumber can be expanded as

$$k_z \approx k_{0,z}\left(1 + \frac{\alpha_1}{2\tilde{x}_2} + \frac{\alpha_2}{2\tilde{x}_2^2} + \frac{\alpha_3}{2\tilde{x}_2^3} + \frac{\alpha_4}{2\tilde{x}_2^4} + \mathcal{O}(\tilde{x}_2^{-5})\right), \tag{4-28}$$

where $k_{0,z}$ is the axial wave number of the zero-order solution and $\alpha_{1,2,3,4}$ are the first-, second-, third-, and fourth-order correction factors, respectively.

The RPM solution (up to first-order correction) can be written in a compact form as

$$\mathbf{F}^{\pm} = \mathbf{F}^{\pm}_{0,np} + \frac{\mathbf{F}^{\pm}_{1,(n+1)p}}{\tilde{x}_2} + \frac{\mathbf{F}^{\pm}_{1,(n-1)p}}{\tilde{x}_2}, \quad \text{with} \quad \mathbf{F} = \{\mathbf{E}, \mathbf{H}\}, \tag{4-29}$$

where the subscript $(0, np)$ is related to the zeroth-order fields and the terms with index $(n\pm1)p$ are associated with the first-order perturbation corrections.

Based on CMPM presented before, the change in the axial wavenumber due to the perturbation $\Delta\bar{\bar{\epsilon}}$ and $\Delta\bar{\bar{\mu}}$ is given by

$$\frac{k_{0,z} - k_z}{\omega} = \frac{\int_S \left(\Delta\bar{\bar{\epsilon}} \cdot \mathbf{E}^- \cdot \mathbf{E}_0^+ + \Delta\bar{\bar{\mu}} \cdot \mathbf{H}^- \cdot \mathbf{H}_0^+\right) dS}{\int_S \left(\mathbf{E}_0^+ \times \mathbf{H}^- + \mathbf{E}^- \times \mathbf{H}_0^+\right) \cdot \hat{z}\, dS} \tag{4-30}$$

$$= \frac{I_{\mathrm{TM}} + I_{\mathrm{TE}}}{N_{np}}. \tag{4-31}$$

By replacing (4-3) and (4-10) in (4-30), after some simplifications, we can obtain

$$I_{\mathrm{TM}} = \frac{8\pi\epsilon_{0,z}}{\tilde{x}_2^2} \int_{r_0}^{r_1} \left[\rho e_{z,np}^2 + e_{z,np}\left(e_{z,(n+1)p} + e_{z,(n-1)p}\right)\right] \rho^2\, d\rho + \frac{2\pi\epsilon_{0,z}}{\tilde{x}_2^4} \int_{r_0}^{r_1} \left[8 e_{z,(n+1)p} e_{z,(n-1)p} + 3\left(e_{z,(n+1)p}^2 + e_{z,(n-1)p}^2\right)\right] \rho^3\, d\rho, \tag{4-32}$$

$$I_{\mathrm{TE}} = \frac{8\pi\mu_{0,z}}{\tilde{x}_2^2} \int_{r_0}^{r_1} \left[\rho h_{z,np}^2 + h_{z,np}\left(h_{z,(n+1)p} + h_{z,(n-1)p}\right)\right] \rho^2\, d\rho + \frac{2\pi\mu_{0,z}}{\tilde{x}_2^4} \int_{r_0}^{r_1} \left[8 h_{z,(n+1)p} h_{z,(n-1)p} + 3\left(h_{z,(n+1)p}^2 + h_{z,(n-1)p}^2\right)\right] \rho^3\, d\rho, \tag{4-33}$$

and

$$
\begin{aligned}
N_{np} &= \int_S \left(\mathbf{E}^+ \times \mathbf{H}^- - \mathbf{E}^- \times \mathbf{H}^+\right) \cdot \hat{z}\, dS \\
&= \int_{r_0}^{r_1} \Bigg[\mathbf{E}^+_{0,np} \times \mathbf{H}^-_{0,-np} - \mathbf{E}^-_{0,-np} \times \mathbf{H}^+_{0,np} \\
&\qquad + \frac{1}{\tilde{x}_2^2}\Big(\mathbf{E}^+_{(n+1)p} \times \mathbf{H}^-_{(-n-1)p} + \mathbf{E}^+_{(n-1)p} \times \mathbf{H}^-_{(-n+1)p} \\
&\qquad\qquad - \mathbf{E}^-_{(-n+1)p} \times \mathbf{H}^+_{(n-1)p} - \mathbf{E}^-_{(-n-1)p} \times \mathbf{H}^+_{(n+1)p}\Big)\Bigg] \cdot \hat{z}\, \rho\, d\rho \\
&= (-1)^n 4\pi \int_{r_0}^{r_1} \Bigg[e^{0+}_{\phi,np} h^{0+}_{\rho,np} + e^{0+}_{\rho,np} h^{0+}_{\phi,np} \\
&\qquad + \frac{1}{\tilde{x}_2^2}\Big(e^+_{\phi,(n+1)p} h^+_{\rho,(n+1)p} + e^+_{\rho,(n+1)p} h^+_{\phi,(n+1)p} \\
&\qquad\qquad + e^+_{\phi,(n-1)p} h^+_{\rho,(n-1)p} + e^+_{\rho,(n-1)p} h^+_{\phi,(n-1)p}\Big)\Bigg] \rho\, d\rho,
\end{aligned}
\tag{4-34}
$$

for $n \geq 0$ in all equations. The equations above do not present terms with $\tilde{x}_2^{-1}$ and $\tilde{x}_2^{-3}$ as a consequence of the azimuth orthogonality in the numerator in (4-30). In other words, the correction factors α_1 and α_3 in (4-28) vanish. If the first-order fields are zero, the above equations reduce to the ordinary CMPM presented in [52]. In what follows, the present method will be referred to as improved CMPM (ICMPM).

4.4 Results

To validate the CMPM and ICMPM methods, we consider an eccentric coaxial waveguide with $\tilde{r}_1 = 5$ mm, $\tilde{r}_0 = 0.05\tilde{r}_1$ and eccentricity $\tilde{d} = 0.05\tilde{r}_1$, assuming the medium as vacuum. Table 4.1 shows the cutoff wavenumbers $k_{\rho c} = (\omega^2\mu_s\epsilon_s - k_z^2)^{1/2}$ for the first TE_{np} and TM_{np} modes. The results obtained by the ICMPM show good agreement with those obtained by (a) the finite-element method (FEM) from CST Studio Suited [2], (b) the ordinary Harrington's cavity-material perturbation method (CMPM), and (c) the regular perturbation method (RPM). Relative errors were computed using the FEM solution as a reference. As expected, we can observe that the ICMPM results have a relative error of less than 0.2%, while the CMPM presented an error of up to 0.6%.

In Fig. 4.4 we explore more scenarios, where we keep the same waveguide considered before, but with different values of eccentricity in order to

Table 4.1: Cutoff wavenumbers obtained by the FEM from [2], results from RPM, from CMPM, and from ICMPM. The relative errors were computed using the FEM solution as reference.

	FEM	ICMPM		RPM		CMPM	
Mode	$k_{\rho c}(\mathrm{m}^{-1})$	$k_{\rho c}(\mathrm{m}^{-1})$	Error(%)	$k_{\rho c}(\mathrm{m}^{-1})$	Error(%)	$k_{\rho c}(\mathrm{m}^{-1})$	Error(%)
TE_{11}	366.156	366.874	0.196	366.230	0.020	367.789	0.446
TE_{21}	610.692	610.954	0.043	610.796	0.017	611.333	0.105
TE_{31}	840.159	841.705	0.184	840.234	0.009	843.861	0.441
TM_{01}	610.692	611.126	0.071	610.674	-0.003	614.109	0.559
TM_{11}	775.540	774.706	-0.107	775.698	0.020	774.695	-0.109
TM_{21}	1027.331	1028.426	0.106	1027.383	0.005	1028.743	0.137

investigate the capacity of these methods. With FEM as a reference, we notice that all the tested perturbational methods gradually deteriorate as the eccentricity factor increases. Also, we notice that the ICMPM performs better than the CMPM in all the analyzed scenarios. The RPM outperforms the CMPM in all cases, and the ICMPM except for the TM_{01} mode. Although the computational resources demanded by the RPM are higher compared to the other perturbation methods, the ICMPM can capture more appropriately the characteristics of the TM_{01} mode. This is a consequence of the limited azimuth variations the RPM [52] can provide.

The merits of the ICMPM are also evidenced in Fig. 4.5, which shows the TM_{01} cutoff wavenumbers as a function of the anisotropic permittivity ratio. We have assumed a waveguide filled with an anisotropic medium described by $\tilde{\mu}_s = \tilde{\mu}_z = \mu_0$ and $\tilde{\epsilon}_s = \epsilon_0\tilde{\epsilon}_{rs}$, $\tilde{\epsilon}_z = \epsilon_0\tilde{\epsilon}_{rz}$ (where ϵ_0 and μ_0 are the vacuum parameters) and with an eccentricity $\tilde{d} = 0.2\tilde{r}_1$. As before, we see that the ICMPM outperforms the RPM when assuming the finite-integration technique (FIT) results as a reference.

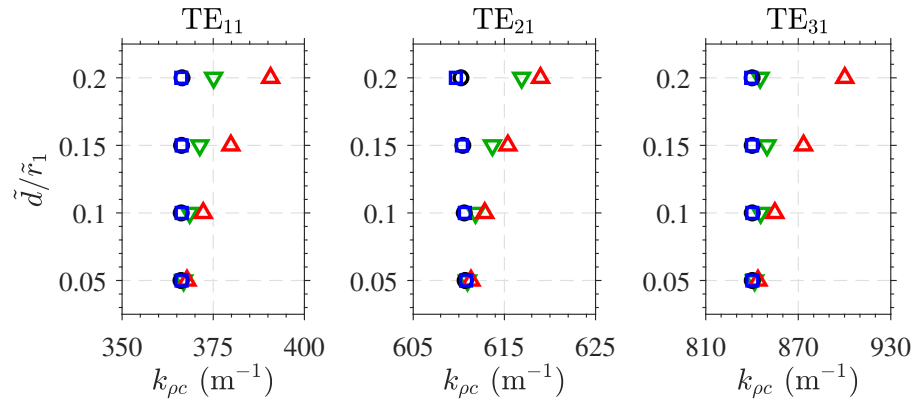

4.4(a):

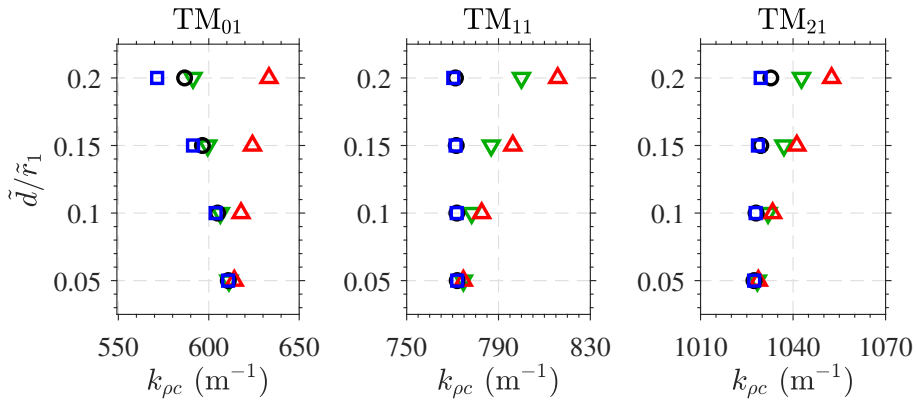

4.4(b):

Figure 4.4: Cutoff wavenumbers for (a) TE and (b) TM modes as a function of the normalized eccentricity distance $\tilde{d}/\tilde{r}_1$ obtained by FEM (○), by RPM from (□), by CMPM from (△), and by the presented ICMPM (▽).

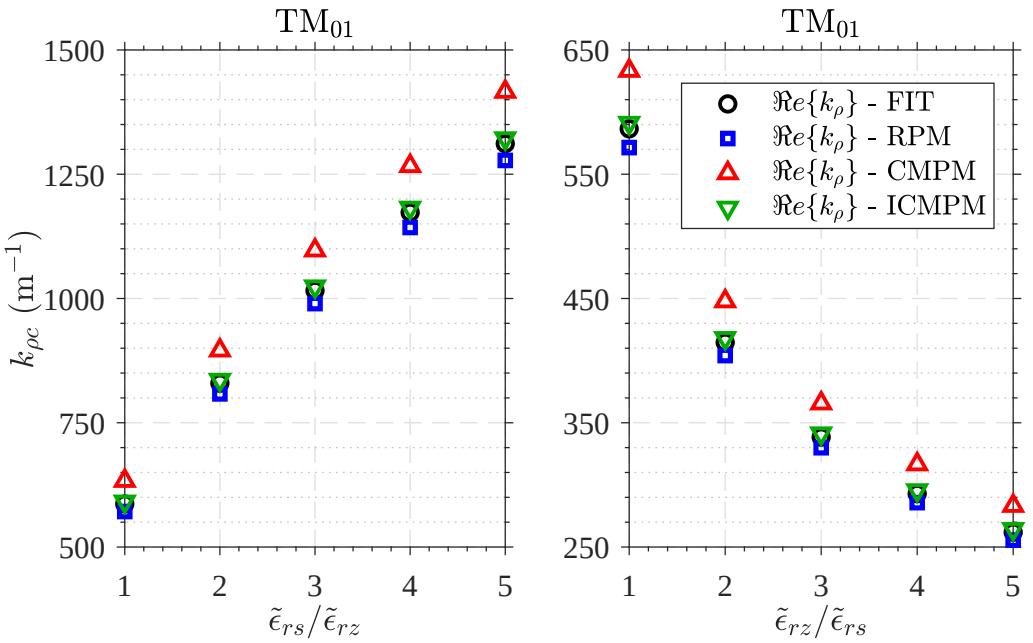

Figure 4.5: Cutoff wavenumbers for the TM_{01} mode as a function of the anisotropic permittivity ratio. The results in (a) are for a fixed $\tilde{\epsilon}_{rz} = 1$, while the results in (b) are for a fixed $\tilde{\epsilon}_{rs} = 1$.

5
Point-Matching Method

5.1
Introduction

In this chapter, the so-called point-matching method (PMM) will be formulated and discussed. In short, this method allows us to find an approximated solution for two-dimensional Helmholtz equation subject to complex-shaped boundary conditions by expanding the field solutions as a series of cylindrical harmonics. The boundary conditions are then enforced at an appropriate set of points over the domain boundaries. This method is also referred in the literature as straightforward point-matching method (SPMM), and was developed in the seminal works [9, 17, 18]. This method has been used with success over the years for the analysis of non-circular hollow waveguides [9,17,18], scattering by dielectric cylinders [19–21], and other waveguided-devices [22,23]. However, it is important to stress this method may fail when the cross-section of the waveguide has a convex geometry from an external point of view. Another deficiency this method can present in some complex geometries is the ill-conditioning (linear dependence) in the associated system of equations that can happen in some particular scenarios. This problem usually is alleviated by a careful selection of points where the boundary conditions are enforced.

Another extension of the SPMM is obtained by using the addition theorem for Bessel functions [53, Ch. 11]. This approach allows us to replicate the SPMM in different coordinate systems, so that the chosen contour has different points and is exactly the points of the geometry. In other words, we can describe the geometry of the waveguide as a combination of circles. A similar method was used in [54] for a scattering problem.

In this chapter, we explore point-matching-based methods for solving complex anisotropic-filled non-circular multi-layered cylindrical guided structures. An improved PPM formulation based on the recent works in [19, 22] is also investigated for allowing us to obtain more degrees of freedom on choosing the matching points and in the truncation of the azimuthal series used in the solution. Furthermore, a source expansion in terms of cylindrical harmonics is introduced on the grounds of the Lorentz reciprocity Theorem.

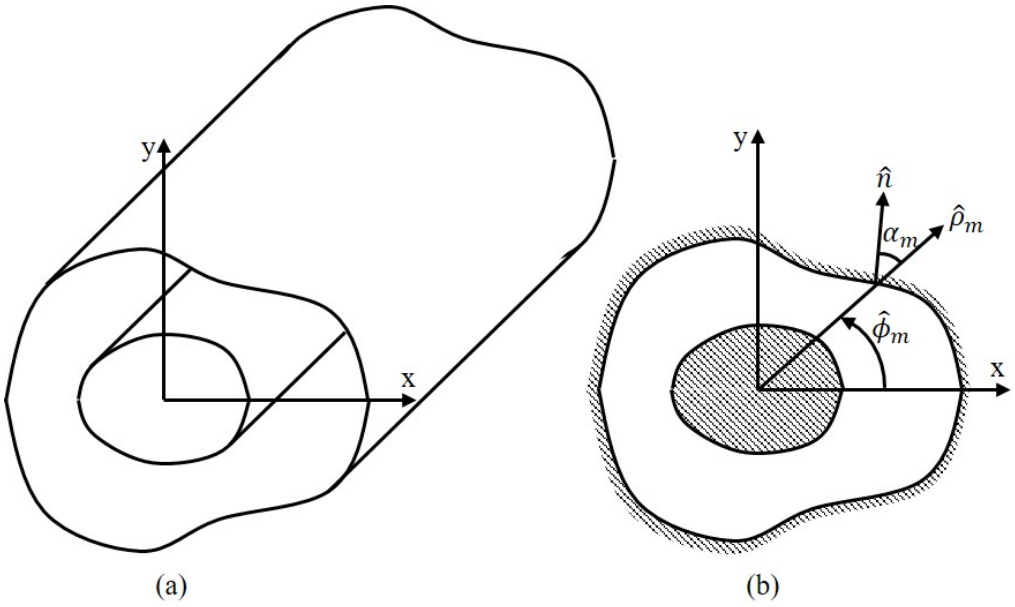

Figure 5.1: Coaxial waveguide with arbitrary cross-section.

5.2 Straightforward Point-Matching Method for Hollow Waveguides

We consider here a waveguide with an inner perfect electric conductor (PEC) enclosed by an outer PEC cylinder. This waveguide has an arbitrary cross-section (with an exception for convex contours) that is invariant along the z-axis, as depicted in the geometry in Fig. 5.1. The axial (to z) fields should satisfy the Helmholtz equation in cylindrical coordinates

$$\left(\nabla_s^2 + \beta^2\right) G(\rho, \phi, z) = 0, \tag{5-1}$$

where $G = \{E_z, H_z\}$. We consider the waveguide is filled with an anisotropic medium, defined by $\bar{\bar{p}} = \text{diag}(p_s, p_s, p_z)$ with $p = \{\mu, \epsilon\}$. The radial wavemumber satisfy $\beta^2 = \alpha^2 k_\rho^2$, with $\alpha = (p_z/p_s)^{1/2}$ being the anisotropy factor defined in Chapter 2. Also, we have $k_\rho^2 = k_s^2 - k_z^2$, $k_s^2 = \omega^2 \mu_s \epsilon_s$, where k_z is the axial wavenumber.

The solution for G can be written as [17] and [55, Ch. 10]

$$G(\rho, \phi, z) = \sum_{n=-N}^{+N} \left[A^n H_n^{(1)}(\beta\rho) + B^n J_n(\beta\rho)\right] e^{in\phi + ik_z z}. \tag{5-2}$$

Alternatively, if the cross-section is symmetrical with respect to the x-axis, we

can write

$$G_e(\rho,\phi,z) = \sum_{n=0}^{N-1} \left[A_e^n H_n^{(1)}(\beta\rho) + B_e^n J_n(\beta\rho)\right] \cos(n\phi) e^{ik_z z}, \tag{5-3}$$

$$G_o(\rho,\phi,z) = \sum_{n=1}^{N} \left[A_o^n H_n^{(1)}(\beta\rho) + B_o^n J_n(\beta\rho)\right] \sin(n\phi) e^{ik_z z}, \tag{5-4}$$

where J_n and $H_n^{(1)}$ are first kind Bessel and Hankel functions, respectively, with integer order n. The set of unknown constants A^n and B^n are to be determined by the boundary conditions enforcement. The subscripts e and o are used in (5-3) and (5-4) to represent *even* and *odd* modes, respectively, with respect to the x-axis. Since the representation of E_z and H_z are now defined as a series of cylindrical harmonics, the transversal fields can be determined using (2-24) and (2-25).

5.2.1 TM modes

For solving the transversal magnetic (TM) fields, we have $G = E_z$, and a Dirichlet boundary condition must be satisfied on the outer and inner PEC that truncate the waveguide under analysis. However, satisfying this condition is not a simple task since the contour that delimits these conductors is now arbitrary. The point-matching method allows us to find an approximate solution by matching the boundary conditions over a set of m points described in polar coordinates by (ρ_m, ϕ_m). On enforcing

$$\sum_n \left[A^n H_n(\beta\rho_m) + B^n J_n(\beta\rho_m)\right] \begin{matrix}\cos\\ \sin\end{matrix}(n\phi_m) = 0, \tag{5-5}$$

over a set of $N+1$ points per boundary, we obtain a homogeneous linear system equations that allows us to solve the coefficients A^n and B^n. Also, we obtain a determinant characteristic equation for the eigenvalues β.

5.2.2 TE modes

For solving the transversal electric (TE) fields, we have $G = H_z$, and a Neumann boundary condition $\partial H_z/\partial n|_{\text{PEC}} = 0$ must be satisfied on the inner and outer PEC that truncate the waveguide under analysis, where n is the normal direction in respect to waveguide contour (see Fig. 5.1). Since $\partial/\partial n = \hat{n} \cdot \nabla_s$ (where $\hat{n}$ is an outward normal vector), from (2-24), we need

to enforce

$$\sum_n \Big\{ (\hat{n}\cdot\hat{\rho}_m)\beta\rho_m \Big[A^n H_n'(\beta\rho_m) + B^n J_n'(\beta\rho_m)\Big]\begin{matrix}\cos\\ \sin\end{matrix}(n\phi_m) \\ \mp (\hat{n}\cdot\hat{\phi}_m) n \Big[A^n H_n(\beta\rho_m) + B^n J_n(\beta\rho_m)\Big]\begin{matrix}\sin\\ \cos\end{matrix}(n\phi_m)\Big\} = 0, \tag{5-6}$$

over a set of $N+1$ points per each conductor shown in Fig. 5.1. By defining the angle α_m, and the unit vectors $\hat{\rho}_m$ and $\hat{\phi}_m$ according to the geometry in Fig. 5.1, we can simplify (5-6) by means of $\hat{n}\cdot\hat{\rho}_m = \cos\alpha_m$ and $\hat{n}\cdot\hat{\phi}_m = \sin\alpha_m$.

5.3 Improved Point-Matching Method

The SPMM can be improved by matching the fields at the boundary contours via a projection solution with a set of orthogonal basis functions [19, 22], similar to the procedure used in the method of moments [13]. This approach is commonly known as field matching, and will be used here to obtain more degrees of freedom on choosing points in the contours of the waveguide because it mitigates linear dependency problems that happen in the ordinary SPMM. As a drawback, a path integral is now required and it will impair the computational cost of the method.

Consider the orthogonal set of functions w_p, for $p = 0, ..., N$, given by

$$w_p(c) = \frac{1}{\sqrt{C}}\exp\Big(\frac{i2\pi p}{C}c\Big), \tag{5-7}$$

where C is the total length of the boundary and c measures the contour length. This basis function is simpler and more convenient than the basis function set used if we were to use the Galerkin method because our characteristic equations are composed of pairs of cylindrical functions, for example, $H_n^{(1)}(\beta\rho_m) + J_n(\beta\rho_m)$. In what follow, we will employ the inner product

$$\Big\langle g_n(c)\,,\, w_p(c)\Big\rangle = \int_0^C g_n(c)\, w_p(c)^*\, dc. \tag{5-8}$$

It is important to mention that we can recover the SPMM approach using Dirac's delta functions in w_p as follows

$$w_m(\rho,\phi) = \delta(\rho-\rho_m)\frac{\delta(\phi-\phi_m)}{\rho}, \tag{5-9}$$

where the index p (azimuthal order) was replaced by m (m^{th} point on the boundary) to clarify the understanding of the methods. In this way, the inner

product is reduced to

$$\Big\langle g_n(\rho,\phi)\,,\, w_m(\rho,\phi)\Big\rangle = g_n(\rho_m,\phi_m). \tag{5-10}$$

Notice that g_n can assume the form of (5-5) and (5-6) functions, used in SPMM to solve the problem of TM and TE modes, respectively. The above-described approach will be denoted here as the improved point-matching method (IPMM) just for the facility of notation.

5.3.1 TM mode

The IPMM solutions for TM modes is given by the projections of the boundary condition (5-5) with w_p, in view of (5-8), along the over the inner and outer waveguide contours denoted he as c_1 and c_2. As a result, we obtain

$$\begin{bmatrix} W^H_{np}(c_1) & W^J_{np}(c_1) \\ W^H_{np}(c_2) & W^J_{np}(c_2) \end{bmatrix} \begin{bmatrix} A^e_n \\ B^e_n \end{bmatrix} = \bar{0}, \tag{5-11}$$

where

$$W^F_{np}(c) = \Big\langle F_n(\beta\rho(c))\overset{\cos}{\underset{\sin}{}}(n\phi(c))\,,\, w_p(c)\Big\rangle, \tag{5-12}$$

with $F_n = \{J_n, H^{(1)}_n\}$ are first kind Bessel and Hankel functions of integer order n.

5.3.2 TE mode

The IPMM for TE modes is given by projecting (5-6) with w_p, in view of (5-8). As a results, we obtain

$$\begin{bmatrix} W^H_{np}(c_1) & W^J_{np}(c_1) \\ W^H_{np}(c_2) & W^J_{np}(c_2) \end{bmatrix} \begin{bmatrix} A^h_n \\ B^h_n \end{bmatrix} = \bar{0}, \tag{5-13}$$

where

$$\begin{aligned} W^F_{np}(c) = \Big\langle \Big[\, \beta\rho(c)F'_n(\beta\rho(c))\cos(\alpha(c))\overset{\cos}{\underset{\sin}{}}(n\phi(c)) \\ \mp nF_n(\beta\rho(c))\sin(\alpha(c))\overset{\sin}{\underset{\cos}{}}(n\phi(c))\,\Big]\,,\, w_p(c)\Big\rangle. \end{aligned} \tag{5-14}$$

5.4 Point-Matching Methods for Layered Waveguides

Considering a coaxial waveguide filled with two radial layers, as depicted in Fig. 5.2. Layers 1 and 2 are connected at the interface $\rho = r_l$, for $0 < \phi < 2\pi$. Whereas the cross-section of this waveguide has a symmetry with respect to the x-axis, we have

$$G^1_{\substack{e\\o}}(\rho,\phi,z) = \sum_n \Big[A^n_1 H^{(1)}_n(\beta_1\rho) + B^n_1 J_n(\beta_1\rho)\Big]^{\cos}_{\sin}(n\phi)e^{ik_z z}, \tag{5-15}$$

$$G^2_{\substack{e\\o}}(\rho,\phi,z) = \sum_n \Big[A^n_2 H^{(1)}_n(\beta_2\rho) + B^n_2 J_n(\beta_2\rho)\Big]^{\cos}_{\sin}(n\phi)e^{ik_z z}, \tag{5-16}$$

where $G = \{H_z, E_z\}$ in layers 1 and 2. The boundary conditions to be enforced are given by:

$$E^1_{z^e_o}(\rho = r_0,\phi,z) = 0, \tag{5-17a}$$
$$E^1_{t^e_o}(\rho = r_0,\phi,z) = 0, \tag{5-17b}$$
$$E^2_{z^e_o}(\rho = r_1,\phi,z) = 0, \tag{5-17c}$$
$$E^2_{t^e_o}(\rho = r_1,\phi,z) = 0, \tag{5-17d}$$
$$E^1_{z^e_o}(\rho = r_l,\phi,z) = E^2_{z^e_o}(\rho = r_l,\phi,z), \tag{5-17e}$$
$$E^1_{t^e_o}(\rho = r_l,\phi,z) = E^2_{t^e_o}(\rho = r_l,\phi,z), \tag{5-17f}$$
$$H^1_{z^e_o}(\rho = r_l,\phi,z) = H^2_{z^e_o}(\rho = r_l,\phi,z), \tag{5-17g}$$
$$H^1_{t^e_o}(\rho = r_l,\phi,z) = H^2_{t^e_o}(\rho = r_l,\phi,z). \tag{5-17h}$$

Equation (5-17a) requires

$$E^1_{z^e_o}(r_0,\phi_0,z) = \Big[A^n_{1e} H^{(1)}_n(\beta^e_1 r_{0m}) + B^n_{1e} J_n(\beta^e_1 r_{0m})\Big]^{\cos}_{\sin}(n\phi_{0m}) = 0. \tag{5-18}$$

Equation (5-17b) requires

$$E^1_{t^e_o}(r_0,\phi_0,z) = (\hat{n}\cdot\hat{r}_{0m})\beta^h_1 r_{0m}\Big[A^n_{1h} H'_n(\beta^h_1 r_{0m}) + B^n_{1h} J'_n(\beta^h_1 r_{0m})\Big]^{\cos}_{\sin}(n\phi_{0m})$$
$$\mp(\hat{n}\cdot\hat{\phi}_{0m})n\Big[A^n_{1h} H_n(\beta^h_1 r_{0m}) + B^n_{1h} J_n(\beta^h_1 r_{0m})\Big]^{\sin}_{\cos}(n\phi_{0m}) = 0. \tag{5-19}$$

Equation (5-17c) requires

$$E^2_{z^e_o}(r_1,\phi_1,z) = \Big[A^n_{2e}H^{(1)}_n(\beta^e_2 r_{1m}) + B^n_{2e}J_n(\beta^e_2 r_{1m})\Big]^{\cos}_{\sin}(n\phi_{1m}) = 0. \tag{5-20}$$

Equation (5-17d) requires

$$E^2_{t^e_o}(r_1,\phi_1,z) = (\hat{n}\cdot\hat{r}_{1m})\beta^h_2 r_{1m}\Big[A^n_{2h}H'_n(\beta^h_2 r_{1m}) + B^n_{2h}J'_n(\beta^h_2 r_{1m})\Big]^{\cos}_{\sin}(n\phi_{1m})$$
$$\mp(\hat{n}\cdot\hat{\phi}_{1m})n\Big[A^n_{2h}H_n(\beta^h_2 r_{1m}) + B^n_{2h}J_n(\beta^h_2 r_{1m})\Big]^{\sin}_{\cos}(n\phi_{1m}) = 0. \tag{5-21}$$

Equation (5-17e) requires

$$\Big[A^n_{1e}H^{(1)}_n(\beta^e_1 r_{lm}) + B^n_{1e}J_n(\beta^e_1 r_{lm})\Big]^{\cos}_{\sin}(n\phi_{lm}) =$$
$$\Big[A^n_{2e}H^{(1)}_n(\beta^e_2 r_{lm}) + B^n_{2e}J_n(\beta^e_2 r_{lm})\Big]^{\cos}_{\sin}(n\phi_{lm}). \tag{5-22}$$

Equation (5-17h) requires

$$\Big[A^n_{1h}H^{(1)}_n(\beta^h_1 r_{lm}) + B^n_{1h}J_n(\beta^h_1 r_{lm})\Big]^{\cos}_{\sin}(n\phi_{lm}) =$$
$$\Big[A^n_{2h}H^{(1)}_n(\beta^h_2 r_{lm}) + B^n_{2h}J_n(\beta^h_2 r_{lm})\Big]^{\cos}_{\sin}(n\phi_{lm}). \tag{5-23}$$

Equation (5-17f) requires

$$\Big[P^e_{H,1}A^n_{1e} + P^e_{J,1}B^n_{1e} + F^h_{H,1}A^n_{1h} + F^h_{J,1}B^n_{1h} =$$
$$P^e_{H,2}A^n_{2e} + P^e_{J,2}B^n_{2e} + F^h_{H,2}A^n_{2h} + F^h_{J,2}B^n_{2h}\Big]_{\rho_{lm},\phi_{lm}}, \tag{5-24}$$

where

$$P^e_{G,j} = \frac{ik_z}{k^2_{\rho j}}\Big[\sin\alpha_{lm}\beta^e_j G'_n\,{}^{\cos}_{\sin}(n\phi_{lm}) \pm \cos\alpha_{lm}\frac{n}{r_{lm}}G_n\,{}^{\sin}_{\cos}(n\phi_{lm})\Big], \tag{5-25}$$

$$F^h_{G,j} = \frac{i\omega\mu_s}{k^2_{\rho j}}\Big[\mp\sin\alpha_{lm}\frac{n}{r_{lm}}G_n\,{}^{\sin}_{\cos}(n\phi_{lm}) + \cos\alpha_{lm}\beta^h_j G'_n\,{}^{\cos}_{\sin}(n\phi_{lm})\Big]. \tag{5-26}$$

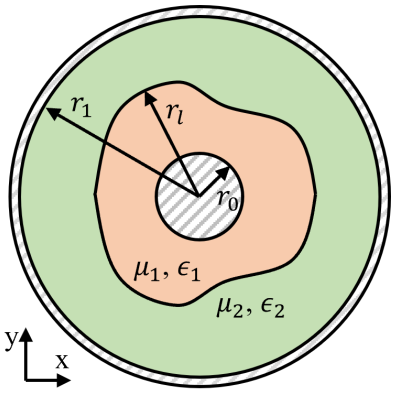

Figure 5.2: Coaxial waveguide filled with two non-circular layers.

Notice we have omitted the arguments of Bessel functions for simplifying the notation. Equation (5-17h) requires

$$\Big[P^h_{H,1}A^n_{1h} + P^h_{J,1}B^n_{1h} + F^e_{H,1}A^n_{1e} + F^e_{J,1}B^n_{1e} = P^h_{H,2}A^n_{2h} + P^h_{J,2}B^n_{2h} + F^e_{H,2}A^n_{2e} + F^e_{J,2}B^n_{2e}\Big]_{\rho_{lm},\phi_{lm}}, \quad (5\text{-}27)$$

where P^h and F^e are similar the expressions in (5-25) and (5-26) but switching $e \to h$ and $h \to e$.

We can combine the above boundary conditions into a matrix:

$$\begin{array}{rl}
E^1_z|_{\rho=r_{0m}} = 0 & : \\
E^1_t|_{\rho=r_{0m}} = 0 & : \\
[E^1_z = E^2_z]_{\rho=r_{lm}} & : \\
[E^1_t = E^2_t]_{\rho=r_{lm}} & : \\
[H^1_z = H^2_z]_{\rho=r_{lm}} & : \\
[H^1_t = H^2_t]_{\rho=r_{lm}} & : \\
E^2_z|_{\rho=r_{1m}} = 0 & : \\
E^2_t|_{\rho=r_{lm}} = 0 & :
\end{array}
\begin{bmatrix}
H^e_{1,n} & J^e_{1,n} & 0 & 0 & 0 & 0 & 0 & 0 \\
0 & 0 & Q^h_{H,1} & Q^h_{J,1} & 0 & 0 & 0 & 0 \\
H^e_{1,n} & J^e_{1,n} & 0 & 0 & -H^e_{2,n} & -J^e_{2,n} & 0 & 0 \\
P^e_{H,1} & P^e_{J,1} & F^h_{H,1} & F^h_{J,1} & -P^e_{H,2} & -P^e_{J,2} & -F^h_{H,2} & -F^h_{J,2} \\
0 & 0 & H^h_{1,n} & J^h_{1,n} & 0 & 0 & -H^h_{2,n} & -J^h_{2,n} \\
F^e_{H,1} & F^e_{J,1} & P^h_{H,1} & P^h_{J,1} & -F^e_{H,2} & -F^e_{J,2} & -P^h_{H,2} & -P^h_{J,2} \\
0 & 0 & 0 & 0 & H^e_{2,n} & J^e_{2,n} & 0 & 0 \\
0 & 0 & 0 & 0 & 0 & 0 & Q^h_{H,2} & Q^h_{J,2}
\end{bmatrix}
\begin{bmatrix}
A^n_{1e} \\ B^n_{1e} \\ A^n_{1h} \\ B^n_{1h} \\ A^n_{2e} \\ B^n_{2e} \\ A^n_{2h} \\ B^n_{2h}
\end{bmatrix}
= \bar{0}$$

$$\big[\bar{\bar{M}}_{m,n}\big]\big[\bar{A}_n\big] = \bar{0}, \quad (5\text{-}28)$$

where

$$H_{1,n}^{e} = H_n(\beta_1^e r_{0m}) \begin{matrix}\cos\\ \sin\end{matrix} (n\phi_{0m}), \tag{5-29a}$$

$$J_{1,n}^{e} = J_n(\beta_1^e r_{0m}) \begin{matrix}\cos\\ \sin\end{matrix} (n\phi_{0m}), \tag{5-29b}$$

$$Q_{H,1}^{h} = \cos\alpha_{0m}\beta_1^h r_{0m} H_n'(\beta_1^h r_{0m}) \begin{matrix}\cos\\ \sin\end{matrix} (n\phi_{0m}) \mp \sin\alpha_{0m} n H_n(\beta_1^h r_{0m}) \begin{matrix}\sin\\ \cos\end{matrix} (n\phi_{0m}), \tag{5-29c}$$

$$Q_{J,1}^{h} = \cos\alpha_{0m}\beta_1^h r_{0m} J_n'(\beta_1^h r_{0m}) \begin{matrix}\cos\\ \sin\end{matrix} (n\phi_{0m}) \mp \sin\alpha_{0m} n J_n(\beta_1^h r_{0m}) \begin{matrix}\sin\\ \cos\end{matrix} (n\phi_{0m}), \tag{5-29d}$$

$$H_{2,n}^{e} = H_n(\beta_2^e r_{1m}) \begin{matrix}\cos\\ \sin\end{matrix} (n\phi_{1m}), \tag{5-29e}$$

$$J_{2,n}^{e} = J_n(\beta_2^e r_{1m}) \begin{matrix}\cos\\ \sin\end{matrix} (n\phi_{1m}), \tag{5-29f}$$

$$Q_{H,2}^{h} = \cos\alpha_{1m}\beta_2^h r_{1m} H_n'(\beta_2^h r_{1m}) \begin{matrix}\cos\\ \sin\end{matrix} (n\phi_{1m}) \mp \sin\alpha_{1m} n H_n(\beta_2^h r_{1m}) \begin{matrix}\sin\\ \cos\end{matrix} (n\phi_{1m}), \tag{5-29g}$$

$$Q_{J,2}^{h} = \cos\alpha_{1m}\beta_2^h r_{1m} J_n'(\beta_2^h r_{1m}) \begin{matrix}\cos\\ \sin\end{matrix} (n\phi_{1m}) \mp \sin\alpha_{1m} n J_n(\beta_2^h r_{1m}) \begin{matrix}\sin\\ \cos\end{matrix} (n\phi_{1m}). \tag{5-29h}$$

The matrix $\bar{\bar{M}}_{m,n}$ is a submatrix of the characteristic equation of the PMM. Futhermore, when we consider all points used in the problem boundary to obtain a full matrix of system equation writen by

$$\begin{bmatrix} \bar{\bar{M}}_{1,1} & \cdots & \bar{\bar{M}}_{1,n} & \cdots & \bar{\bar{M}}_{1,N} \\ \vdots & \ddots & & & \vdots \\ \bar{\bar{M}}_{m,1} & & \bar{\bar{M}}_{m,n} & & \bar{\bar{M}}_{m,N} \\ \vdots & & & \ddots & \vdots \\ \bar{\bar{M}}_{M,1} & \cdots & \bar{\bar{M}}_{M,n} & \cdots & \bar{\bar{M}}_{M,N} \end{bmatrix} \begin{bmatrix} \bar{A}_1 \\ \vdots \\ \bar{A}_n \\ \vdots \\ \bar{A}_N \end{bmatrix} = \bar{0}. \tag{5-30}$$

5.5 Electromagnetic Sources

In order to include the effects of excitation antennas in our source-free solutions, we can start from the Lorentz reciprocity theorem [56, Ch. 1] considering two sets of sources $\mathbf{J}_1$, $\mathbf{M}_1$ and $\mathbf{J}_2$, $\mathbf{M}_2$ that produce the fields $\mathbf{E}_1$, $\mathbf{H}_1$ and $\mathbf{E}_2$, $\mathbf{H}_2$, respectively. Inside a volume V enclosed by the surface S, we have

$$\oint_S \Big(\mathbf{E}_1 \times \mathbf{H}_2 - \mathbf{E}_2 \times \mathbf{H}_1\Big) \cdot d\mathbf{S} = \int_V \Big(\mathbf{E}_2 \cdot \mathbf{J}_1 - \mathbf{E}_1 \cdot \mathbf{J}_2 + \mathbf{H}_1 \cdot \mathbf{M}_2 - \mathbf{H}_2 \cdot \mathbf{M}_1\Big)\, dV, \tag{5-31}$$

where $d\mathbf{S}$ is an outward-pointing vector, normal to the boundary S. As the guide is radially limited by a PEC wall, we have that the fields tangent to the surface are zero, that is, $\mathbf{E}\times\mathbf{H}\cdot\hat{z} = \mathbf{H}\cdot(\hat{z}\times\mathbf{E}) = 0$. Consequently, this reduces the surface integral in (5-31) to be over the waveguide cross-section S_0, i.e.,

$$\int_{S_0} \Big(\mathbf{E}_1 \times \mathbf{H}_2 - \mathbf{E}_2 \times \mathbf{H}_1\Big) \cdot \hat{z}\, dS = \int_V \Big(\mathbf{E}_2 \cdot \mathbf{J}_1 - \mathbf{E}_1 \cdot \mathbf{J}_2 + \mathbf{H}_1 \cdot \mathbf{M}_2 - \mathbf{H}_2 \cdot \mathbf{M}_1\Big)\, dV. \tag{5-32}$$

The forward-propagating electric and magnetic axial fields refereed at the source plane $z = z_T$ can be written in terms of cylindrical harmonics by using

$$\begin{bmatrix} E_z(\rho,\phi,z) \\ H_z(\rho,\phi,z) \end{bmatrix} = \sum_{n=-N}^{N} \sum_{p=1}^{\infty} \Big[\bar{\bar{H}}_{zn}(\beta_p\rho)\bar{A}_p + \bar{\bar{J}}_{zn}(\beta_p\rho)\bar{B}_p\Big] e^{in\phi + ik_{z,p}(z-z_T)}, \tag{5-33}$$

and

$$\bar{\bar{G}}_{zn}(\beta_p\rho) = \begin{bmatrix} G_n(\beta_p^e\rho) & 0 \\ 0 & G_n(\beta_p^h\rho) \end{bmatrix},$$

$$\bar{A}_p = \begin{bmatrix} A_p^e \\ A_p^h \end{bmatrix} \quad \text{and} \quad \bar{B}_p = \begin{bmatrix} B_p^e \\ B_p^h \end{bmatrix}, \tag{5-34}$$

where $G_n = \{H_n^{(1)}, J_n\}$ and $\beta_p^{e,h} = \alpha^{e,h} k_{\rho,p}$. The transversal (to z) fields are

obtained through (2-24) and (2-25):

$$\begin{bmatrix} E_\phi \\ H_\phi \\ E_\rho \\ H_\rho \end{bmatrix} = \frac{1}{k_\rho^2 \rho} \begin{bmatrix} ik_z \frac{\partial}{\partial \phi} & -i\omega\mu_s \rho \frac{\partial}{\partial \rho} \\ i\omega\epsilon_s \rho \frac{\partial}{\partial \rho} & ik_z \frac{\partial}{\partial \phi} \\ ik_z \rho \frac{\partial}{\partial \rho} & i\omega\mu_s \frac{\partial}{\partial \phi} \\ -i\omega\epsilon_s \frac{\partial}{\partial \phi} & ik_z \rho \frac{\partial}{\partial \rho} \end{bmatrix} \begin{bmatrix} E_z \\ H_z \end{bmatrix}. \tag{5-35}$$

The compact forms shown below are preferable:

$$\begin{bmatrix} E_\phi(\rho,\phi,z) \\ H_\phi(\rho,\phi,z) \end{bmatrix} = \sum_{n=-N}^{N} \sum_{p=1}^{\infty} \Big[\bar{\bar{H}}_{\phi n}(\beta_p \rho) \bar{A}_p + \bar{\bar{J}}_{\phi n}(\beta_p \rho) \bar{B}_p \Big] e^{in\phi + ik_{z,p}(z - z_T)}, \tag{5-36}$$

$$\begin{bmatrix} E_\rho(\rho,\phi,z) \\ H_\rho(\rho,\phi,z) \end{bmatrix} = \sum_{n=-N}^{N} \sum_{p=1}^{\infty} \Big[\bar{\bar{H}}_{\rho n}(\beta_p \rho) \bar{A}_p + \bar{\bar{J}}_{\rho n}(\beta_p \rho) \bar{B}_p \Big] e^{in\phi + ik_{z,p}(z - z_T)}, \tag{5-37}$$

with

$$\bar{\bar{G}}_{\phi n}(\beta_p \rho) = \frac{1}{k_{\rho,p}^2 \rho} \begin{bmatrix} -nk_z G_n(\beta_p^e \rho) & -i\omega\mu_s \rho \beta_p^h G_n'(\beta_p^h \rho) \\ i\omega\epsilon_s \rho \beta_p^e G_n'(\beta_p^e \rho) & -nk_z G_n(\beta_p^h \rho) \end{bmatrix}, \tag{5-38}$$

$$\bar{\bar{G}}_{\rho n}(\beta_p \rho) = \frac{1}{k_{\rho,p}^2 \rho} \begin{bmatrix} ik_z \rho \beta_p^e G_n'(\beta_p^e \rho) & -n\omega\mu_s G_n(\beta_p^h \rho) \\ n\omega\epsilon_s G_n(\beta_p^e \rho) & ik_z \rho \beta_p^h G_n'(\beta_p^h \rho) \end{bmatrix}. \tag{5-39}$$

If the forward-propagating fields ($z > z_T$) associate ($+k_{z,p}$, E_z, H_z, $\mathbf{E}_s$, $\mathbf{H}_s$) are proper solutions for the Maxwell's equations, the mirror mode [57, Ch. 15.7], [27, Sec. 3.3.5] ($-k_{z,p}$, $-E_z$, H_z, $\mathbf{E}_s$, $-\mathbf{H}_s$) is also a solution. Then, we can write

$$\begin{aligned} \mathbf{E}^\pm &= \sum_{p=1}^{\infty} A_p^\pm \Big[\mathbf{e}_{s,p}^\pm(\rho,\phi) + \hat{z} e_{z,p}^\pm(\rho,\phi) \Big] e^{\pm ik_{z,p}(z - z_T)} \\ &= \sum_{p=1}^{\infty} A_p^\pm \Big[\mathbf{e}_{s,p}^+(\rho,\phi) \pm \hat{z} e_{z,p}^+(\rho,\phi) \Big] e^{\pm ik_{z,p}(z - z_T)}, \end{aligned} \tag{5-40}$$

$$\begin{aligned} \mathbf{H}^\pm &= \sum_{p=1}^{\infty} A_p^\pm \Big[\mathbf{h}_{s,p}^\pm(\rho,\phi) + \hat{z} h_{z,p}^\pm(\rho,\phi) \Big] e^{\pm ik_{z,p}(z - z_T)} \\ &= \sum_{p=1}^{\infty} A_p^\pm \Big[\pm \mathbf{h}_{s,p}^+(\rho,\phi) + \hat{z} h_{z,p}^+(\rho,\phi) \Big] e^{\pm ik_{z,p}(z - z_T)}, \end{aligned} \tag{5-41}$$

for $z \gtrless z_T$. Notice in the above we adopted a compact notation where $g_{\alpha,p}^+(\rho,\phi)$

is the portion of the fields that depend on (ρ, ϕ), with $g^+_{\alpha,p} = \{e^+_{\alpha,p}, h^+_{\alpha,p}\}$, $\alpha = \{\rho, \phi, z\}$, given by (5-33), (5-36) and (5-37). It is important to note that $g^+_{\alpha,p}$ also carries the azimuth sum over n. Since the modes are orthogonal over the cross-section of the waveguide, we can derive the following conditions:

$$\int_S \mathbf{E}^\pm_p \times \mathbf{H}^\pm_{p'} \cdot \hat{z}\, dS = \int_S \mathbf{E}^\pm_p \times \mathbf{H}^\mp_{p'} \cdot \hat{z}\, dS = 0, \quad \text{for} \quad p \neq p'. \tag{5-42}$$

For solving the source excitation amplitudes $A^\pm_p$, let us go back to (5-32). We assume first that $\mathbf{J}_1 = \mathbf{J}$ and $\mathbf{M}_1 = \mathbf{M}$, and $\mathbf{J}_2 = \mathbf{0}$ and $\mathbf{M}_2 = \mathbf{0}$. For the fields with subscript 1, we have $\mathbf{E}_1 = \mathbf{E}^\pm$ and $\mathbf{H}_1 = \mathbf{H}^\pm$ for $z \lessgtr z^\pm_T$. For fields with the subscript 2, we chose the pth waveguide mode propagating in the negative z-direction, i.e.,

$$\mathbf{E}_2 = \mathbf{e}^-_p, \tag{5-43}$$

$$\mathbf{H}_2 = \mathbf{h}^-_p. \tag{5-44}$$

Substituting the above in (5-32), we can obtain

$$\begin{aligned}&\int_{S^+_0} A^+_p \left(\mathbf{E}^+_p \times \mathbf{h}^-_p - \mathbf{e}^-_p \times \mathbf{H}^+_p\right) \cdot \hat{z}\, dS \\ &- \int_{S^-_0} A^-_p \left(\mathbf{E}^-_p \times \mathbf{h}^-_p - \mathbf{e}^-_p \times \mathbf{H}^-_p\right) \cdot \hat{z}\, dS = \int_V \left(\mathbf{e}^-_p \cdot \mathbf{J} - \mathbf{h}^-_p \cdot \mathbf{M}\right) dV.\end{aligned} \tag{5-45}$$

We can readily notice that the second surface integral vanishes for any p, and allows us to write

$$\int_{S^+_0} A^+_p \left[e^+_{\rho,p} h^-_{\phi,p} - e^+_{\phi,p} h^-_{\rho,p} - (e^-_{\rho,p} h^+_{\phi,p} - e^-_{\phi,p} h^+_{\rho,p})\right] dS = \int_V \left(\mathbf{e}^-_p \cdot \mathbf{J} - \mathbf{h}^-_p \cdot \mathbf{M}\right) dV. \tag{5-46}$$

Then, we can obtain A^+_p via

$$A^+_p = \frac{S^+_p}{N^+_p}, \tag{5-47}$$

where

$$\begin{aligned}S^+_p = \int_V \Big[&\left(e^+_{\rho,p}\hat{\rho} + e^+_{\phi,p}\hat{\phi} - e^+_{z,p}\hat{z}\right) \cdot \mathbf{J} \\ &+ \left(h^+_{\rho,p}\hat{\rho} + h^+_{\phi,p}\hat{\phi} - h^+_{z,p}\hat{z}\right) \cdot \mathbf{M}\Big] e^{-ik_{z,p}z}\, dV,\end{aligned} \tag{5-48}$$

and

$$N_p^+ = -2\int_{S_0^+}\left(e_{\rho,p}^+ h_{\phi,p}^+ - e_{\phi,p}^+ h_{\rho,p}^+\right) dS. \tag{5-49}$$

In order to find A_p^- we can use an analogous procedure but with $\mathbf{E}_2 = \mathbf{e}_p^+$ and $\mathbf{H}_2 = \mathbf{h}_p^+$. Equation (5-32) now provides

$$\begin{aligned}&\int_{S_0^+} A_p^+\left(\mathbf{E}_p^+ \times \mathbf{h}_p^+ - \mathbf{e}_p^+ \times \mathbf{H}_p^+\right)\cdot \hat{z}\, dS \\ &\quad - \int_{S_0^-} A_p^-\left(\mathbf{E}_p^- \times \mathbf{h}_p^+ - \mathbf{e}_p^+ \times \mathbf{H}_p^-\right)\cdot \hat{z}\, dS = \int_V \left(\mathbf{e}_p^+ \cdot \mathbf{J} - \mathbf{h}_p^+ \cdot \mathbf{M}\right) dV,\end{aligned} \tag{5-50}$$

and consequently, we can obtain A_p^- via

$$A_p^- = \frac{S_p^-}{N_p^-}, \tag{5-51}$$

where

$$\begin{aligned}S_p^- = \int_V \Big[&\left(e_{\rho,p}^+\hat{\rho} + e_{\phi,p}^+\hat{\phi} + e_{z,p}^+\hat{z}\right)\cdot \mathbf{J} \\ &- \left(h_{\rho,p}^+\hat{\rho} + h_{\phi,p}^+\hat{\phi} + h_{z,p}^+\hat{z}\right)\cdot \mathbf{M}\Big] e^{+ik_{z,p}z}\, dV,\end{aligned} \tag{5-52}$$

and

$$N_p^- = -2\int_{S_0^-}\left(e_{\rho,p}^+ h_{\phi,p}^+ - e_{\phi,p}^+ h_{\rho,p}^+\right) dS. \tag{5-53}$$

In summary, the source coefficient associated with the pth mode in (5-40) and (5-41) is given by

$$A_p^\pm = \frac{S_p^\pm}{N_p}, \tag{5-54}$$

where

$$\begin{aligned}S_p^\pm = \int_V \Big[&\left(e_{\rho,p}^+\hat{\rho} + e_{\phi,p}^+\hat{\phi} \mp e_{z,p}^+\hat{z}\right)\cdot \mathbf{J} \\ &\pm \left(h_{\rho,p}^+\hat{\rho} + h_{\phi,p}^+\hat{\phi} \mp h_{z,p}^+\hat{z}\right)\cdot \mathbf{M}\Big] e^{\mp ik_{z,p}z}\, dV.\end{aligned} \tag{5-55}$$

and $N_p = N_p^+ = N_p^-$.

Table 5.1: Axial wavenumber of HE_{11} and TM_{01} modes for different numbers of points N.

N	1	2	3	4	5	CST	RPM
TM_{01}	240.509	217.996	217.959	217.925	217.966	218.488	222.373
HE_{11e}	373.759	376.937	375.651	375.683	375.692	376.244	376.747
HE_{11o}	370.071	370.890	375.189	375.518	375.618		

5.5.1 Electric and Magnetic Coil Antenna Source

Consider the excitation of an electric and magnetic loop placed at $z = z_T$ and defined by the surface current densities

$$\mathbf{J} = j_T \boldsymbol{\delta}_T, \tag{5-56a}$$

$$\mathbf{M} = m_T \boldsymbol{\delta}_T, \tag{5-56b}$$

where $j_T = j_0 \rho_T$ and $m_T = m_0 \rho_T$ are defined as the electric and magnetic moments, respectively, of a coil with radius ρ_T, and

$$\boldsymbol{\delta}_T = \frac{\delta(\rho - \rho_T)}{\rho} \delta(z - z_T) \hat{\phi}. \tag{5-57}$$

By replacing (5-56) in (5-55), we obtain

$$S_p^{\pm} = e^{\mp i k_{z,p} z_T} \int_0^{2\pi} \Big[j_T e_{\phi,p}^{+}(\rho_T, \phi) \pm m_T h_{\phi,p}^{+}(\rho_T, \phi) \Big] d\phi. \tag{5-58}$$

5.6 Numerical Results and Discussions

In order to test and validate our method, a series of different structures were simulated, analyzed and compared with results present in the literature.

5.6.1 Circular Anisotropic Waveguide Filled with Anisotropic Eccentric Rod

Consider the eccentric waveguide with $r_1 = 5\text{mm}$, $r_0 = 0.1 r_1$ and $d = 0.23 r_1$, the regions I and II are characterized by tensors $\mu_{\text{I\II}} = \text{diag}(\mu_{rs,\text{I\II}}, \mu_{rs,\text{I\II}}, \mu_{rz,\text{I\II}})\mu_0$ and $\epsilon_{\text{I\II}} = \text{diag}(\epsilon_{rs,\text{I\II}}, \epsilon_{rs,\text{I\II}}, \epsilon_{rz,\text{I\II}})\epsilon_0$ the waveguide operate in a frequency of 25GHz. The Table 5.1 shows the axial wavenumber of the HE_{11} and TM_{01} modes for different amounts of points, for the case where de medium II is vacuum and medium I has anisotropic

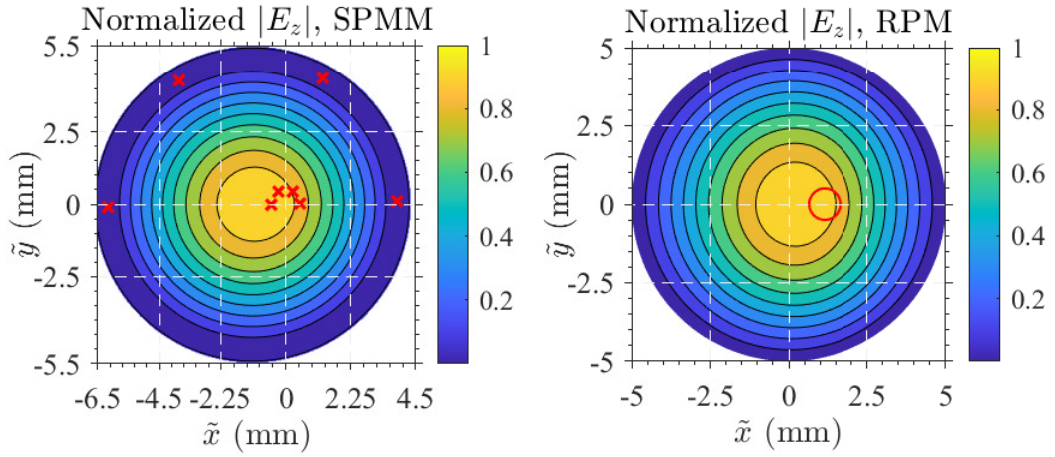

Figure 5.3: Normalized axial electric field of TM_{01} mode patterns calculated using SPMM (left) and RPM (right). The points used in SPMM are marked in red x and the circle with red bold line delimits the inner rod, i.e., region I.

characteristics described by $\mu_{rs,\mathrm{I}} = \mu_{rz,\mathrm{I}} = 1$, $\epsilon_{rz,\mathrm{I}} = 3.6$ and $\epsilon_{rs,\mathrm{I}} = 1.6$, in addition we also consider the values of k_z obtained by software CST and RPM methods.

In Fig. 5.3, the axial field pattern of the TM_{01} mode for $N = 3$ is illustrated, we also highlight the points used to apply the boundary conditions of the method (observe the markers at $\times$), we can see that the E_z field satisfies the boundary conditions on the outer conductor and mainly on the highlighted points and also a good agreement with the results obtained with RPM.

In Fig. 5.4, we show k_z for HE_{11} and TM_{01} modes considering different combinations of anisotropy, since in upper graph we have $\mu_{rs,\mathrm{I\backslash II}} = \mu_{rz,\mathrm{I\backslash II}} = 1.0\backslash 1.0$, $\epsilon_{rz,\mathrm{I\backslash II}} = 3.6\backslash 1.0$ and $\epsilon_{rs,\mathrm{I\backslash II}} = [1.6 \cdots 5.6]\backslash 1.0$ for HE_{11} mode, and for TM_{01} mode we interchange the $\epsilon_{rs,\mathrm{I}}$ and $\epsilon_{rz,\mathrm{I}}$. In down graph we consider a case where all media have anisotropic characteristic both in magnetic permeability and electrical permittivity described by $\mu_{rs,\mathrm{I\backslash II}} = 5.6\backslash 1.6$, $\mu_{rz,\mathrm{I\backslash II}} = 1.6\backslash 5.6$ $\epsilon_{rz,\mathrm{I\backslash II}} = 3.6\backslash 5.6$ and $\epsilon_{rs,\mathrm{I\backslash II}} = [1.6 \cdots 5.6]\backslash 1.6$ for HE_{11} mode, and for TM_{01} mode we interchange $\epsilon_{rs,\mathrm{I}}$ by $\epsilon_{rz,\mathrm{I}}$. In both graphs we can see a good agreement between the results obtained by our method, CST (based-FIT) and RPM.

5.6.2 Circular-Elliptical and Elliptical-Circular Waveguide

Let the guides in Fig. 5.5 are filled with vacuum and their walls are composed of PEC, r_0 is the radius of the circle, r_1 is the longest length of the ellipse in the direction of x and $e = f/r_1$ is the eccentricity with f being the focus of the ellipse. In Table 5.2, we compare the axial wavenumbers of

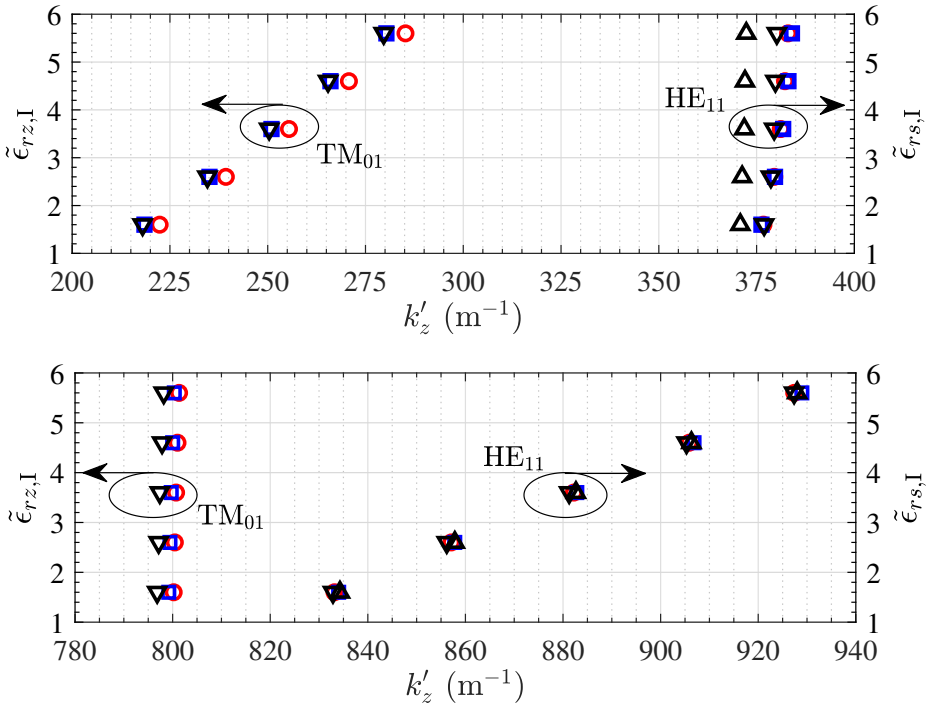

Figure 5.4: Axial wavenumbers of HE_{11} mode with $\epsilon_{rz,\mathrm{I}} = 3.6$ fixed and TM_{01} mode with $\epsilon_{rs,\mathrm{I}} = 3.6$ fixed. In upper graphic the region II is isotropic material and for lower graphic we consider full anisotropic material with $\mu_{rz,\mathrm{I\backslash II}} = 1.6\backslash 5.6$, $\mu_{rs,\mathrm{I\backslash II}} = 5.6\backslash 1.6$ and $\epsilon_{rz,\mathrm{II}} = 5.6$ and $\epsilon_{rz,\mathrm{II}} = 1.6$ obtained by FIT ($\square$), second-order RPM ($\circ$), SPMM even ($\triangledown$) and SPMM odd ($\triangle$).

the first TE modes present for each waveguide. Fig. 5.6, shows the results considering the IPMM, the magnetic field pattern of the TE_{11} even and odd modes for circular-elliptic configuration considering $h = 0.7$, $r_1/r_0 = 2$, $N = 3$ and $P = 7$, in addition we also show the field pattern retrieved from [58].

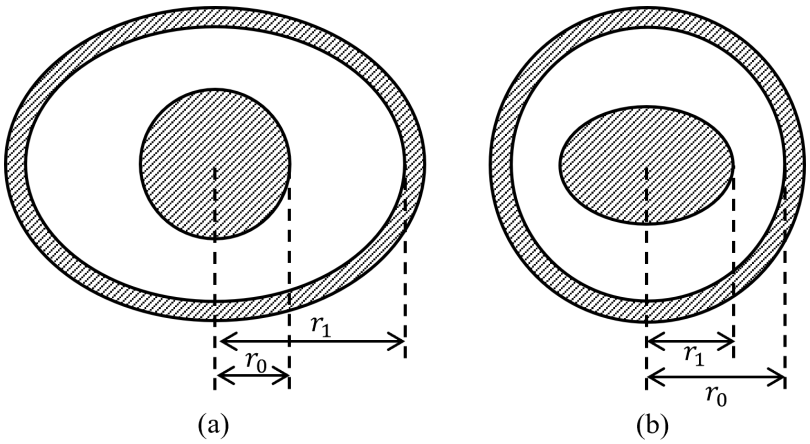

Figure 5.5: Geometry of (a) an coaxial elliptical-circular waveguide and (b) a circular-elliptical waveguide.

Table 5.2: Comparison of the longitudinal wavenumbers obtained via our implementations SPMM and IPMM with $N = 3$ with results from the work [58]. Value parameter $e = 0.2$.

Elliptical-circular waveguide with $r_1/r_0 = 2/3$					
Mode	SPMM		IPMM		[58]
	$N = 4$	$N = 6$	$P = 5$	$P = 7$	
TE_{11e}	20.9545	20.9545	20.9545	20.9546	20.9567
TE_{21e}	20.9429	20.9431	20.9435	20.9432	20.9515
TE_{31e}	20.9240	20.9246	20.9238	20.9234	20.9429
TE_{11o}	20.9546	20.9547	20.9547	20.9548	20.9567
TE_{21o}	20.9429	20.9429	20.9429	20.9431	20.9515
TE_{31o}	20.9236	20.9237	20.9239	20.9242	20.9429
Circular-elliptical waveguide with $r_1/r_0 = 3/2$					
Mode	SPMM		IPMM		[58]
	$N = 4$	$N = 6$	$P = 5$	$P = 7$	
TE_{11e}	20.9545	20.9547	20.9547	20.9547	20.9567
TE_{21e}	20.9426	20.9428	20.9427	20.9428	20.9515
TE_{31e}	20.9229	20.9234	20.9234	20.9235	20.9428
TE_{11o}	20.9542	20.9544	20.9544	20.9544	20.9566
TE_{21o}	20.9421	20.9428	20.9428	20.9429	20.9515
TE_{31o}	20.9197	20.9234	20.9238	20.9234	20.9428

5.6.3 Coaxial Waveguide with Arbitrary Cross-Section

In Fig. 5.7(a) we consider a waveguide composed initially by an outer circular PEC of radius $r_1 = 5$mm and filled with vacuum, an inner PEC of radius $r_0 = 0.1r_1$ with eccentricity $d = 0.2r_1$, both circumference are described by points highlighted with $\times$. Then we deform the two lateral points on the left by reducing their radii (coordinate ρ) to $\rho = \{0, 5, 10, 15, 20\}\%$ as shown In Fig. 5.7(a). The field pattern E_z of the TM_{01} mode was obtained for each deformed waveguide using formulation based in exponential presented in (5-2) with $N = 4$, to facilitate the observation of the boundary conditions on the guide walls we also highlight the points used by the method, we can see that they are satisfied mainly over the points.

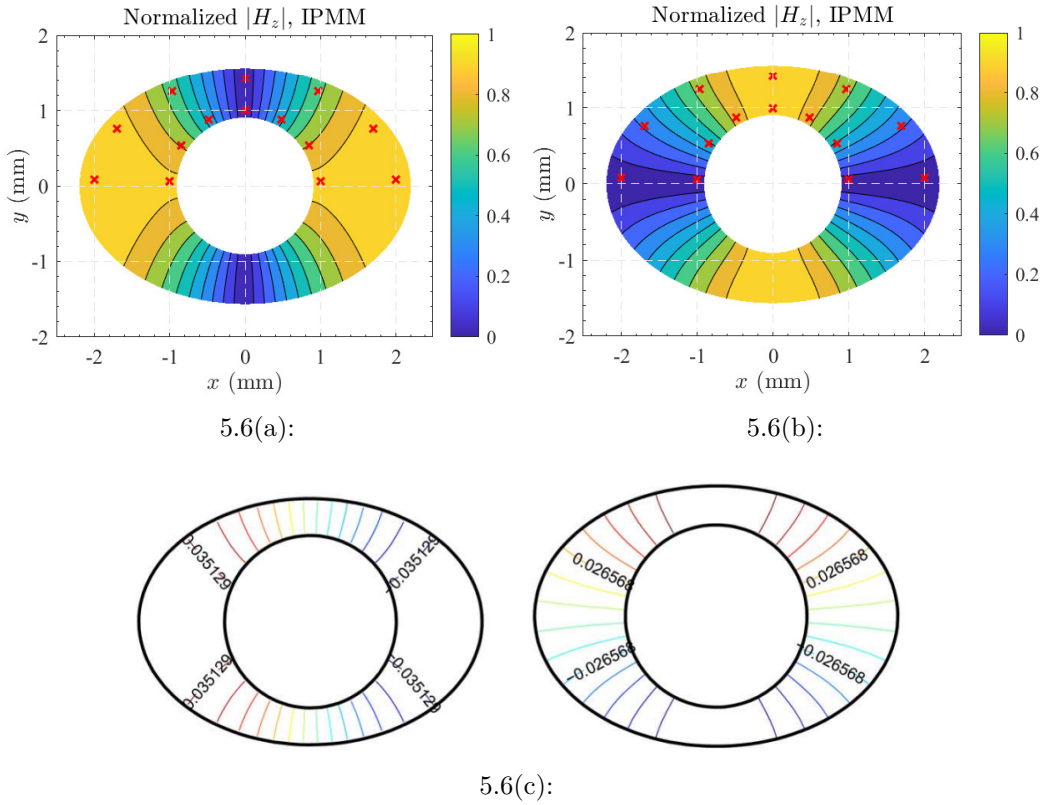

5.6(a): 5.6(b): 5.6(c):

Figure 5.6: Normalized axial field patterns calculated via the IPMM with $N = 3$ and $P = 7$. (a) TE_{11} even mode. (b) TE_{11} odd mode. (c) TE_{11} even (left) and odd (right) modes retired from [58].

5.6.4 Circular and Non-Circular Tunnel Propagation

Consider the scenario proposed in [59, 60] where a tunnel with a circular cross-section is excited by an electric loop antenna located in the center of the tunnel, see Fig. 5.8(a). The system operates at a frequency of 1 GHz, the tunnel has a radius $r_1 = 2$ m and is filled with vacuum, the external medium is characterized by a non-magnetic medium with isotropic permittivity $\epsilon_2 = \epsilon_0\epsilon_{r2} - i\sigma_2/\omega$, where$\epsilon_{r2} = 12$ and $\sigma_2 = 0.02$ S/m. The looped source, described by J_ϕ has a radius $r_S = 0.1$ m with electrical moment $j_S = I_S r_1$ and $I_S = 1$ Amp. In order to study the characteristics of tunnel propagation, we implemented the algorithm according to the flowchart shown in Fig. 5.9, where both the SPMM and IPMM formulations can be used and combined with the source formulation described in Section 5.5.

For this scenario, we consider that medium 2 is unbounded, in order to check the eigenvalue of this structure in Fig. 5.10 show the zeros ($\circ$) found by SPMM, in addition, the eigenvalues found using reference [61] for $n = 0$ and $n = 1$ highlighted by the symbols triangle ($\triangle$) and square ($\square$), respectively. It

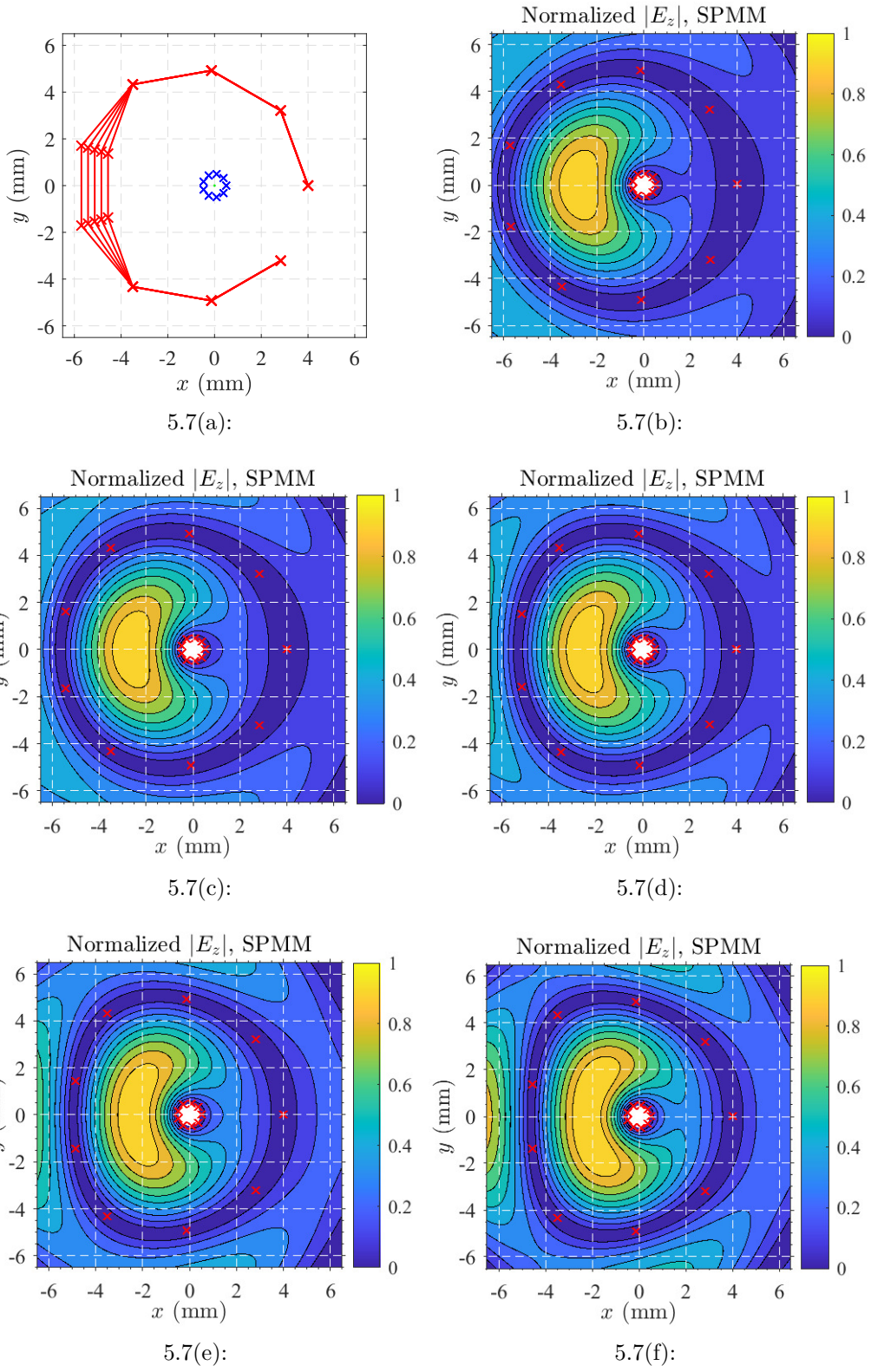

Figure 5.7: Normalized axial electric field patterns of TM_{01} calculated via the SPMM with $N = 4$ and different deformations. (a) Geometry of eccentric waveguides with different percentages of deformations. (b) 0%. (c) 5%. (d) 10%. (e) 15%. (f) 20%.

is important to comment that at this point, it is not possible to distinguish, in a simple way, which of these modes found by SPMM have $n = 0$ and $n = 1$, for this type of classification, an individual analysis of the field pattern of each mode would be necessary.

In Fig. 5.11 show the transversal electric E_ϕ field along the axial distance z inside the tunnel. In this simulation, all 12 eigenvalues found in Fig. 5.10 were considered $N = 1$ and $P = 3$. We can observe a good agreement, remembering that the results obtained from [60] considered 16 TE_{0j} modes with $j = 1, ..., 16$ in the solution, while our approach considered only the first 6 modes of the structure.

In addition, In Fig. 5.12 we compare the modes found by SPMM with $N = 4$ with values obtained using the [60] approach. We can notice a good agreement between the modes, except in the region where the higher order modes begin to appear, it is also important to comment that the order of magnitude of the search plan compared to the results of $N = 1$, as the functions present in the matrix of determinants is periodic overflow problems begin to become relevant. Fig. 5.13 shows the E_ϕ field component along z considering $N = 4$. As we expected, the result holds with good agreement, because the new added modes are of high order, and as discussed in [59], the electric loop source excites only TE modes with $n = 0$.

Fig. 5.14 illustrates the E_ϕ field pattern of the two main modes $k_z = \{20.8707 + 0.0012i, 20.6627 + 0.0041i\}$ excited by the antenna, these modes can be classified as TE_{01} and TE_{02}, respectively, also considering a distance of 1 km in the tunnel and formulation with $N = 4$.

Fig. 5.15 shows the k_z plane, as well as the modes found by IPMM considering $N = 1$ and $P = 9$. These modes are used to calculate the E_ϕ field along z shown in Fig. 5.16 and in Fig. 5.17 shows the E_ϕ field pattern in the plane (ρ, ϕ) situated at a distance $z = 1$ km.

In order to analyze the tunnel shown in Fig. 5.8(b), where the characteristics of the medium is the same of the circular tunnel, except for the non-circular geometry of the wall that was deformed symmetrically around the x axis, this deformity aims to simulate a more realistic geometry for tunnels and also to preserve the position $(\rho = 0.6, \phi = 0)$ of reception at which the field will be measured along the distance z of the tunnel.

Before analyzing the more realistic scenario, we will consider other cross-sections with milder deformities and, also, use different numbers of points. In Fig. 5.18(a) we have two scenarios where only the two points on the left side were shifted 10% and 20% towards the origin, respectively.

Fig. 5.19(a) show the first eigenvalues (k_z) considering $N = 1$ and

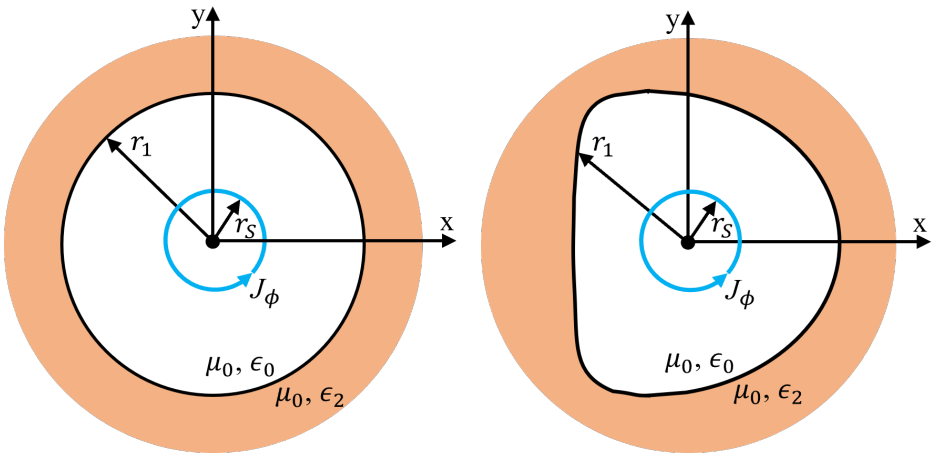

5.8(a): 5.8(b):

Figure 5.8: Geometry of circular (a) with $r_1 = 2$ m and non circular (b) tunnel with electric loop antenna (J_ϕ). The medium is described by $\epsilon_2 = \epsilon_{r2}\epsilon_0 + i\sigma_2/\omega$ where $\epsilon_{r2} = 12$, $\sigma_2 = 0.02$ S/m and operating at frequency of 1 GHz.

$P = \{9, 30\}$. Notice the variation in the high order modes, as well as the emergence of new modes compared to the eigenvalues of the circular tunnel, the variation due to the number of points is also noticeable in high order modes. In Fig. 5.19(b) show de eigenvalues for the second deformity (of 20%). Fig. 5.20(a) compares the field E_ϕ along z of the circular tunnel with the first deformed case, we can see the presence of the fundamental propagating modes in the far field region, similar to the circular tunnel. In Fig. 5.20(b) shows the E_ϕ field along z referring to the second deformity, where all the eigenvalues listed In Fig. 5.19(b) were considered.

Finally, In Fig. 5.21 are the results for the tunnel with the most realistic cross-section, in this case, as the deformity is more severe, it is also expected that there will be a difference between the results obtained using P={9,30}. However, the fundamental modes (see Fig. 5.21(a)) show excellent agreement, which can also be observed in the field pattern in the region far from the source (far field) (see Fig. 5.21(b)). In Fig. 5.22 we see the E_ϕ field pattern in the tunnel's cross-section at a distance $z = 1000$ m considering $P = 30$, all the points used in the integration applied in the continuity condition on the tunnel wall are also highlighted.

5.6.5 Coaxial Waveguide Filled with 2 Dielectric Layers

Consider the coaxial waveguide along z and with cross-section is illustrated in Fig. 5.23. The guide is delimited by two PECs located at r_1 and r_2, and filled by two uniaxially anisotropic dielectric layers characterized by

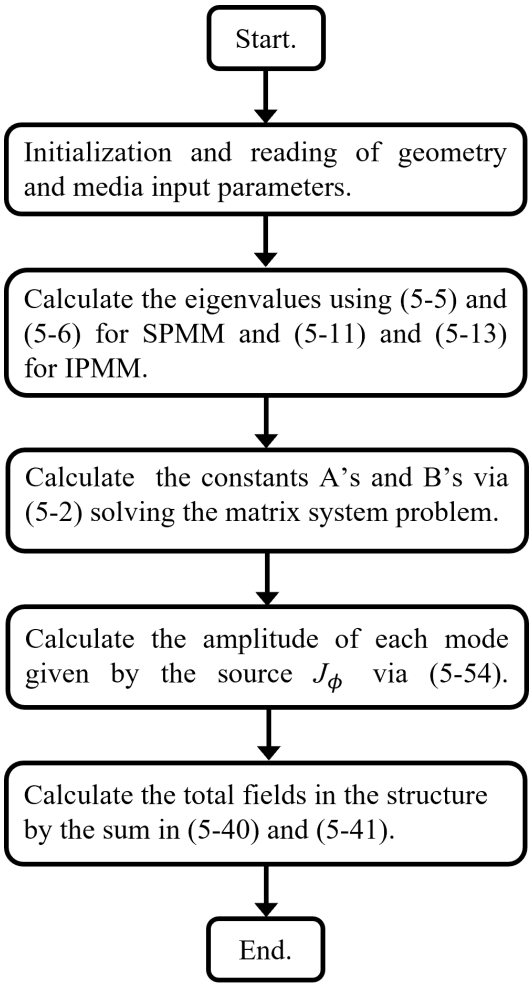

Figure 5.9: Flowchart for algorithm execution for tunnel analysis.

$p_j = \text{diag}(p_{j,s}, p_{j,s}, p_{j,z})$ where $p = \{\mu, \epsilon\}$ and $j = \{1, 2\}$ referring to the first and second layers, respectively. Furthermore, the dielectric layers are delimited by an arbitrary boundary r_l.

In order to check the validity of the method for this scenario, we consider that the boundary between the dielectrics is circular with $r_l = 15$ mm, the two dielectric layers are characterized by $\epsilon_1 = 2\epsilon_0$, $\epsilon_2 = \epsilon_0$ and $\mu_{1,2} = \mu_0$, with the radii $r_1 = 10$ mm and $r_2 = 20$ mm. In Fig. 5.24, the dispersion curve of the TM_{00}, TM_{01}, TM_{02} and TM_{03} modes is illustrated, the results were obtained considering the SPMM with $N = 1$ and the exponential formulation, we can see a good agreement with the results obtained in [27, 62].

The table 5.3 lists the eigenvalues obtained by SPMM and IPMM for the guide of the previous example considering different anisotropy combinations, where $\epsilon_{1,rs} = 4$, $\epsilon_{1,rz} = 2$, $\epsilon_{2,rs} = 3$ and when $\epsilon_{2,rz} = \{1, 2, 3, 4, 5\}$, the operating frequency used is 1 GHz.

In Fig. 5.25 shows the dispersion curve, calculated by IPMM with $N = 1$ and $P = 7$, for this results we consider that the boundary between the

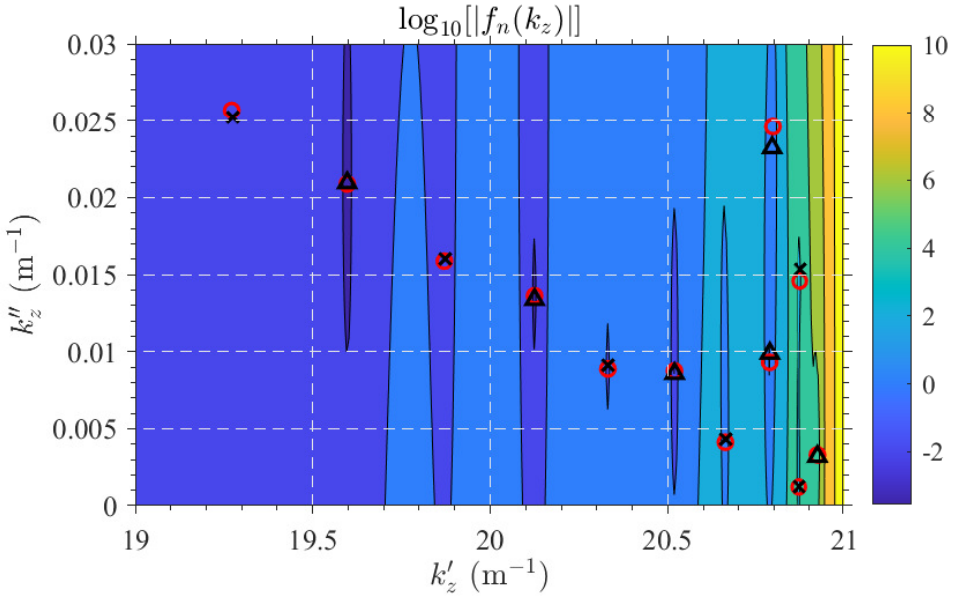

Figure 5.10: Plane $k_z = k_z' + ik_z''$, the circles ($\circ$) are eigenvalues calculated by SPMM for $n = \{0, 1\}$, and markers $\times$ and $\triangle$ are obtained using [61] for $n = 0$ and $n = 1$, respectively.

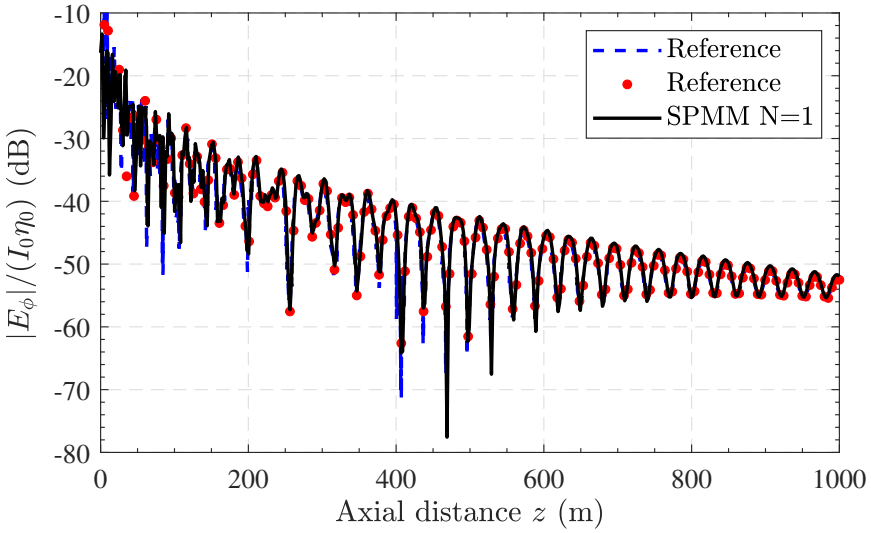

Figure 5.11: Electric field along the distance z calculated by our approach (solid line). The dashed line and small dots are results obtained in [60].

dielectrics has an elliptical shape, where the longest length of the ellipse in the direction x has a length of 15 mm and the eccentricity $e = 0.4$.

In Fig. 5.26 we can see the pattern of the fields of the mode $k_z'' = 327.264$ and $k_z'' = 327.438$ of the guide with elliptical boundary considering two different eccentricity $e = 0.4$ and $e = 0.5$, respectively, we can observe the boundary conditions were correctly enforced at the PECs as well as the continuity of the tangential fields is satisfied at the boundary between each layer.

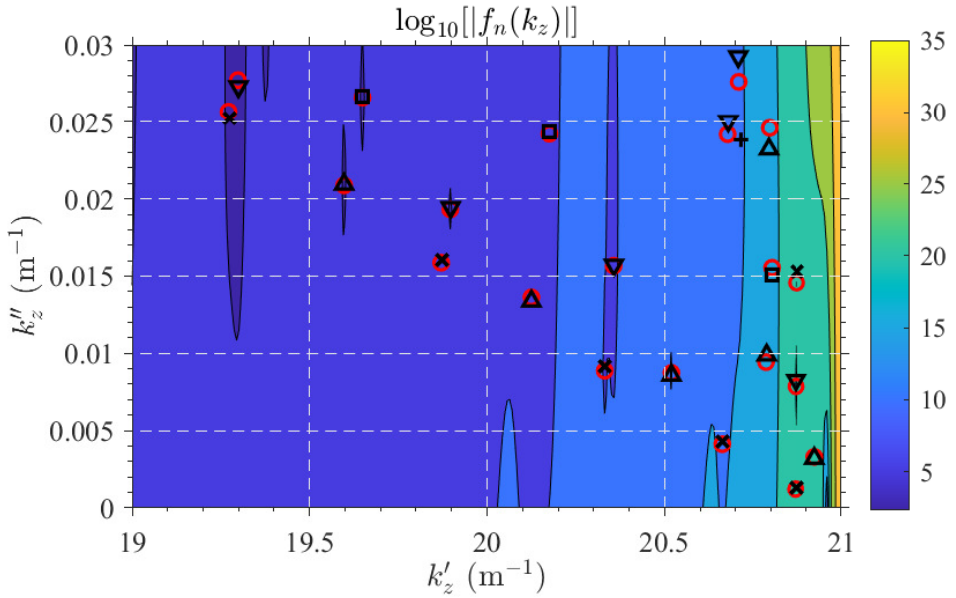

Figure 5.12: Plane $k_z = k_z' + ik_z''$ the circles ($\circ$) are eigenvalues calculated by SPMM for $N = 4$, the other markets ($\times$, $\triangle$, $\bigtriangledown$, $\square$, $+$) are calculated via [61] for $n = \{0, 1, 2, 3, 4\}$, respectively.

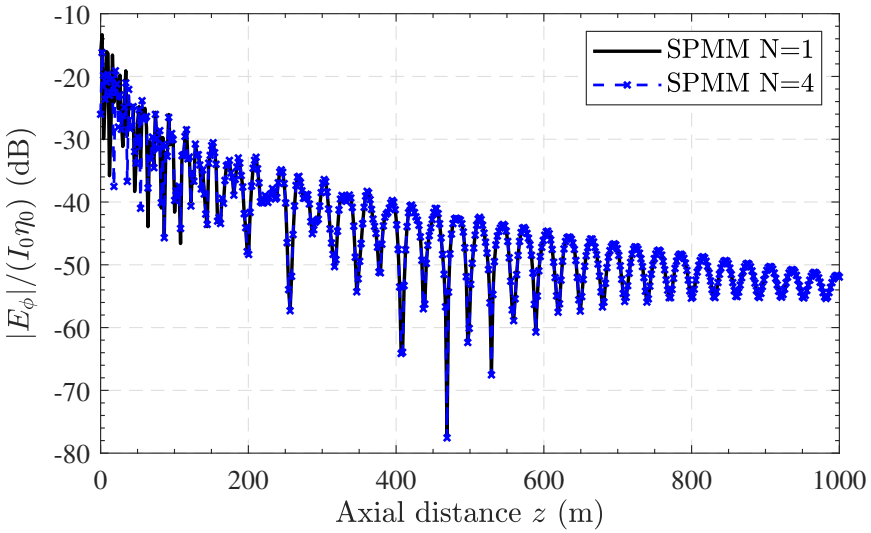

Figure 5.13: Electric field along the distance z by considering $n = 1$ (solid line) and $n = 0$ (dashed line).

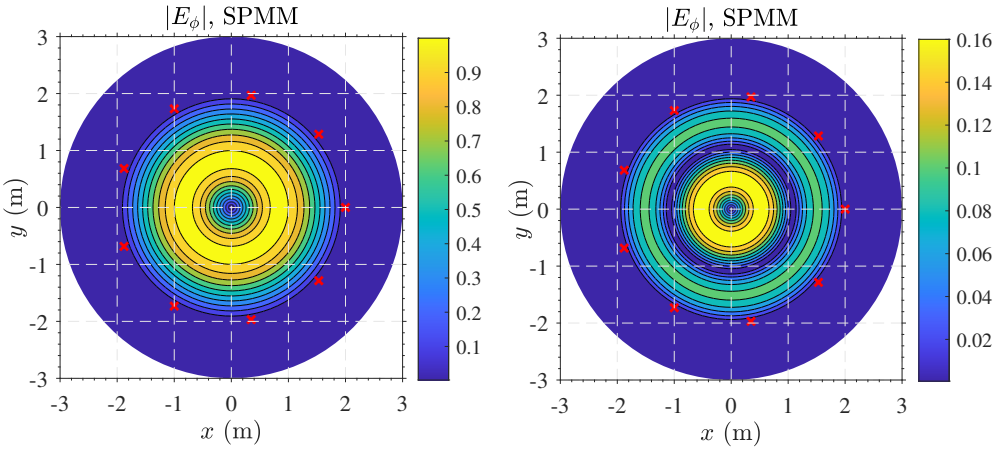

5.14(a): 5.14(b):

Figure 5.14: Transversal E_ϕ field pattern at distance of 1 km in tunnel for TE_{01} and TE_{02} modes in figures (a) and (b), respectively.

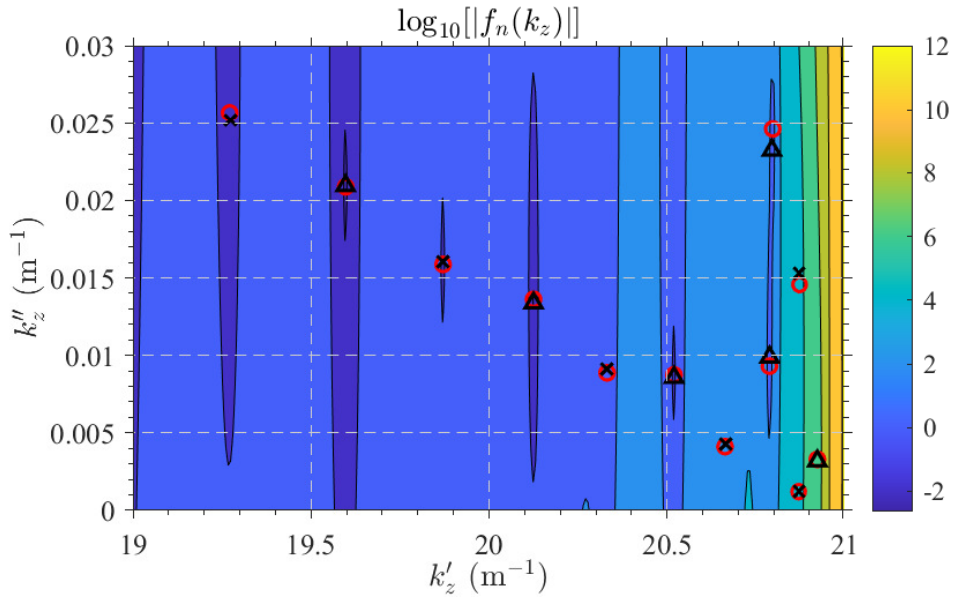

Figure 5.15: Plane $k_z = k_z' + ik_z''$, the circles ($\circ$) are eigenvalues calculated by IPMM using $N = 1$ and $P = 9$, whereas the eigenvalues illustrate by $(\times, \triangle)$ are obtained using [61] for $n = 0$ and $n = 1$, respectively.

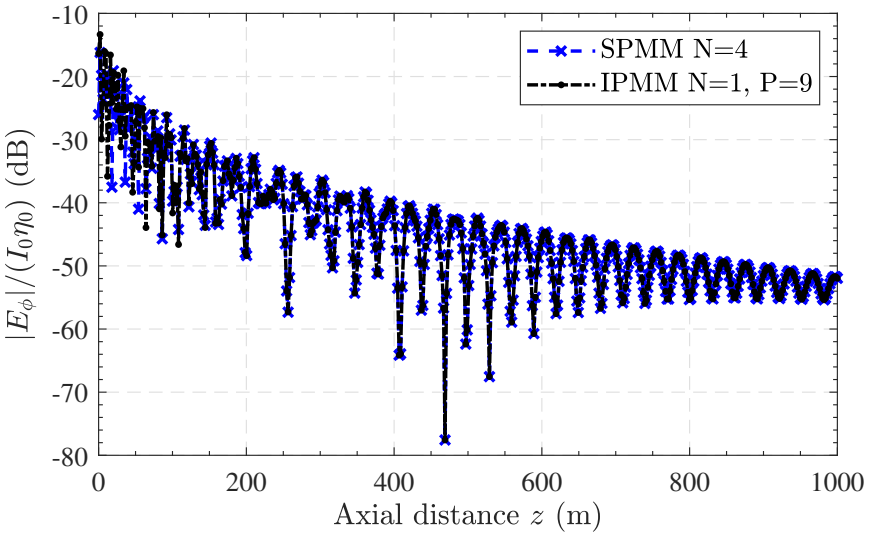

Figure 5.16: Electric field along the distance z calculated by IPMM with $N = 1$ and $P = 9$, and SPMM with $N = 4$.

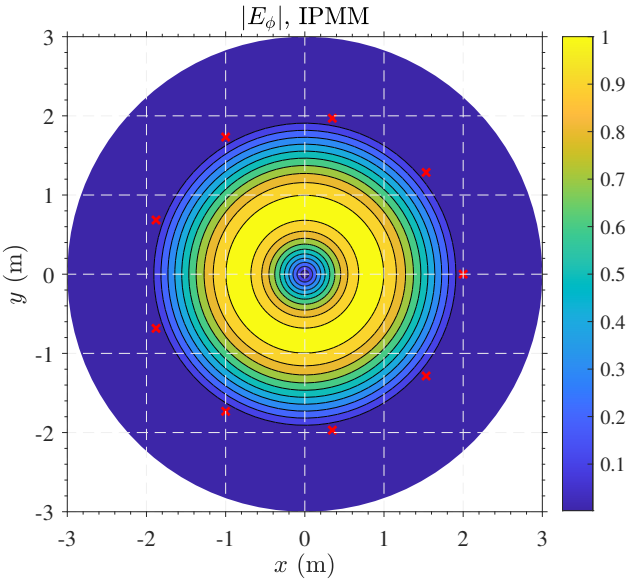

Figure 5.17: Transversal E_ϕ field pattern at distance of 1 km in tunnel.

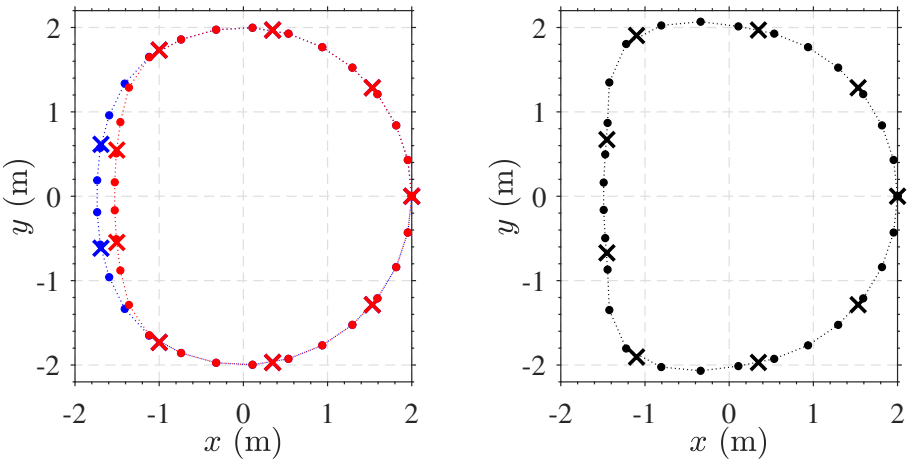

5.18(a): 5.18(b):

Figure 5.18: Geometry of the two milder (a) deformities and one (b) more severe, both scenarios considering $P = 9$ ($\times$) and an interpolation with $P = 30$ (small dots) points.

Table 5.3: Axial wavenumber k_z'' of coaxial waveguide with 2 anisotropic layers.

mode	method	$\epsilon_{2,rz}$				
		1	2	3	4	5
TM_{01}	SPMM	480.343	416.020	367.009	330.281	302.033
	IPMM	480.343	416.020	367.009	330.282	302.033
mode	method	$\epsilon_{2,rs}$				
		1	2	3	4	5
TM_{01}	SPMM	265.793	320.187	367.009	399.909	428.879
	IPMM	271.221	327.524	367.009	399.909	428.879

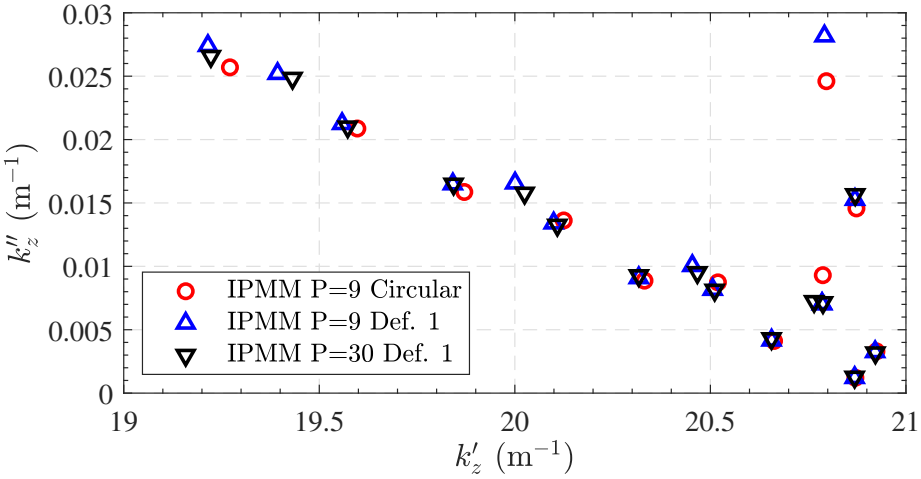

5.19(a):

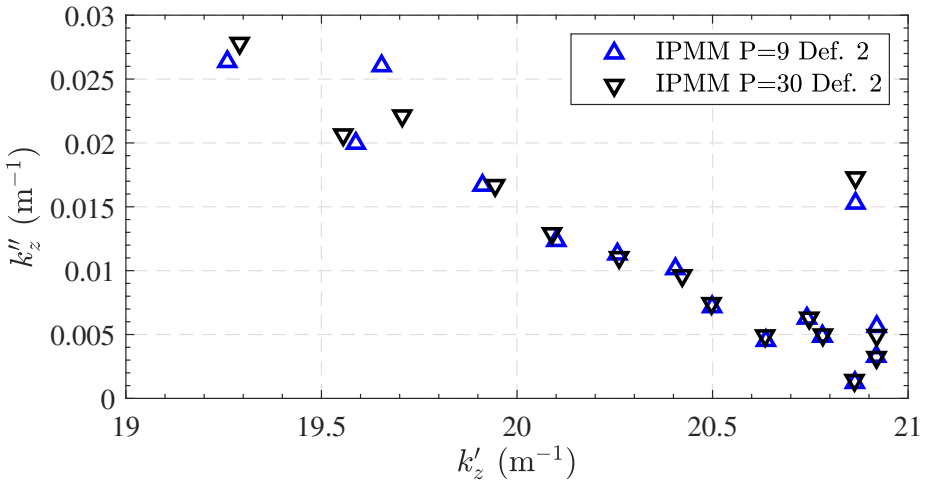

5.19(b):

Figure 5.19: First modes calculated via IPMM with $N = 1$ and $P = \{9, 30\}$ for geometry with 10% (a) and 20% (b) of deformation.

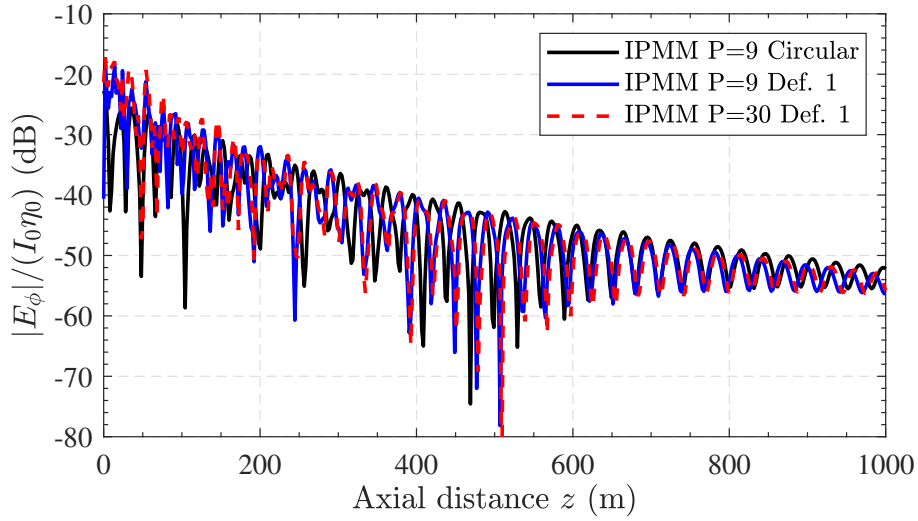

5.20(a):

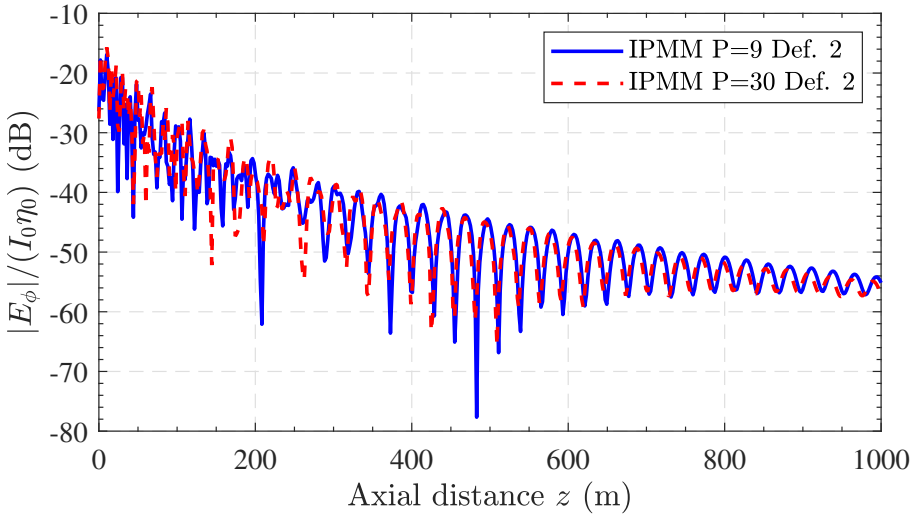

5.20(b):

Figure 5.20: Transversal E_ϕ field along the axial distance of 1 km in the first deformed cross-section.

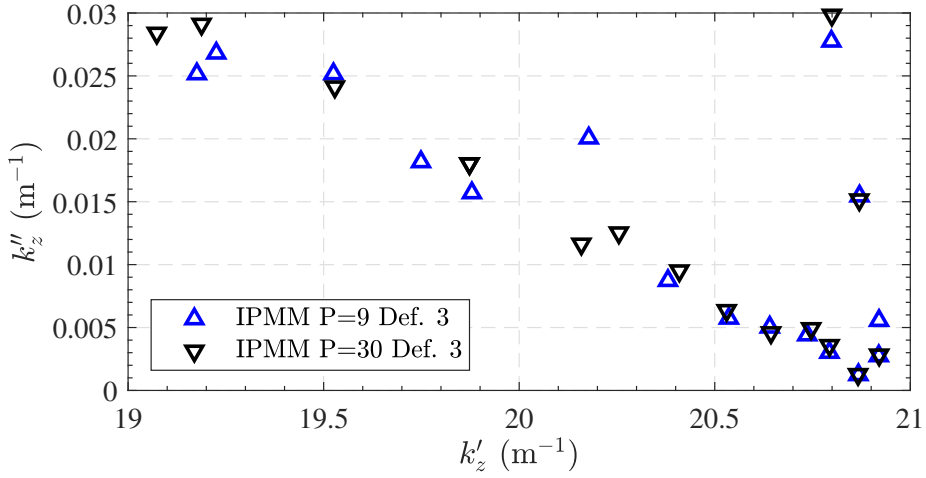

5.21(a):

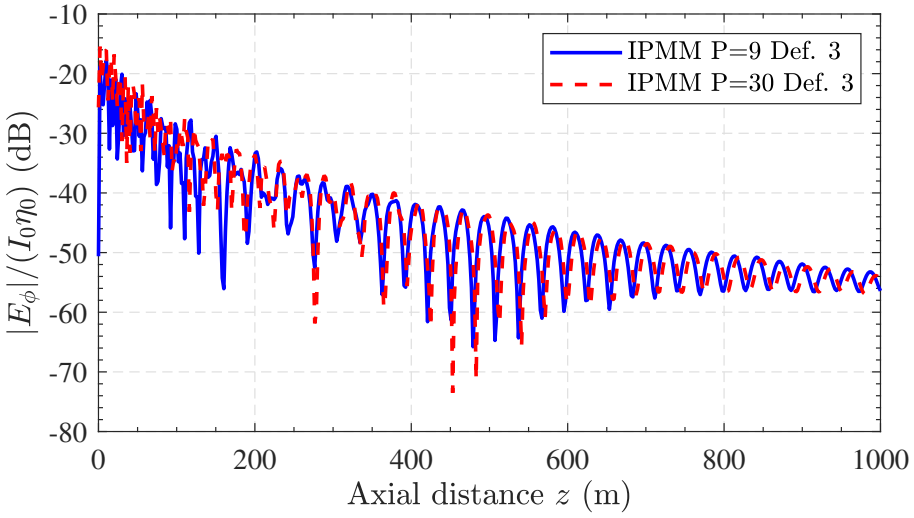

5.21(b):

Figure 5.21: Results of (a) eigenvalues and (b) field distribution along z, for third deformation and more realistic geometry of tunnel.

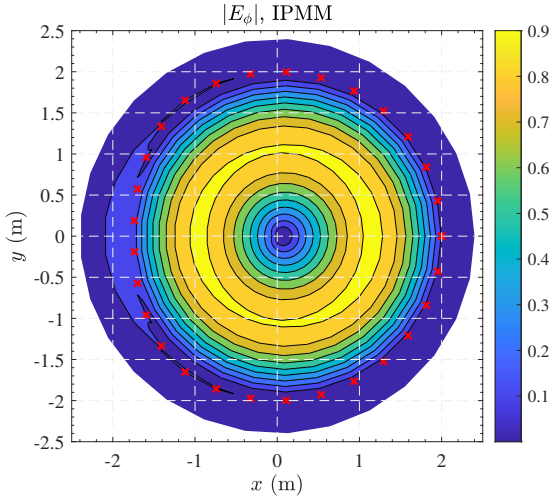

5.22(a):

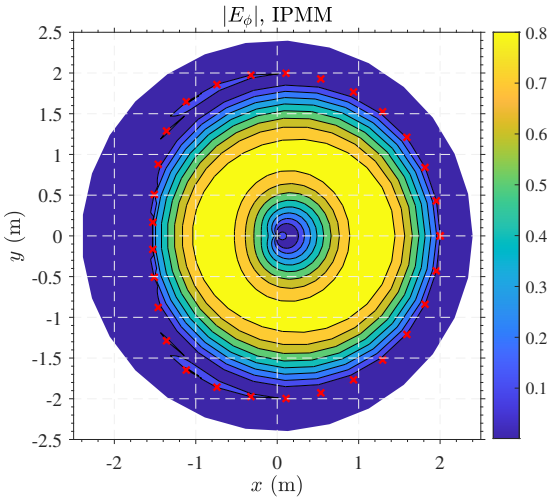

5.22(b):

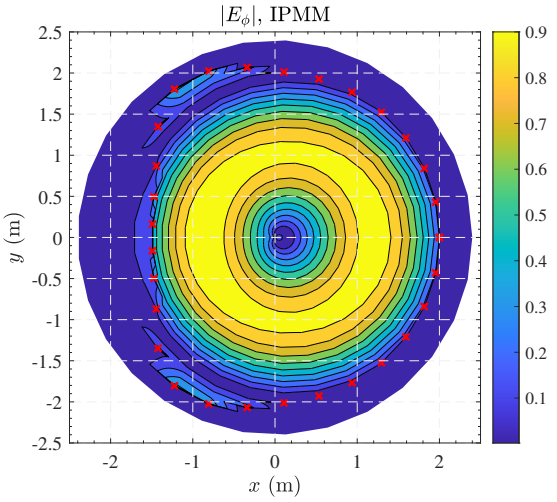

5.22(c):

Figure 5.22: Transversal E_ϕ field pattern for the first (a) second (b) and third (c) cases of deformities in cross-section of the non-circular tunnel.

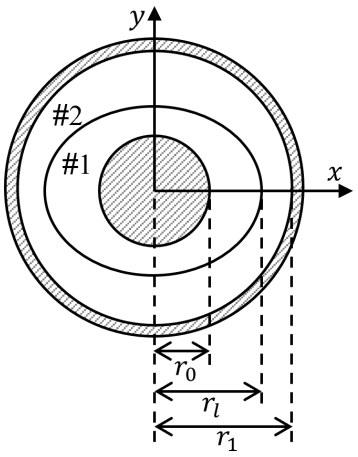

Figure 5.23: Geometry of coaxial waveguide filled with two elliptical dielectric layers.

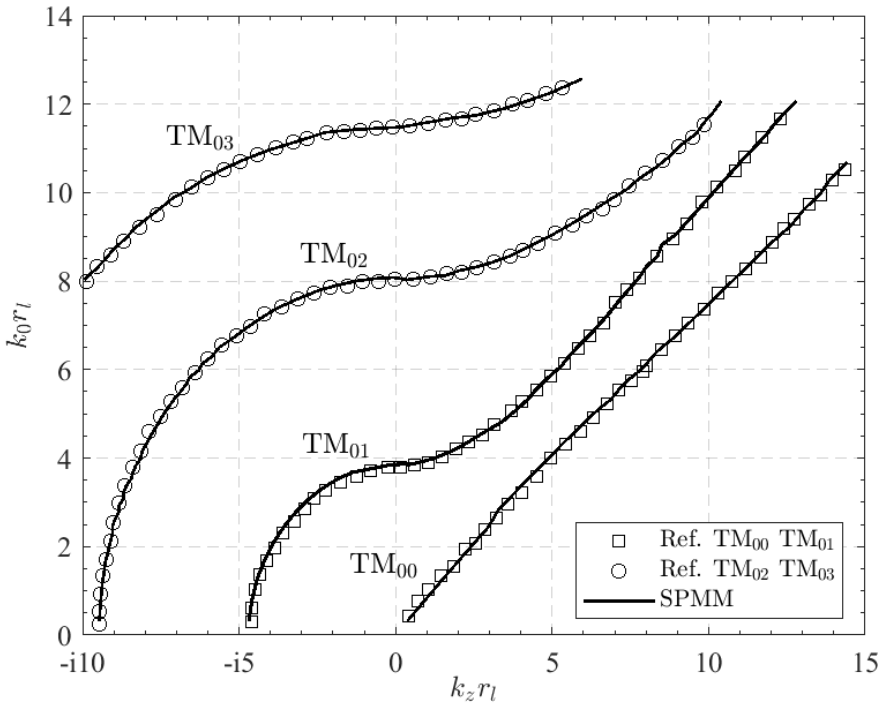

Figure 5.24: Dispersion curve for TM modes of coaxial waveguide filled with two layers, the modes of TM_{00} and TM_{01} were obtained of [62] and TM_{02} and TM_{03} by [27].

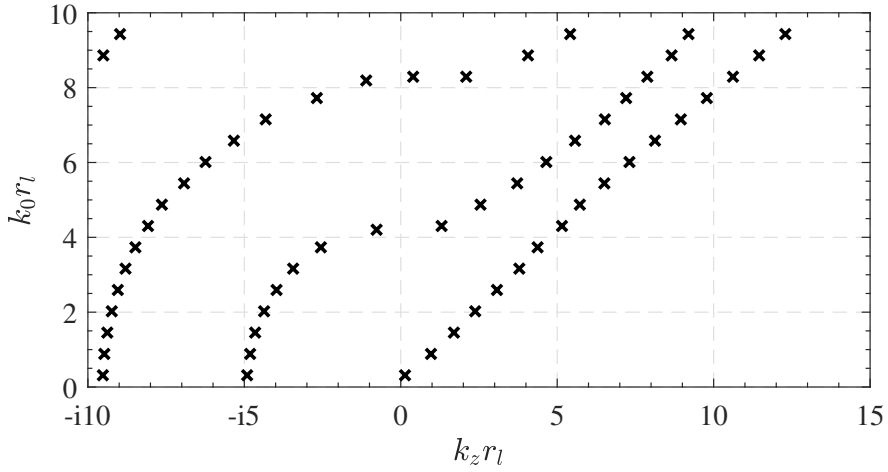

Figure 5.25: Dispersion curve of the modes of coaxial waveguide filled with two elliptical layers.

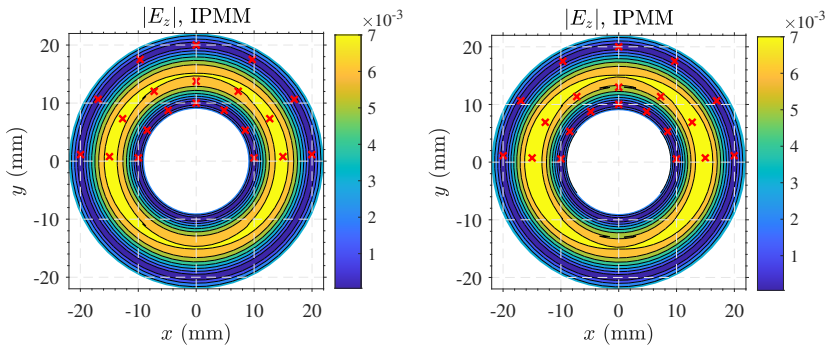

5.26(a):

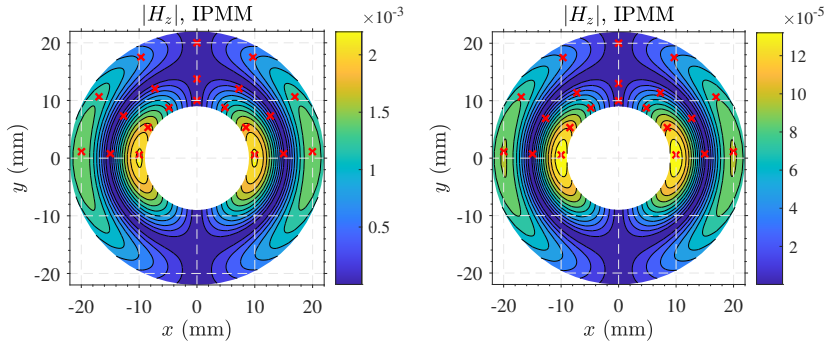

5.26(b):

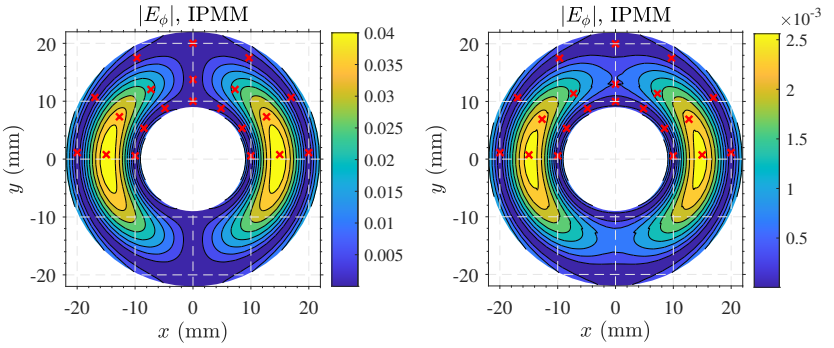

5.26(c):

Figure 5.26: Fields distribution of the coaxial waveguide filled with 2 elliptical layers with eccentricity $e = 0.4$ (left) and $e = 0.5$ (right).

6
Conclusions and Future Work

Electromagnetic analysis of cylindrical structures with arbitrary cross-sections is usually performed using computational software based on techniques such as finite-differences (FD) or finite-elements (FE). This type of approach is very attractive due to its easy implementation, on the other hand, it requires high computational power processing. Analytical models are generally obtained when the geometry of the structures conforms to the coordinate axes used in the analysis. They are attractive from a computational point of view, however, they can present great complexity in the implementation.

In this work, an analytical model, combining an optical transformation principle with a regular perturbation method (RPM) was developed in chapter 3 for the analysis of an eccentric coaxial waveguide filled with an anisotropic material. The model determines eigenvalues and fields of the modes present in this type of structure. Furthermore, the method was expanded to the case where the inner conductor is replaced by a dielectric rod. More general boundary and orthogonality condition enforcement for the RPM needed to solve the problem were developed.

In Chapter 4, the cavity-material perturbation method (CMPM) was expanded to waveguides filled with anisotropic material. We also propose an approach where a low order solution extracted from RPM was combined with CMPM, rendering a precise and low computational method if compared to the original CMPM.

In Chapter 5, two semi-analytical approaches based on the point matching method (PMM) for waveguides with arbitrary cross-sections and a double-layer anisotropic medium were studied. A mathematical formalism for source expansion in terms of cylindrical harmonics was described and applied for propagation scenarios in tunnels with realistic cross-sections.

As an extension for the PMM theory, we can list some research problems for the continuity of this work. The first is on further investigations on stable representation for fields in scenarios with extreme conductive conditions, where under- and over-flow issues in computing cylindrical functions are critical to an ordinary PMM. The second point suggested for study is related to the choice of points. For SPMM, a simple variation in point density for more critical regions

in the geometry can be tested. However, for IPMM, a study of non-uniform parameterization of the contour integrals can be explored for different regions of the contour. The third point is the use of Mathieu functions instead of cylindrical functions to expand the fields, in order to obtain a fast convergence for geometries that approximate an ellipse. The fourth point suggested to be explored involves the application of the PMM for modeling curved waveguides and tunnels, based on an initial formulation applied to the electromagnetic solution of toroidal guides. The direct application of this model is to the study of electromagnetic propagation along realistic tunnels with curvature along the longitudinal direction with non-circular cross-sections. In addition, the PMM methodology can also be extended to consider media with the presence of an absorbing boundary conditions such as a perfectly matched layer (PML).

6.1 Published Works

The author has contributed the following published works to the literature:

- J. R. Gonçalves, G. S. Rosa and F. L. Teixeira, "Perturbation Solution for Circular Waveguides Loaded with Eccentric Anisotropic Rods", *IEEE Microwave and Wireless Components Letters*, vol. 32, no. 8, pp. 935-938, Aug. 2022.

- J. R. Gonçalves, G. S. Rosa and F. L. Teixeira, "Perturbative Analysis of Anisotropic Coaxial Waveguides With Small Eccentricities via Conformal Transformation Optics", *IEEE Transactions on Microwave Theory and Techniques*, vol. 69, no. 9, pp. 3958-3966, Sep. 2021.

- J. R. Gonçalves, G. S. Rosa and F. L. Teixeira, "A Novel High-Order Perturbation Method for the Analysis of Eccentric Coaxial Waveguides Filled with Anisotropic Media", In *2021 SBMO/IEEE MTT-S International Microwave and Optoelectronics Conference* (IMOC), IEEE, pp. 1-5, 2021.

- J. R. Gonçalves, G. R. Rosa and F. L. Teixeira, "A Perturbation Method for the Analysis of Eccentric Coaxial Waveguides", In *2020 IEEE International Symposium on Antennas and Propagation and North American Radio Science Meeting*, APS-URSI, Montreal 2020, pp. 891-892.

– J. R. Gonçalves and G. R. Rosa, "A Novel Technique to the Computation of Cutoff Wavenumbers in Eccentric Coaxial Waveguides", In *URSI GASS 2020, Proceedings URSI GASS*, Rome 2020.

Bibliography

[1] W. C. Chew, M. S. Tong, and B. Hu, *Integral equation methods for electromagnetic and elastic waves*. New York, NY, USA: Morgan & Claypool, 2009.

[2] CST AG, CST Studio Suite 2019, Darmstadt, Germany, 2019.

[3] AC/DC Module User's Guide. COMSOL Multiphysics v. 5.4. COMSOL AB, Stockholm, Sweden. 2018.

[4] ANSYS HFSS 2019 R1, Canonsburg, PA, USA, 2019.

[5] J. A. Roumeliotis, A. B. M. S. Hossain, and J. G. Fikioris, "Cutoff wave numbers of eccentric circular and concentric circular-elliptic metallic wave guides," *Radio Sci.*, vol. 15, no. 05, pp. 923–937, Sep. 1980.

[6] A. D. Kotsis and J. A. Roumeliotis, "Cutoff wavenumbers of eccentric circular metallic waveguides," *IET Microw., Antennas Propag.*, vol. 8, no. 2, pp. 104–111, Jan. 2014.

[7] M. Gholizadeh, M. Baharian, and F. H. Kashani, "A simple analysis for obtaining cutoff wavenumbers of an eccentric circular metallic waveguide in bipolar coordinate system," *IEEE Trans. Microw. Theory Techn.*, vol. 67, no. 3, pp. 837–844, Mar. 2019.

[8] M. Gholizadeh and F. H. Kashani, "Analytical solution of higher order modes of a dielectric-lined eccentric coaxial cable," *Int. J. Microw. Wireless Technol.*, vol. 13, no. 3, pp. 1–8, Jul. 2020.

[9] H. Y. Yee and N. F. Audeh, "Cutoff frequencies of eccentric waveguides," *IEEE Trans. Microw. Theory Techn.*, vol. 14, no. 10, pp. 487–493, Oct. 1966.

[10] M. J. Beaubien and A. Wexler, "An accurate finite-difference method for higher order waveguide modes," *IEEE Trans. Microw. Theory Techn.*, vol. 16, no. 12, pp. 1007–1017, Dec. 1968.

[11] L. Tsang, J. A. Kong, and K.-H. Ding, *Scattering of electromagnetic waves: theories and applications*. John Wiley & Sons, 2004, vol. 27.

[12] S. Caorsi, M. Pastorino, and M. Raffetto, "Electromagnetic scattering by a multilayer elliptic cylinder under transverse-magnetic illumination: Series solution in terms of mathieu functions," *IEEE Transactions on Antennas and Propagation*, vol. 45, no. 6, pp. 926–935, Jun. 1997.

[13] W. C. Gibson, *The Method of Moments in Electromagnetics*. Boca Raton, FL, USA: Press,, 2015.

[14] A. Taflove and S. C. Hagness, *Computational Electrodynamics: The Finite-difference Time-domain Method by Allen Taflove and Susan C Hagness*. Artech House, 2005.

[15] C. W. Penney, R. J. Luebbers, and J. W. Schuster, "Scattering from coated targets using a frequency-dependent, surface impedance boundary condition in fdtd," *IEEE Transactions on Antennas and Propagation*, vol. 44, no. 4, pp. 434–443, Apr. 1996.

[16] D. B. Davidson, *Computational electromagnetics for RF and microwave engineering*. Cambridge University Press, 2010.

[17] H. Y. Yee and N. F. Audeh, "Uniform waveguides with arbitrary cross-section considered by the point-matching method," *IEEE Trans. Microw. Theory Techn.*, vol. 13, no. 6, pp. 847–851, Nov. 1965.

[18] R. H. T. Bates, "The theory of the point-matching method for perfectly conducting waveguides and transmission lines," *IEEE Transactions on Microwave Theory and Techniques*, vol. 17, no. 6, pp. 294–301, Jun. 1969.

[19] R. Lech, P. Kowalczyk, and A. Kusiek, "Scattering from a cylindrical object of arbitrary cross section with the use of field matching method," *IEEE Trans. Antennas Propag.*, vol. 64, no. 11, pp. 4883–4887, Nov. 2016.

[20] B. Aslanyürek and T. U. Gürbüz, "A continuity-based series solution for electromagnetic scattering by arbitrary shaped multilayer cylinders: Tm case," *IEEE Transactions on Antennas and Propagation*, vol. 65, no. 2, pp. 812–819, Feb. 2017.

[21] B. Aslanyürek, "Tm scattering by arbitrary-shaped multilayer cylinders having embedded inhomogeneities," *IEEE Antennas and Wireless Propagation Letters*, vol. 19, no. 4, pp. 576–580, Apr. 2020.

[22] M. Warecka, R. Lech, and P. Kowalczyk, "Propagation in the open cylindrical guide of arbitrary cross section with the use of field matching method," *IEEE Trans. Antennas Propag.*, vol. 66, no. 6, pp. 3237–3240, Jun. 2018.

[23] ——, "Scattering and propagation analysis for the multilayered structures based on field matching technique," in *2019 13th European Conference on Antennas and Propagation (EuCAP)*. IEEE, 2019, pp. 1–4.

[24] H. Kober, *Dictionary of conformal representations*. Vol. 2, New York, USA: Dover, 1957.

[25] R. Schinzinger and P. A. Laura, *Conformal Mapping: Methods and Applications*. Dover Publications, Inc., Mineola, New York., 2003.

[26] W. C. Chew, *Waves and fields in inhomogeneous media*. New York, NY, USA: John Wiley & Sons, 1995.

[27] G. S. Rosa, "Pseudo-analytical modeling for electromagnetic well-logging tools in complex geophysical formations," Ph.D. dissertation, Pontifical Catholic University of Rio de Janeiro, Rio de Janeiro, RJ, Brazil, 2017, DOI: 10.17771/PUCRio.acad.30559.

[28] R. F. Harrington, *Time-Harmonic Electromagnetic Fields*. New York, NY, USA: McGraw-Hill, Chapter 7, 1961.

[29] F. L. Teixeira and W. C. Chew, "Differential forms, metrics, and the reflectionless absorption of electromagnetic waves," *J. Electromagn. Waves Appl.*, vol. 13, no. 5, pp. 665–686, 1999.

[30] G. W. Milton, M. Briane, and J. R. Willis, "On cloaking for elasticity and physical equations with a transformation invariant form," *New Journal of Physics*, vol. 8, no. 10, p. 248, 2006.

[31] B. Donderici and F. L. Teixeira, "Metamaterial blueprints for reflectionless waveguide bends," *IEEE Microw. Wireless Compon. Lett.*, vol. 18, no. 4, pp. 233–235, Apr. 2008.

[32] L. Xu and H. Chen, "Conformal transformation optics," *Nature Photonics*, vol. 9, no. 1, pp. 15–23, Jan. 2015.

[33] G. S. Rosa, J. R. Bergmann, F. L. Teixeira, and M. S. Novo, "A perturbation-based method to model electromagnetic logging sensors in eccentric boreholes via conformal transformation optics," in *12th European Conference on Antennas and Propagation (EuCAP 2018)*, Apr. 2018, pp. 1–5.

[34] J. P. Turpin, A. T. Massoud, Z. H. Jiang, P. L. Werner, and D. H. Werner, "Conformal mappings to achieve simple material parameters for transformation optics devices," *Optics Express*, vol. 18, no. 1, pp. 244–252, Jan. 2010.

[35] C. Y. Tsao, D. N. Payne, and L. Li, "Modal propagation characteristics of radially stratified and d-shaped metallic optical fibers," *Applied optics*, vol. 28, no. 3, pp. 588–594, Feb. 1989.

[36] E. Butkov, *Mathematical Physics*, ser. Addison-Wesley world student series. Addison-Wesley, 1973.

[37] L. Lewin, D. Chang, and E. Kuester, *Electromagnetic waves and curved structures*. London, UK: Peter Peregrinus, 1977.

[38] G. S. Rosa, J. R. Bergmann, and F. L. Teixeira, "A perturbation method to model electromagnetic well-logging tools in curved boreholes," *IEEE Trans. Geosci. Remote Sens.*, vol. 56, no. 4, pp. 1979–1993, Apr. 2018.

[39] F. L. Teixeira, "Closed-form metamaterial blueprints for electromagnetic masking of arbitrarily shaped convex pec objects," *IEEE Antennas Wireless Propag. Lett.*, vol. 6, pp. 163–164, Feb. 2007.

[40] H. Yang and S. Lee, "A variational calculation of te and tm cutoff wavenumbers in circular eccentric guides by conformal mapping," *Microw. Opt. Technol. Lett.*, vol. 31, no. 5, pp. 381–384, Oct. 2001.

[41] S. B. Chakrabarty, S. B. Sharma, and B. N. Das, "Higher-order modes in circular eccentric waveguides," *Electromagnetics*, vol. 29, no. 5, pp. 377–383, Jun. 2009.

[42] B. N. Das and O. J. Vargheese, "Analysis of dominant and higher order modes for transmission lines using parallel cylinders," *IEEE Trans. Microw. Theory Techn.*, vol. 42, no. 4, pp. 681–683, Apr. 1994.

[43] J. Liu and L. Yuan, "Evanescent field characteristics of eccentric core optical fiber for distributed sensing," *J. Opt. Soc. Amer A.*, vol. 31, no. 3, pp. 475–479, Mar. 2014.

[44] K. Sainath and F. L. Teixeira, "Interface-flattening transform for em field modeling in tilted, cylindrically stratified geophysical media," *IEEE Antennas Wireless Propag. Lett.*, vol. 13, pp. 1808–1811, Dec. 2014.

[45] N. Schupfer, "Axisymmetric electromagnetic eigenmodes of plasma-filled toroidal resonators," *IEEE Trans. Plasma Sci.*, vol. 19, no. 5, pp. 906–911, Oct. 1991.

[46] C. A. Balanis, *Advanced engineering electromagnetics*. John Wiley & Sons, 2012.

[47] J. R. Gonçalves, G. S. Rosa, and F. L. Teixeira, "Perturbative analysis of anisotropic coaxial waveguides with small eccentricities via conformal transformation optics," *IEEE Trans. Microw. Theory Techn.*, vol. 69, no. 9, pp. 3958–3966, 2021.

[48] V. Rumsey, "Reaction concept in electromagnetic theory," *Physical Review*, vol. 94, no. 6, p. 1483, 1954.

[49] M. Gholizadeh and F. Hojjat Kashani, "A new analytical method for calculating the cutoff frequencies of an eccentrically dielectric-loaded circular waveguide," *IEEE Microw. Wireless Compon. Lett.*, vol. 30, no. 5, pp. 453–456, 2020.

[50] J. Kong, *Electromagnetic Wave Theory*. New York, NY, USA: Wiley, 1986.

[51] I. V. Lindell, A. H. Sihvola, S. Tretyakov, and A. J. Viitanen, *Electromagnetic Waves in Chiral and Bi-Isotropic Media*. London, England: Artech House, 1994.

[52] J. R. Gonçalves, G. S. Rosa, and F. L. Teixeira, "Perturbative analysis of anisotropic coaxial waveguides with small eccentricities via conformal transformation optics," *IEEE Trans. Microw. Theory Techn.*, 2021, accept (18-May-2021).

[53] G. N. Watson, *A treatise on the theory of Bessel functions*. Cambridge university press, 1995.

[54] W. Imbriale and R. Mittra, "The two-dimensional inverse scattering problem," *IEEE Trans. Antennas Propag.*, vol. 18, no. 5, pp. 633–642, Sep. 1970.

[55] R. Plonsey and R. E. Collin, *Electromagnetic fields*. New York: McGraw-Hill Book, 1961.

[56] D. M. Pozar, *Microwave Engineering*. Hoboken, NJ, USA: John Wiley & Sons, Inc., 3 ed., 2005.

[57] J. G. Van Bladel, *Electromagnetic fields*. IEEE Press Series on Electromagnetics Wave Theory, New York, NY, USA: IEEE Press, 2 ed., 2007, vol. 19.

[58] G. D. Kolezas, G. P. Zouros, and J. A. Roumeliotis, "Efficient and accurate calculation of the cutoff wavenumbers of coaxial elliptical-circular and circular-elliptical metallic waveguides," *IEEE Transactions on Microwave Theory and Techniques*, vol. 62, no. 10, pp. 2242–2250, 2014.

[59] D. G. Dudley, "Wireless propagation in circular tunnels," *IEEE Transactions on Antennas and Propagation*, vol. 53, no. 1, pp. 435–441, 2005.

[60] G. S. Rosa and J. R. Bergmann, "Electromagnetic propagation along lossy anisotropic and radially stratified cylindrical structures," in *2014 Loughborough Antennas and Propagation Conference (LAPC)*. IEEE, 2014, pp. 155–159.

[61] G. S. Rosa, "A robust method for solving the modal fields in radially-unbounded cylindrical waveguides with two layers under extreme conductive conditions," *IEEE Transactions on Antennas and Propagation*, 2022.

[62] A. Puzella and A. Palevsky, "Electromagnetic dispersion of a coaxial waveguide with an arbitrary radial dielectric profile," *IEEE transactions on electron devices*, vol. 35, no. 11, pp. 2048–2051, 1988.

[63] M. Abramowitz, "Abramowitz and stegun," *Applied Mathematics Series. National Bureau of Standards. New York, NY, USA: Dover*, 1968.

[64] R. E. Collin, *Field theory of guided waves*. John Wiley & Sons, 1990, vol. 5.

A
Second-Order Solution of the RMP

In order to determine the particular second-order solution using the ansatz of [27, 45], we can consider the set of equations based in operator L_m over $\rho^q B_p(\beta\rho)$ as follows

$$L_m\Big[\rho^q B_p(\beta\rho)\Big] = \left(p^2+q^2-m^2\right)\rho^{q-2}B_p(\beta\rho) + 2q\beta\rho^{q-1}B'_p(\beta\rho) \tag{A-1a}$$

$$= \Big[(p-q)^2-m^2\Big]\rho^{q-2}B_p(\beta\rho) + 2q\beta\rho^{q-1}B_{p-1}(\beta\rho) \tag{A-1b}$$

$$= \Big[(p+q)^2-m^2\Big]\rho^{q-2}B_p(\beta\rho) - 2q\beta\rho^{q-1}B_{p+1}(\beta\rho), \tag{A-1c}$$

where B_p is a linear combination of cylindrical functions with integer order p. First, we can rewrite equations (3-33a) as follows

$$L_n R_2^n = Z_3 - \left(Z_2^+ + Z_2^-\right) - Z_1 \tag{A-2}$$

where

$$Z_1 = 4\rho^2\beta^2 B_n(\beta\rho) + 2\rho^3\beta^3 B'_n(\beta\rho), \tag{A-3a}$$

$$Z_2^{\pm} = Z_2^+ + Z_2^- = 2\rho\beta^2 B^{1+}_{n+1}(\beta\rho) + 2\rho\beta^2 B^{1-}_{n-1}(\beta\rho), \tag{A-3b}$$

$$Z_3 = \alpha_2\alpha_0^2 k_{0,z}^2 B_n(\beta\rho). \tag{A-3c}$$

By using the combination of $p = n$, $q = 4$, $m = n$ in (Aa) we obtain

$$L_n\Big[\rho^4 B_n(\beta\rho)\Big] = 16\rho^2 B_n(\beta\rho) + 8\beta\rho^3 B'_n(\beta\rho)$$

$$L_n\left[\frac{\beta^2}{4}\rho^4 B_n(\beta\rho)\right] = Z_1, \tag{A-4}$$

and by using the combination of $p = n+2$, $q = 2$, $m = n$ in (Ab) we obtain

$$L_n\Big[\rho^2 B^{1+}_{n+2}(\beta\rho)\Big] = 4\beta\rho B^{1+}_{n+1}(\beta\rho)$$

$$L_n\left[\frac{\beta}{2}\rho^2 B^{1+}_{n+2}(\beta\rho)\right] = Z_2^+, \tag{A-5}$$

and by using the combination of $p = n - 2$, $q = 2$, $m = n$ in (Ac) we obtain

$$L_n\Big[\rho^2 B^{1-}_{n-2}(\beta\rho)\Big] = -4\beta\rho B^{1-}_{n-1}(\beta\rho)$$
$$L_n\left[-\frac{\beta}{2}\rho^2 B^{1-}_{n-2}(\beta\rho)\right] = Z_2^-, \tag{A-6}$$

and using combinations analogous we can obtain a equation for Z_3 expressed by

$$L_n\left[-\frac{\rho}{2\beta}B'_n(\beta\rho)\right] = B_n(\beta\rho)$$
$$L_n\left[-\alpha_2\alpha_0^2 k_{0,z}^2\frac{\rho}{2\beta}B'_n(\beta\rho)\right] = Z_3. \tag{A-7}$$

We can summarizing all Z's equations to obtain the solution of the term of R_2^n, given by

$$L_n R_2^n = L_n\left[-\alpha_2\alpha_0^2 k_{0,z}^2\frac{\rho}{2\beta}B'_n - \frac{\beta}{2}\rho^2 B^{1+}_{n+2} + \frac{\beta}{2}\rho^2 B^{1-}_{n-2} - \frac{\beta^2}{4}\rho^4 B_n\right]$$
$$R_2^n = -\alpha_2\alpha_0^2 k_{0,z}^2\frac{\rho}{2\beta}B'_n - \frac{\beta^2}{4}\rho^4 B_n + \frac{\beta}{2}\rho^2\left(B^{1-}_{n-2} - B^{1+}_{n+2}\right). \tag{A-8}$$

note that argument $(\beta\rho)$ of cylindrical functions has been omitted only by visual notation.

Similarly, we repeat this routine to find a solution of $R_2^{n\pm2}$, that is

$$L_{n\pm2}R_2^{n\pm2} = \pm L_{n\pm2}\left[\frac{\beta}{2}\rho^2 B_n^{1\pm}\right] \pm L_{n\pm2}\left[\frac{\beta}{2}\rho^3 B_{n\mp1}\right] \pm L_{n\pm2}\left[\frac{\beta^2}{8}\rho^4 B_{n\mp2}\right]$$
$$R_2^{n\pm2} = \pm\frac{\beta}{2}\rho^2 B_n^{1\pm} \pm \frac{\beta}{2}\rho^3 B_{n\mp1} \pm \frac{\beta^2}{8}\rho^4 B_{n\mp2}. \tag{A-9}$$

B
Solving the Integral of the CMPM

In what follows, $B_n(\beta\rho)$ denotes a linear combination of solutions for the Bessel differential equation of integer order n. After some simplifications on the Lommel integrals [63, p. 484], we obtained

$$\begin{aligned} I &= \int B_n(\beta\rho)^2\,\rho^3\,d\rho \\ &= \frac{\rho}{6\beta^3}\Big\{\beta\rho\Big[2n(n-1)+\beta^2\rho^2\Big]B_n(\beta\rho)^2 \\ &\qquad -2(n-1)\Big[2n(n+1)+\beta^2\rho^2\Big]B_n(\beta\rho)B_{n+1}(\beta\rho) \\ &\qquad\qquad +\beta\rho\Big[2(n^2-1)+\beta^2\rho^2\Big]B_{n+1}(\beta\rho)^2\Big\}. \end{aligned} \tag{B-1}$$

By defining $x=\beta\rho$ and omitting the the argument of the cylindrical functions, we can write

$$\begin{aligned} I = \frac{\rho^4}{6x^3}\Big\{&x\Big[2n(n-1)+x^2\Big]B_n^2 - 2(n-1)\Big[2n(n+1)+x^2\Big]B_nB_{n+1} \\ &+x\Big[2(n^2-1)+x^2\Big]B_{n+1}^2\Big\}. \end{aligned} \tag{B-2}$$

Alternatively, we can write

$$I = \frac{\rho^4}{6x^3}\Big\{aB_n^2+bB_nB_{n+1}+cB_{n+1}^2\Big\}. \tag{B-3}$$

The expression above can be further simplified on using the property [28, Appendix D]

$$B_{n+1} = -B_n' + \frac{n}{x}B_n, \tag{B-4}$$

that allows us to obtain

$$I = \frac{\rho^4}{6x^3}\Big\{aB_n^2+bB_n\left(-B_n'+\frac{n}{x}B_n\right)+c\left(-B_n'+\frac{n}{x}B_n\right)^2\Big\}. \tag{B-5}$$

From the boundary conditions associated to TM and TE fields, we should enforce $B_n=0$ and $B_n'=0$ at the PEC, respectively. As a consequence of the decoupling between TM and TE fields in a coaxial waveguide, we always have

$B_n B_n' = 0$ on the integration limits $\rho = \{r_0, r_1\}$. Then, (B-5) becomes

$$I = \frac{\rho^4}{6x^3}\left\{ \left(a + b\frac{n}{x} + c\frac{n^2}{x^2}\right) B_n^2 + cB_n'^2 \right\}. \tag{B-6}$$

In a simplifies form, the above can be written as

$$I = \frac{\rho^4}{6x^3}\left\{ d_{\mathrm{TM}} B_n^2 + d_{\mathrm{TE}} B_n'^2 \right\}, \tag{B-7}$$

where

$$d_{\mathrm{TM}} = \frac{1}{x}\Big[x^4 + x^2 n^2 - 2n^2(n-1)\Big], \tag{B-8a}$$

$$d_{\mathrm{TE}} = x^3 + 2(n^2 - 1)x. \tag{B-8b}$$

Recovering that $x = \beta\rho$ and $B_n(x)B_n'(x) = 0$ at the limits of the integration, (B-7) can be written as a contribution for TM and TE modes according to

$$I = \hat{I}_{\mathrm{TM}} + \hat{I}_{\mathrm{TE}}, \tag{B-9}$$

where

$$\hat{I}_{\mathrm{TM}} = \left[\frac{\rho^4}{6(\beta\rho)^3} d_{\mathrm{TM}} B_n(\beta\rho)^2\right]\Bigg|_{\rho=r_0}^{r_1}, \tag{B-10}$$

because $B_n(\beta\rho) = 0$ at $\rho = \{r_0, r_1\}$, and

$$\hat{I}_{\mathrm{TE}} = \left[\frac{\rho^4}{6(\beta\rho)^3} d_{\mathrm{TE}} B_n'(\beta\rho)^2\right]\Bigg|_{\rho=r_0}^{r_1}, \tag{B-11}$$

because $B_n'(\beta\rho) = 0$ at $\rho = \{r_0, r_1\}$.

C
Properties of Orthogonality Condition

This appendix is based on book [64, Ch. 5] and adapted for the waveguides studied in this thesis. Consider a cylindrical waveguide with perfectly conductive walls and filled with a uniaxially anisotropic material, illustrated in Fig. C.1. Also consider that G_{np} and $G_{n'p'}$ are scalar functions of the solutions for npth and $n'p'$th modes of E_z or H_z with their respective axial wavenumbers $k_{z,np}$ and $k_{z,n'p'}$. Multiplying the Helmholtz equation satisfied by G_{np} by $G_{n'p'}$, we have to

$$G_{n'p'}\nabla_s^2 G_{np} + \gamma\Big(k_s^2 - k_{z,np}^2\Big)G_{np}G_{n'p'} = 0, \tag{C-1}$$

where $\gamma = p_z/p_s$ with $p = \{\mu, \epsilon\}$ and $k_s^2 = \omega^2\mu_s\epsilon_s$. Similarly, multiplying and equation of $G_{n'p'}$ by G_{np}, we have

$$G_{np}\nabla_s^2 G_{n'p'} + \gamma\Big(k_s^2 - k_{z,n'p'}^2\Big)G_{n'p'}G_{np} = 0. \tag{C-2}$$

Subtracting the two previous equations and integrating the all area of the cross-section of the waveguide, we obtain

$$\gamma\Big(k_{z,n'p'}^2 - k_{z,np}^2\Big)\iint_S G_{np}G_{n'p'}\,dS = \iint_S \Big(G_{np}\nabla_s^2 G_{n'p'} - G_{n'p'}\nabla_s^2 G_{np}\Big)\,dS. \tag{C-3}$$

Analyzing the right side of the equality one, we can use the second identity of Green

$$\iint_S \Big(G_{np}\nabla_s^2 G_{n'p'} - G_{n'p'}\nabla_s^2 G_{np}\Big)\,dS = \oint_C \left(G_{np}\frac{\partial G_{n'p'}}{\partial\rho} - G_{n'p'}\frac{\partial G_{np}}{\partial\rho}\right)dl, \tag{C-4}$$

where C is the contour that denote the guide boundary. For TM modes we have that $E_{z,np}$ and $E_{z,n'p'}$ are zeros on the boundary and for TE modes $\partial H_{z,np}/\partial\rho$ and $\partial H_{z,n'p'}/\partial\rho$ are null on the boundary. So the boundary integral is disappeared and since $k_{z,np}^2 \neq k_{z,n'p'}^2$ we can reduce (C-3) to

$$\iint_S G_{np}G_{n'p'}\,dS = 0, \quad np \neq n'p'. \tag{C-5}$$

The above equation is equivalent to the equation used in the 3.5 section for hollow waveguides with perfectly conductive walls.

Futhermore, it is possible to establish a more general principle of orthogonality, which can be used for more complex waveguides. This more general property is obtained from the Lorentz principle of reciprocity. Consider two independent sets of fields $\mathbf{E}_1$, $\mathbf{H}_1$ and $\mathbf{E}_2$, $\mathbf{H}_2$ and satisfying Maxwell's

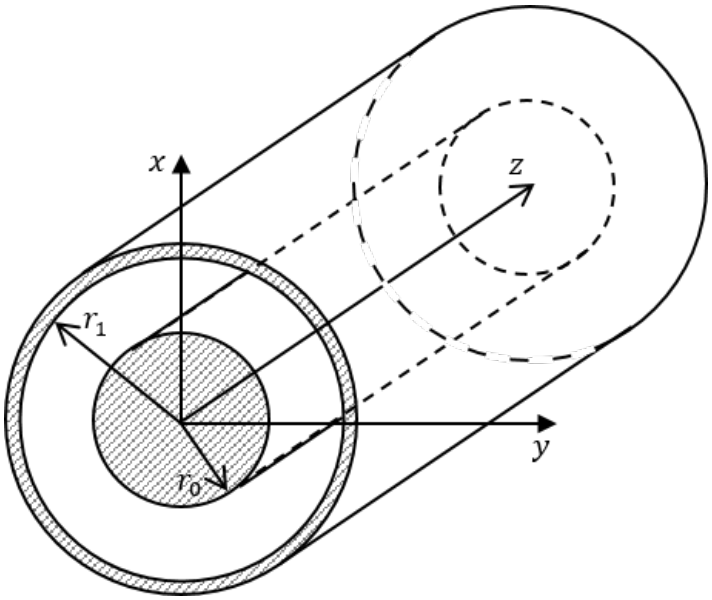

Figure C.1: Coaxial waveguide.

equations for a source-free medium, we can write

$$\boldsymbol{\nabla} \times \mathbf{E}_1 = i\omega\bar{\bar{\mu}} \cdot \mathbf{H}_1, \tag{C-6a}$$

$$\boldsymbol{\nabla} \times \mathbf{E}_2 = i\omega\bar{\bar{\mu}} \cdot \mathbf{H}_2, \tag{C-6b}$$

$$\boldsymbol{\nabla} \times \mathbf{H}_1 = -i\omega\bar{\bar{\epsilon}} \cdot \mathbf{E}_1, \tag{C-6c}$$

$$\boldsymbol{\nabla} \times \mathbf{H}_2 = -i\omega\bar{\bar{\epsilon}} \cdot \mathbf{E}_2, \tag{C-6d}$$

scalar multiplying (C-6a) by $\mathbf{H}_2$ and (C-6b) by $\mathbf{H}_1$, and then subtracting the two, we have

$$\mathbf{H}_2 \cdot \boldsymbol{\nabla} \times \mathbf{E}_1 - \mathbf{H}_1 \cdot \boldsymbol{\nabla} \times \mathbf{E}_2 = 0. \tag{C-7}$$

Repeating the same procedure for (C-6c) and (C-6d), but multiplying by $\mathbf{E}_2$ and $\mathbf{E}_1$, respectively , we have

$$\mathbf{E}_2 \cdot \boldsymbol{\nabla} \times \mathbf{H}_1 - \mathbf{E}_1 \cdot \boldsymbol{\nabla} \times \mathbf{H}_2 = 0. \tag{C-8}$$

By adding (C-7) and (C-8) we can find

$$\boldsymbol{\nabla} \cdot \Big(\mathbf{E}_1 \times \mathbf{H}_2 - \mathbf{E}_2 \times \mathbf{H}_1\Big) = 0, \tag{C-9}$$

since the identity

$$\boldsymbol{\nabla} \cdot (\mathbf{A} \times \mathbf{B}) = \mathbf{B} \cdot \boldsymbol{\nabla} \times \mathbf{A} - \mathbf{A} \cdot \boldsymbol{\nabla} \times \mathbf{B}, \tag{C-10}$$

is employed.

Since that the z dependency of $\mathbf{E}_1$, $\mathbf{H}_1$ is like $\exp(-ik_{1,z}z)$ and $\mathbf{E}_2$, $\mathbf{H}_2$

like $\exp(-ik_{2,z}z)$, in this case representing a field propagating in the direction $z < 0$, we can expand (C-9) to

$$\begin{aligned}\boldsymbol{\nabla}\cdot\Big(\mathbf{E}_1\times\mathbf{H}_2-\mathbf{E}_2\times\mathbf{H}_1\Big) &= \boldsymbol{\nabla}_s\cdot\Big(\mathbf{E}_1\times\mathbf{H}_2-\mathbf{E}_2\times\mathbf{H}_1\Big)\\ &\quad+\hat{z}\cdot\frac{\partial}{\partial z}\Big(\mathbf{E}_1\times\mathbf{H}_2-\mathbf{E}_2\times\mathbf{H}_1\Big)\\ &= \boldsymbol{\nabla}_s\cdot\Big(\mathbf{E}_1\times\mathbf{H}_2-\mathbf{E}_2\times\mathbf{H}_1\Big)\\ &\quad-i\Big(k_{1,z}+k_{2,z}\Big)\hat{z}\cdot\Big(\mathbf{E}_{1,s}\times\mathbf{H}_{2,s}-\mathbf{E}_{2,s}\times\mathbf{H}_{1,s}\Big),\end{aligned} \tag{C-11}$$

by rewriting (C-9) we have

$$\boldsymbol{\nabla}_s\cdot\Big(\mathbf{E}_1\times\mathbf{H}_2-\mathbf{E}_2\times\mathbf{H}_1\Big)=i\Big(k_{1,z}+k_{2,z}\Big)\hat{z}\cdot\Big(\mathbf{E}_{1,s}\times\mathbf{H}_{2,s}-\mathbf{E}_{2,s}\times\mathbf{H}_{1,s}\Big). \tag{C-12}$$

Integrating in all area (C-9) and using the divergence theorem in the two-dimensional form on the left side of equality, we obtain the following relation

$$\begin{aligned}&\oint_C\hat{z}\cdot\Big(\mathbf{E}_1\times\mathbf{H}_2-\mathbf{E}_2\times\mathbf{H}_1\Big)\,dl\\ &\qquad=i\Big(k_{1,z}+k_{2,z}\Big)\iint_S\Big(\mathbf{E}_{1,s}\times\mathbf{H}_{2,s}-\mathbf{E}_{2,s}\times\mathbf{H}_{1,s}\Big)\cdot\hat{z}\,dS,\end{aligned} \tag{C-13}$$

It is important to remember that as the guide walls are perfect electrical conductors we have $\hat{z}\times\mathbf{E}=0$, therefore $\hat{z}\cdot\mathbf{E}\times\mathbf{H}=\mathbf{H}\cdot(\hat{z}\times\mathbf{E})=0$, and then (C-13) reduces to

$$\Big(k_{1,z}+k_{2,z}\Big)\iint_S\Big(\mathbf{E}_{1,s}\times\mathbf{H}_{2,s}-\mathbf{E}_{2,s}\times\mathbf{H}_{1,s}\Big)\cdot\hat{z}\,dS=0. \tag{C-14}$$

It is appropriate to write the format of the transversal (to z) field functions, so that if we consider a cylindrical waveguide along z with circular cross-section Fig. C.1, we can write the following functions for the fields

$$\begin{aligned}\mathbf{E}_{1,s}(\rho,\phi,z)&=\mathbf{e}_{1,s}(\rho)\,e^{in\phi+ik_{1,z}z}\\ \mathbf{H}_{1,s}(\rho,\phi,z)&=\mathbf{h}_{1,s}(\rho)\,e^{in\phi+ik_{1,z}z}\end{aligned}\quad\text{and}\quad\begin{aligned}\mathbf{E}_{2,s}(\rho,\phi,z)&=\mathbf{e}_{2,s}(\rho)\,e^{-in\phi+ik_{2,z}z}\\ \mathbf{H}_{2,s}(\rho,\phi,z)&=\mathbf{h}_{2,s}(\rho)\,e^{-in\phi+ik_{2,z}z},\end{aligned} \tag{C-15}$$

where $\mathbf{e}$ and $\mathbf{h}$ are cylindrical vector functions transverse to z, so we have that the equation (C-14) can be summarized to

$$\Big(k_{1,z}+k_{2,z}\Big)\int_{r_0}^{r_1}\Big(\mathbf{e}_{1,s}\times\mathbf{h}_{2,s}-\mathbf{e}_{2,s}\times\mathbf{h}_{1,s}\Big)\cdot\hat{z}\,\rho\,d\rho=0. \tag{C-16}$$

However, we can also assume that the set of fields $\mathbf{E}_2$ and $\mathbf{H}_2$ is propagating in the opposite direction of z, thus, based on the symmetry with respect to z we can write

$$\begin{aligned}\mathbf{E}_{1,s}(\rho,\phi,z) &= \mathbf{e}_{1,s}(\rho)\, e^{in\phi+ik_{1,z}z} \\ \mathbf{H}_{1,s}(\rho,\phi,z) &= \mathbf{h}_{1,s}(\rho)\, e^{in\phi+ik_{1,z}z}\end{aligned} \quad \text{and} \quad \begin{aligned}\mathbf{E}_{2,s}(\rho,\phi,z) &= \mathbf{e}_{2,s}(\rho)\, e^{-in\phi-ik_{2,z}z} \\ \mathbf{H}_{2,s}(\rho,\phi,z) &= -\mathbf{h}_{2,s}(\rho)\, e^{-in\phi-ik_{2,z}z},\end{aligned} \tag{C-17}$$

substituting in the equation (C-14), we obtain

$$\Big(k_{1,z}-k_{2,z}\Big)\int_{r_0}^{r_1}\Big(\mathbf{e}_{1,s}\times\mathbf{h}_{2,s}+\mathbf{e}_{2,s}\times\mathbf{h}_{1,s}\Big)\cdot\hat{z}\,\rho\,d\rho=0. \tag{C-18}$$

Finally, by adding and subtracting (C-16) and (C-18) we can write the orthogonality relation between the fields of a waveguide, such as

$$\int_{r_0}^{r_1}\mathbf{e}_{2,s}\times\mathbf{h}_{1,s}\cdot\hat{z}\,\rho\,d\rho=0, \tag{C-19a}$$

$$\int_{r_0}^{r_1}\mathbf{e}_{1,s}\times\mathbf{h}_{2,s}\cdot\hat{z}\,\rho\,d\rho=0, \tag{C-19b}$$

the above equations are equivalent to the equations described in [64, Ch. 5].

C.1
Orthogonality Condition Using RPM Fields

The solution of the regular perturbation method requires an extra condition necessary to determine the unknown α_2. This condition is obtained using the orthogonality relation described in the previous section. However, we will use the zeroth- and second-order fields described by $\mathbf{E}_{0,s}$ and $\mathbf{H}_{2,s}$, respectively. The equation of (C-19) can be written

$$\begin{aligned}\int_0^{r_1}\mathbf{E}_{0,s}\times\mathbf{H}_{2,s}\cdot\hat{z}\rho d\rho &= \int_0^{r_1}\Big(E_{0,\rho}H_{2,\phi}-E_{0,\phi}H_{2,\rho}\Big)\rho d\rho \\ &= \int_0^{r_0}\Big[E_{0,\rho}(\beta_{\mathrm{I}}\rho)H_{2,\phi}(\beta_{\mathrm{I}}\rho)-E_{0,\phi}(\beta_{\mathrm{I}}\rho)H_{2,\rho}(\beta_{\mathrm{I}}\rho)\Big]\rho d\rho \\ &+\int_{r_0}^{r_1}\Big[E_{0,\rho}(\beta_{\mathrm{II}}\rho)H_{2,\phi}(\beta_{\mathrm{II}}\rho)-E_{0,\phi}(\beta_{\mathrm{II}}\rho)H_{2,\rho}(\beta_{\mathrm{II}}\rho)\Big]\rho d\rho,\end{aligned} \tag{C-20}$$

the equation above has the same boundaries as Fig. C.1, however the inner conductor is replaced by a dielectric. Thus, the problem is divided into two regions, where the region delimited by $0>\rho>r_0$ is denoted by index I and the region of $r_0>\rho>r_1$ is described by index II. The equation (C-20) can be

expanded to

$$A_{2,\mathrm{I}}^{e,n}Q_{\mathrm{I}}^{e,J}+A_{2,\mathrm{I}}^{h,n}Q_{\mathrm{I}}^{h,J}-\alpha_2\Big(Q_{\mathrm{I}}^{e,F}+Q_{\mathrm{I}}^{h,F}\Big)+\Big(Q_{\mathrm{I}}^{e,P}+Q_{\mathrm{I}}^{h,P}\Big) + A_{2,\mathrm{II}}^{e,n}Q_{\mathrm{II}}^{e,J}+B_{2,\mathrm{II}}^{e,n}Q_{\mathrm{II}}^{e,H}+A_{2,\mathrm{II}}^{h,n}Q_{\mathrm{II}}^{h,J}+B_{2,\mathrm{II}}^{h,n}Q_{\mathrm{II}}^{h,H} - \alpha_2\Big(Q_{\mathrm{II}}^{e,F}+Q_{\mathrm{II}}^{h,F}\Big)+\Big(Q_{\mathrm{II}}^{e,P}+Q_{\mathrm{II}}^{h,P}\Big)=0, \tag{C-21}$$

where for the region I we have

$$Q_{\mathrm{I}}^{e,J}=\frac{i\omega\epsilon_s\beta_{\mathrm{I}}^{e}}{k_\rho^2}\int_0^{r_0}E_{0,\rho}(\beta_{\mathrm{I}}\rho)J_n'(\beta_{\mathrm{I}}^{e}\rho)\rho d\rho-\frac{\omega\epsilon_s n}{k_\rho^2}\int_0^{r_0}E_{0,\phi}(\beta_{\mathrm{I}}\rho)J_n(\beta_{\mathrm{I}}^{e}\rho)d\rho, \tag{C-22a}$$

$$Q_{\mathrm{I}}^{h,J}=-\frac{k_z n}{k_\rho^2}\int_0^{r_0}E_{0,\rho}(\beta_{\mathrm{I}}\rho)J_n(\beta_{\mathrm{I}}^{h}\phi)d\rho-\frac{ik_z\beta_{\mathrm{I}}^{h}}{k_\rho^2}\int_0^{r_0}E_{0,\phi}(\beta_{\mathrm{I}}\rho)J_n'(\beta_{\mathrm{I}}^{h}\rho)\rho d\rho, \tag{C-22b}$$

$$Q_{\mathrm{I}}^{e,F}=\frac{i\omega\epsilon_s\beta_{\mathrm{I}}^{e}}{k_\rho^2}\int_0^{r_0}E_{0,\rho}(\beta_{\mathrm{I}}\rho)F'(\beta_{\mathrm{I}}^{e}\rho)\rho d\rho-\frac{\omega\epsilon_s n}{k_\rho^2}\int_0^{r_0}E_{0,\phi}(\beta_{\mathrm{I}}\rho)F(\beta_{\mathrm{I}}^{e}\rho)d\rho, \tag{C-22c}$$

$$Q_{\mathrm{I}}^{h,F}=-\frac{k_z n}{k_\rho^2}\int_0^{r_0}E_{0,\rho}(\beta_{\mathrm{I}}\rho)F(\beta_{\mathrm{I}}^{h}\phi)d\rho-\frac{ik_z\beta_{\mathrm{I}}^{h}}{k_\rho^2}\int_0^{r_0}E_{0,\phi}(\beta_{\mathrm{I}}\rho)F'(\beta_{\mathrm{I}}^{h}\rho)\rho d\rho, \tag{C-22d}$$

$$Q_{\mathrm{I}}^{e,P}=\frac{i\omega\epsilon_s\beta_{\mathrm{I}}^{e}}{k_\rho^2}\int_0^{r_0}E_{0,\rho}(\beta_{\mathrm{I}}\rho)P'(\beta_{\mathrm{I}}^{e}\rho)\rho d\rho-\frac{\omega\epsilon_s n}{k_\rho^2}\int_0^{r_0}E_{0,\phi}(\beta_{\mathrm{I}}\rho)P(\beta_{\mathrm{I}}^{e}\rho)d\rho, \tag{C-22e}$$

$$Q_{\mathrm{I}}^{h,P}=-\frac{k_z n}{k_\rho^2}\int_0^{r_0}E_{0,\rho}(\beta_{\mathrm{I}}\rho)F(\beta_{\mathrm{I}}^{h}\phi)d\rho-\frac{ik_z\beta_{\mathrm{I}}^{h}}{k_\rho^2}\int_0^{r_0}E_{0,\phi}(\beta_{\mathrm{I}}\rho)F'(\beta_{\mathrm{I}}^{h}\rho)\rho d\rho, \tag{C-22f}$$

and for region II we have

$$Q_{\mathrm{II}}^{e,J} = \frac{i\omega\epsilon_s\beta_{\mathrm{II}}^e}{k_\rho^2}\int_{r_0}^{r_1} E_{0,\rho}(\beta_{\mathrm{II}}\rho)J_n'(\beta_{\mathrm{II}}^e\rho)\rho d\rho - \frac{\omega\epsilon_s n}{k_\rho^2}\int_{r_0}^{r_1} E_{0,\phi}(\beta_{\mathrm{II}}\rho)J_n(\beta_{\mathrm{II}}^e\rho)d\rho, \tag{C-23a}$$

$$Q_{\mathrm{II}}^{e,H} = \frac{i\omega\epsilon_s\beta_{\mathrm{II}}^e}{k_\rho^2}\int_{r_0}^{r_1} E_{0,\rho}(\beta_{\mathrm{II}}\rho)H_n'(\beta_{\mathrm{II}}^e\rho)\rho d\rho - \frac{\omega\epsilon_s n}{k_\rho^2}\int_{r_0}^{r_1} E_{0,\phi}(\beta_{\mathrm{II}}\rho)H_n(\beta_{\mathrm{II}}^e\rho)d\rho, \tag{C-23b}$$

$$Q_{\mathrm{II}}^{h,J} = -\frac{k_z n}{k_\rho^2}\int_{r_0}^{r_1} E_{0,\rho}(\beta_{\mathrm{II}}\rho)J_n(\beta_{\mathrm{II}}^h\phi)d\rho - \frac{ik_z\beta_{\mathrm{II}}^h}{k_\rho^2}\int_{r_0}^{r_1} E_{0,\phi}(\beta_{\mathrm{II}}\rho)J_n'(\beta_{\mathrm{II}}^h\rho)\rho d\rho, \tag{C-23c}$$

$$Q_{\mathrm{II}}^{h,H} = -\frac{k_z n}{k_\rho^2}\int_{r_0}^{r_1} E_{0,\rho}(\beta_{\mathrm{II}}\rho)H_n(\beta_{\mathrm{II}}^h\phi)d\rho - \frac{ik_z\beta_{\mathrm{II}}^h}{k_\rho^2}\int_{r_0}^{r_1} E_{0,\phi}(\beta_{\mathrm{II}}\rho)H_n'(\beta_{\mathrm{II}}^h\rho)\rho d\rho, \tag{C-23d}$$

$$Q_{\mathrm{II}}^{e,F} = \frac{i\omega\epsilon_s\beta_{\mathrm{II}}^e}{k_\rho^2}\int_{r_0}^{r_1} E_{0,\rho}(\beta_{\mathrm{II}}\rho)F'(\beta_{\mathrm{II}}^e\rho)\rho d\rho - \frac{\omega\epsilon_s n}{k_\rho^2}\int_{r_0}^{r_1} E_{0,\phi}(\beta_{\mathrm{II}}\rho)F(\beta_{\mathrm{II}}^e\rho)d\rho, \tag{C-23e}$$

$$Q_{\mathrm{II}}^{h,F} = -\frac{k_z n}{k_\rho^2}\int_{r_0}^{r_1} E_{0,\rho}(\beta_{\mathrm{II}}\rho)F(\beta_{\mathrm{II}}^h\phi)d\rho - \frac{ik_z\beta_{\mathrm{II}}^h}{k_\rho^2}\int_{r_0}^{r_1} E_{0,\phi}(\beta_{\mathrm{II}}\rho)F'(\beta_{\mathrm{II}}^h\rho)\rho d\rho, \tag{C-23f}$$

$$Q_{\mathrm{II}}^{e,P} = \frac{i\omega\epsilon_s\beta_{\mathrm{II}}^e}{k_\rho^2}\int_{r_0}^{r_1} E_{0,\rho}(\beta_{\mathrm{II}}\rho)P'(\beta_{\mathrm{II}}^e\rho)\rho d\rho - \frac{\omega\epsilon_s n}{k_\rho^2}\int_{r_0}^{r_1} E_{0,\phi}(\beta_{\mathrm{II}}\rho)P(\beta_{\mathrm{II}}^e\rho)d\rho, \tag{C-23g}$$

$$Q_{\mathrm{II}}^{h,P} = -\frac{k_z n}{k_\rho^2}\int_{r_0}^{r_1} E_{0,\rho}(\beta_{\mathrm{II}}\rho)F(\beta_{\mathrm{II}}^h\phi)d\rho - \frac{ik_z\beta_{\mathrm{II}}^h}{k_\rho^2}\int_{r_0}^{r_1} E_{0,\phi}(\beta_{\mathrm{II}}\rho)F'(\beta_{\mathrm{II}}^h\rho)\rho d\rho. \tag{C-23h}$$